RWTH AACHEN UNIVERSITY

MASTER THESIS

Spectral Flow and Fractional Charge Pumping in Topological Insulators

Author:
Felix BOSCHKE

Supervisors:
Prof. Dr. Fabian HASSLER
Prof. Dr. Markus MÜLLER

A thesis submitted in fulfillment of the requirements for the degree of Master of Science

in the

Hassler Group
Institute for Quantum Information

April 23, 2026

Declaration of Authorship

I, Felix BOSCHKE, declare that this thesis, "Spectral Flow and Fractional Charge Pumping in Topological Insulators", is my original work. Generative AI (Gemini, Google) was used exclusively to optimize sentence structure and enhance the clarity. No scientific content, data, or interpretations were produced or modified by the AI model.

RWTH AACHEN UNIVERSITY

Abstract

Faculty of Mathematics and Natural Sciences
Institute for Quantum Information

Master of Science

Spectral Flow and Fractional Charge Pumping in Topological Insulators

by Felix BOSCHKE

This thesis investigates the surface states of a spherical three-dimensional topological insulator (3D TI) containing a central magnetic monopole with a Dirac string. A magnetic monopole with an integer number of flux quanta in a 3D TI binds half-integer electric charge, which is known as the Witten effect. However, we analyze the effect of an unquantized magnetic flux which necessitates an additional boundary condition within a critical angular momentum subspace. To resolve this, we apply a momentum-squared regularization in a local flat-space limit that requires states to vanish at the string, uniquely fixing the boundary condition. This allows us to analytically determine the spectral flow of the system and it is shown how topological zero modes continuously form. Because zero modes carry half an elementary charge, the charge has to fractionalize during the formation of a zero mode. Thus, we further model the system as an adiabatic quantum pump to calculate the associated charge transport between the surface and monopole. By deriving states in the TI bulk, which are bound to the Dirac string, we demonstrate that during the formation of a zero mode half an electric charge is pumped between the surface and the monopole by the Dirac string, in accordance with the Witten effect.

Contents

List of Figures

To my friends

Chapter 1

Introduction and chapter overview

This thesis investigates topological insulators (TIs) which are a unique class of materials first identified two decades ago [1, 2]. They behave as a standard band insulator characterized by a finite energy gap in its bulk electronic spectrum. However, in contrast to ordinary insulators, this gapped bulk is accompanied by gapless conducting states confined strictly to the material's physical boundaries, which are symmetry protected. Consequently, TIs have garnered attention as promising materials for advancing a broad range of technologies such as spintronics and quantum computation [3].

Specifically, this thesis mainly treats the Bernevig-Hughes-Zhang model (BHZ) for three-dimensional topological insulators (3D TIs) [1]. The surface states in the BHZ-model are described by a massless two-dimensional Dirac Hamiltonian and are influenced by the underlying geometry of the surface. While the Dirac equation originally emerged in particle physics to describe fundamental fermions [4], its realization here bridges the gap between high-energy physics and condensed matter making 3D TIs an ideal testing ground for exploring Dirac fermions in solid-state systems.

This thesis examines the behavior of the surface states on a spherical geometry, the Dirac sphere, with a magnetic monopole at the center [5]. To describe the magnetic flux through this closed surface, we introduce a vector potential that contains a singularity known as a Dirac string. Standard frameworks usually impose a quantization condition on the flux to ensure the string does not affect charged particles [6]. By relaxing this condition, the Dirac string becomes a physical object with a continuously variable flux. This allows us to study the spectral flow which describes the continuous evolution of the surface states and their spectrum as the magnetic flux changes.

While the Dirac sphere with a non-quantized monopole has been explored numerically in Ref. [5], this thesis provides a rigorous analytical treatment of the system. The most significant result of this configuration is the manifestation of fermionic zero energy modes whose number is dictated by the integer part of the flux [5]. An occupied zero mode in a Dirac Hamiltonian carries exactly half an elementary electronic charge. Under spectral flow, increasing the flux by one quantum forms an occupied zero mode. If the state is occupied in the beginning of the process, where it has non-zero energy, it carries an electronic charge but it ends up at zero energy where it carries only half an electric charge. The remaining half-charge cannot vanish and must relocate. This fractional charge is suggested to bind directly to the magnetic monopole at integer flux quanta, a phenomenon known as the Witten effect [7, 8].

A primary goal of this work is to gain analytical access to the mechanism that transports this fractional charge from the surface to the monopole. We present a method to solve the spectral flow of the Dirac sphere's surface states analytically using a regularization for the singular Dirac string. We demonstrate how wavefunctions in a critical subspace localize at the string. Subsequently, taking the bulk into account an effective model for the fractional charge transport is developed.

To systematically develop this analytical description, the thesis is structured as follows.

In Ch. 2, we lay out the theoretical framework necessary to understand 3D TIs and their surface states. We introduce core topological concepts such as the Berry phase, Chern number and the Jackiw-Rebbi model to derive the surface Hamiltonian and understand topological phases. Furthermore, we provide a comprehensive overview of the influence of magnetic fields in quantum mechanics. This includes detailed discussions of the Aharonov-Bohm effect in the context of Berry phases and the notion of spectral flow, building the physical intuition required for the gauge fields addressed in this work.

Chapter 3 isolates the mathematical challenge of non-quantized magnetic flux in the monopole-string configuration by neglecting the spatial curvature of the Dirac sphere. As a local flat-space limit of the North Pole of the Dirac sphere, we investigate a planar two-dimensional Dirac disc pierced by a singular Aharonov-Bohm flux at the origin. A central ambiguity arises in a specific angular momentum subspace, where two mathematically valid solutions exist, necessitating an additional boundary condition at the origin to uniquely determine the physical states. To resolve this, we establish a rigorous regularization method guided by numerical simulations. These simulations employ a Wilson term to eliminate fermion doublers. By retaining this term in the continuum limit, we introduce the required physical regularization, analogous to the approach developed in Ref. [9].

In Ch. 4, we extend this regularization scheme to the globally curved space of the Dirac sphere, representing the full 3D TI surface enclosing the magnetic monopole and Dirac string. Under the assumption that the regularization length scale is small enough so that local curvature can be neglected, we can directly apply the regularization used for the flat Dirac disc limit to the Dirac sphere. This allows us to analytically solve the Dirac equation in the presence of a continuous magnetic flux, granting us analytical access to the surface states and their spectrum which are then analyzed.

In Ch. 5, we develop a theoretical framework for charge fractionalization by explicitly incorporating the 3D bulk of the topological insulator. While a purely two-dimensional surface model describes the formation of a zero-mode, it fundamentally lacks a direct mechanism for charge transport into the sphere's interior. Guided by numerical results [5, 10], we model this transport as occurring along the Dirac string. Specifically, we treat the system as a quantum pump where the spherical surface and an additional inner spherical surface surrounding the magnetic monopole act as two separate

leads. These leads are connected by the Dirac string which enables the exchange of charge. This construction allows us to employ Brouwer's framework for adiabatic charge transport, providing a rigorous method to calculate the charge transferred during the continuous increase of magnetic flux by one flux quantum.

Chapter 2

Foundational concepts

In this chapter we turn to the requisite theoretical framework, to study the surface states of TIs and their spectral flow under the variation of a magnetic field in particular.

The following sections introduce the core concepts needed in the course of this thesis, drawing primarily from [5, 6, 11, 12]. While we refer the reader to these works for a comprehensive treatment of the subjects, the overview in this chapter provides all derivations and concepts to the extent necessary for the scope of this thesis.

2.1 Geometry and the Berry phase

In this section, we establish the mathematical foundations required to understand topological phases, starting from the geometric properties of wavefunctions, the Berry phase.

The goal is to understand how a system that depends on a set of external parameters evolves under changing these parameters. Thus, we analyze the adiabatic evolution of a quantum state using the time-dependent Schrödinger equation

$$i\hbar\frac{\partial}{\partial t}\left|\psi(t)\right\rangle = H(\boldsymbol{R}(t))\left|\psi(t)\right\rangle \tag{2.1}$$

Here, the Hamiltonian $H(\boldsymbol{R})$ depends on a set of time-dependent parameters $\boldsymbol{R}(t) = (R_1(t), R_2(t), \dots)$, that vary slowly along a path $\mathcal{C}$ in parameter space.

We introduce the instantaneous groundstate $|n(\boldsymbol{R})\rangle$ which satisfies the time-independent equation at any fixed configuration of parameters

$$H(\boldsymbol{R})\left|n(\boldsymbol{R})\right\rangle = E_n(\boldsymbol{R})\left|n(\boldsymbol{R})\right\rangle. \tag{2.2}$$

We can assume the system remains in the non-degenerate groundstate as long as the parameters are varied slowly compared to the energy gap Δ to the next excited eigenstate. This is described by

$$\hbar\frac{dR_i}{dt} \ll \Delta. \tag{2.3}$$

Therefore, we propose an ansatz for the time-evolved state $|\psi(t)\rangle$

$$|\psi(t)\rangle = \exp\left(-\frac{i}{\hbar}\int_0^t E_n[\boldsymbol{R}(t')]dt'\right) e^{i\gamma_n(t)} \, |n[\boldsymbol{R}(t)]\rangle \,, \tag{2.4}$$

that includes both a dynamical phase, depending on the energy E_n, and the geometric phase $\gamma_n(t)$. This ansatz governs the adiabatic evolution only in zeroth order, neglects terms of order $\frac{dR_i}{dt}$ or higher and assumes no mixing with higher excited states.

Substituting the adiabtic ansatz into the time-dependent Schrödinger equation and projecting onto $\langle n(\boldsymbol{R}(t))|$, the energy terms cancel, leaving an equation for the geometric phase evolution

$$\frac{d\gamma_n}{dt} = i \langle n(\boldsymbol{R})| \frac{d}{dt} |n(\boldsymbol{R})\rangle = i \langle n(\boldsymbol{R})| \nabla_{\boldsymbol{R}} |n(\boldsymbol{R})\rangle \cdot \frac{d\boldsymbol{R}}{dt}. \tag{2.5}$$

Integrating this expression over time, where $\boldsymbol{R}(t)$ traces a closed loop $\mathcal{C}$ in parameter space, yields the Berry phase

$$\gamma_n = \oint_{\mathcal{C}} i \langle n(\boldsymbol{R})| \nabla_{\boldsymbol{R}} |n(\boldsymbol{R})\rangle \cdot d\boldsymbol{R} = \oint_{\mathcal{C}} \boldsymbol{\mathcal{A}}_n(\boldsymbol{R}) \cdot d\boldsymbol{R}. \tag{2.6}$$

Here, the Berry connection

$$\boldsymbol{\mathcal{A}}_n(\boldsymbol{R}) = i \langle n(\boldsymbol{R})| \nabla_{\boldsymbol{R}} |n(\boldsymbol{R})\rangle \tag{2.7}$$

is identified.

While global phases do not matter for quantum states, relative phases are measurable in interference experiments. Therefore, the Berry phase has physical consequences which manifests in $\boldsymbol{\mathcal{A}}_n$ being gauge-dependent, but the Berry phase over a closed loop being gauge invariant modulo 2π. For two- and three-dimensional parameter spaces this can be expressed via the gauge-invariant Berry curvature $\boldsymbol{\Omega}_n(\boldsymbol{R})$ using Stokes' theorem

$$\boldsymbol{\Omega}_n(\boldsymbol{R}) = \nabla_{\boldsymbol{R}} \times \boldsymbol{\mathcal{A}}_n(\boldsymbol{R}). \tag{2.8}$$

Note that in two-dimensions the Berry curvature only consists of the z-component.

In the specific context of crystalline solids, the relevant parameter space is the Brillouin zone (BZ), and the parameter vector $\boldsymbol{R}$ corresponds to the crystal momentum $\boldsymbol{k}$. However, all possible other parameters are possible, i.e. magnetic and electric fields or potential energy parameters.

2.2 Topological insulators and surface states

With the mathematical framework for parameter dependent Hamiltonians at hand, we can proceed with two- and three-dimensional topological insulator models. We start by introducing the two-dimensional Chern insulator, a simple system which contains all the distinct features of a topological insulator.

After this we extend the model to three dimensions.

The simplest realization of a system which supports topological phases, is the Chern insulator which is a lattice model characterized by two internal degrees of freedom per unit cell.

To study two-band models in general, we use the reciprocal space description. By factoring the wavefunction into spatial and internal components, we obtain

$$|\psi_{\boldsymbol{k}}\rangle = \frac{1}{\sqrt{N}} \sum_m e^{i\boldsymbol{k}\cdot\boldsymbol{R}_m} |m\rangle \otimes |\alpha\rangle \equiv |\boldsymbol{k}\rangle \otimes |\alpha\rangle, \tag{2.9}$$

where $\boldsymbol{R}_m$ denotes the lattice vectors over N unit cells, and $|\alpha\rangle$ represents the internal two-level state. According to Bloch's theorem, this translationally invariant basis block-diagonalizes the full Hamiltonian into momentum-dependent 2×2 Hermitian matrices $h_{\boldsymbol{k}} \equiv \langle \boldsymbol{k}|H|\boldsymbol{k}\rangle$. Here H is the real-space lattice Hamiltonian.

Any such Bloch Hamiltonian of a two-band model can be parametrized by

$$h(\boldsymbol{k}) = \boldsymbol{d}(\boldsymbol{k}) \cdot \boldsymbol{\tau} + \varepsilon(\boldsymbol{k}) I. \tag{2.10}$$

Here, $\boldsymbol{\tau} = (\tau_x, \tau_y, \tau_z)^T$ is the vector of the Pauli matrices , describing an orbital degree of freedom, and the vector $\varepsilon(\boldsymbol{k})$ and $\boldsymbol{d}(\boldsymbol{k})$ contain information about the hopping and on-site terms. We set $\varepsilon(\boldsymbol{k}) = 0$ in the remainder of this chapter. Moreover, $\boldsymbol{k}$ is the crystal momentum in the first Brillouin zone.

For the Chern insulator, the components of $\boldsymbol{d}(\boldsymbol{k})$ are

$$d_x = A \sin(k_x), \tag{2.11a}$$

$$d_y = A \sin(k_y), \tag{2.11b}$$

$$d_z = M + B[\cos(k_x) + \cos(k_y) - 2], \tag{2.11c}$$

with the parameter $M \in \mathbb{R}$ and $k_i \in (-\pi, \pi]$ the dimensionless crystal momenta in the first Brillouin zone, using the lattice spacing $a = 1$. We use a unit system so that the parameters are dimensionless and to simplify matters we also set $B = 1$ here.

The two-band spectrum of the Chern insulator is obtained as

$$E_\pm(\boldsymbol{k}) = \pm|\boldsymbol{d}(\boldsymbol{k})| = \pm\sqrt{A^2\left[\sin^2(k_x) + \sin^2(k_y)\right] + \left[M + \cos(k_x) + \cos(k_y) - 2\right]^2}. \tag{2.12}$$

Notice, that the first equality holds for arbitrary choices $\boldsymbol{d}(\boldsymbol{k})$.

The critical points of the spectrum, where the gap closes and thus describes a conductor, correspond to the $k_x = k_y = 0$ for $M = 0$, the two points $k_x = 0, k_y = \pi$ and $k_x = \pi, k_y = 0$ for $M = 2$ and the equivalent points $k_x = k_y = \pi$ for $M = 4$. For all other values of M the spectrum is gapped and thus describes an insulator. Therefore, the parameter M can only be deformed in intervals between the aforementioned values without closing the gap and determines the topological phase for this model.

As we have a two-dimensional parameter space $\boldsymbol{k} \in BZ$ we can determine the Berry curvature from (2.8) using the groundstate of (2.10) which then

yields

$$\Omega_z(\boldsymbol{k}) = \frac{1}{2}\hat{\boldsymbol{d}} \cdot \left(\frac{\partial \hat{\boldsymbol{d}}}{\partial k_x} \times \frac{\partial \hat{\boldsymbol{d}}}{\partial k_y} \right), \tag{2.13}$$

with the unit vector $\hat{\boldsymbol{d}} = \boldsymbol{d}/|\boldsymbol{d}|$ [13]. Using this to calculate the Berry phase for a closed loop around the first Brillouin zone's edge, denoted by ∂BZ, gives us

$$\mathrm{C}^{(1)} \equiv \frac{\gamma}{2\pi} = \frac{1}{2\pi} \oint_{\partial BZ} \boldsymbol{\mathcal{A}}(\boldsymbol{R}) \cdot d\boldsymbol{R} = \frac{1}{4\pi} \int_{BZ} d^2\boldsymbol{k}\, \hat{\boldsymbol{d}} \cdot \left(\frac{\partial \hat{\boldsymbol{d}}}{\partial k_x} \times \frac{\partial \hat{\boldsymbol{d}}}{\partial k_y} \right) \tag{2.14}$$

defining the Chern number $\mathrm{C}^{(1)}$. Varying the crystal momentum $\boldsymbol{k}$ through the entire Brillouin zone, the vector $\hat{\boldsymbol{d}}(\boldsymbol{k})$ traces out a surface. The Chern number counts how many times this surface contains the origin. Note that it only makes sense to calculate the Chern number for a gapped system, so at values $M \neq 0, 2, 4$, because this assumption is made in the derivation of the Berry phase the Chern number is defined with.

Performing the integral for the Chern number results in

$$\mathrm{C}^{(1)} = \begin{cases} 1, & 2 < M < 4 \\ -1, & 0 < M < 2 \\ 0, & \text{otherwise} \end{cases}. \tag{2.15}$$

Consequently, the Chern number is quantized to integer values. It informs in which topological phase the system is and changes at the values $M = 0, 2, 4$, where the spectrum is gapless and undergoes a non-trivial transition.

If the system has zero Chern number it is in the topologically trivial phase. The Berry connection has no singular points which would give rise to a non-zero Chern number in the integral (2.14). Similarly, a zero Chern number means that the surface traced out by the vector $\hat{\boldsymbol{d}}(\boldsymbol{k})$ does not contain the origin as $\boldsymbol{k}$ is varied through the first Brillouin zone.

In the parameter regimes $M > 4$ or $M < 0$ we can adiabatically deform the system to $M \to \pm\infty$ respectively which is a simple decoupled two-level system, hence we call this the trivial phase. However, for non-zero Chern numbers this is not the case. We cannot adiabatically deform the Hamiltonian to $M \to \pm\infty$ without going through $M = 0, 2$ or 4, so without closing the gap. Therefore, these regimes are in the topoligical phase.

Now that we have understood how the different topological phases appear for the example of the Chern insulator we we want to derive how edge states emerge. We consider a Chern insulator with a spatially varying parameter $M = M(x)$ such that the spectrum is ungapped at some point in space.

For this we use an arbitrary profile $M(x)$ which fulfills $M(x \to \infty) = M_R < 0$, $M(x \to -\infty) = M_L \in (0, 2)$ and $M(0) = 0$. Thus, for $x = 0$ the gap closes at $\boldsymbol{k} = 0$. This means we have a system with an infinite edge in the y-direction at $x = 0$. Therefore, the system is translationally invariant

along y so that k_y remains a good quantum number. Moreover, we expand the Hamiltonian around $\boldsymbol{k} = 0$, where the gap closes for $M(0) = 0$ which yields

$$H_0 = M(x)\tau_z - iA\tau_x\partial_x, \tag{2.16}$$

leaving out the term Ak_y.

The edge Hamiltonian has a zero energy eigenstate

$$H_0\psi_0(x) = 0, \tag{2.17}$$

which is found to be

$$\psi_0(x) = Ne^{\int_0^x M(x')/Adx'} \begin{pmatrix} 1 \\ -i \end{pmatrix} \tag{2.18}$$

with some normalization constant N. This is known as the Jackiw-Rebbi model [14]. The state decays exponentially into both regions $x < 0$ and $x > 0$. It is maximally localized at $x = 0$ making it exponentially confined to the edge. Note, that this state does not depend on the exact profile $M(x)$ but only on the fact that it transitions from a topological to a trivial phase at some point in space.

The full Hamiltonian at the edge reads $H_0 + Ak_y\tau_y$. If we project this Hamiltonian into the edge state subspace we get the effective Hamiltonian

$$H_{\text{edge}} = \int_{-\infty}^{\infty} dx\psi_0(x)^\dagger \left(H_0 + A\tau_y k_y\right)\psi_0(x) = -Ak_y, \tag{2.19}$$

which describes the edge modes of the system. The spectrum is given by $E_{\text{edge}} = -Ak_y$ for $k_y \ll 1$. For large k_y the edge state spectrum merges with the bulk spectrum again. This means that the edge states provide gapless modes for the otherwise insulating gapped bulk spectrum making the Chern insulator only conducting at the edge. Moreover, the edge state is chiral as it only moves in one direction along the boundary.

Lastly, we can extend the occurrence of edge states to the low-energy continuum model of the Chern insulator. This is achieved by expanding $\boldsymbol{d}(\boldsymbol{k})$ around $\boldsymbol{k} = 0$ which yields

$$d_x = Ak_x, \tag{2.20a}$$

$$d_y = Ak_y, \tag{2.20b}$$

$$d_z = M + B\left[k_x^2 + k_y^2\right], \tag{2.20c}$$

where we flip the sign of B for convenience. Consequently, reciprocal space is now $\boldsymbol{k} \in \mathbb{R}^2$. The resulting Hamiltonian corresponds to a massive continuum Dirac Hamiltonian in two dimensions with an additional quadratic term, namely

$$h_c(\boldsymbol{k}) = A\boldsymbol{\tau}\cdot\boldsymbol{k} + \left(M + B\boldsymbol{k}^2\right)\tau_z. \tag{2.21}$$

For this Hamiltonian we can proceed in the exact same fashion as for the

lattice version and find the zero-energy edge states using a mass profile $M(x)$ that changes sign at $x = 0$ from $M > 0$ for $x < 0$ to $M < 0$ for $x > 0$. This gives rise to the edge model $H_{\text{edge}} = -Ak_y$. Note, that we also ignore terms k_i^2 for this derivation, similar to the lattice model which can also be described setting $B = 0$.

Additionally, we can also calculate the Chern number via equation (2.14) which holds for arbitrary $\boldsymbol{d}$. If we consider a simplified model with $B = 0$ we get

$$\mathrm{C}^{(1)} = -\frac{1}{2}\,\mathrm{sgn}(M). \tag{2.22}$$

Although the original model has a non-zero quadratic term, the essential change of the Chern number is contained in the linear model as well [5].

The Chern number itself is not quantized because we are considering a continuum model for which the reciprocal space $\mathbb{R}^2$ is not compact as for the case of the Brillouin zone, but there is still an edge state if M changes sign because $|\Delta \mathrm{C}^{(1)}| = 1$ remains an integer. The change of the Chern number is important because it governs the number of edge states between two regimes. Instead of having multiple regimes for the Chern number as in the lattice model (2.15) we only have two phases governed by the sign of M.

Therefore, the low-energy continuum model suffices to capture the appearance of surface states we are interested in. This is the reason why we use continuum models in the following, while keeping in mind that they emerge from the low-energy continuum limit of a lattice description.

2.3 3D Bernevig-Hughes-Zhang model

We introduce the three-dimensional Bernevig-Hughes-Zhang (BHZ) model described by the low-energy continuum Hamiltonian

$$H_{\text{BHZ}} = \left(M + B\boldsymbol{k}^2\right)\tau_z + A\boldsymbol{k}\cdot\boldsymbol{\sigma}\tau_x \tag{2.23}$$

with $\boldsymbol{k} \in \mathbb{R}^3$. Here $\boldsymbol{\tau}$ is the orbital degree of freedom and $\boldsymbol{\sigma}$ is the spin degree of freedom, whereas both are vectors of the Pauli matrices. To simplify the notation we omit the tensor product symbol and write $\sigma_i\tau_j$ instead of $\sigma_i \otimes \tau_j$.

Rather than calculating the Chern number, we try to find the zero-energy surface states of this model for a varying mass profile. This means we have a model which undergoes a transition between a trivial and topological phase, similar to the Chern insulator, but now in three dimensions. Instead of edge states, we have surface states because of the additional dimension.

We define a single two-dimensional surface with surface normal vector $\hat{\boldsymbol{n}}$. Similar to the calculation of the edge states in the continuum model of the Chern insulator (2.20), we set $B = 0$ because the linear term suffices to capture the essential physics [5].

For an arbitrary vector $\boldsymbol{x}$ we define the quantities $x_n = \hat{\boldsymbol{n}}\cdot\boldsymbol{x}$ and $x_{\parallel} = \boldsymbol{x} - x_{\parallel}\hat{\boldsymbol{n}}$. The in-plane momentum $k_{\parallel}$ remains a good quantum number and

we ignore the terms proportional to $\boldsymbol{k}_\parallel$ in the Hamiltonian for now. The momentum k_n is not a good quantum number, so we replace it by $k_n \to -i\partial_n$. Then we get the Hamiltonian

$$H_0 = M\tau_z - iA\partial_n\sigma_n\tau_x. \tag{2.24}$$

Proceeding similar to the Chern insulator, we use a mass profile $M = M(r_n)$ which changes its sign from $M > 0$ for $r_n < w$ to $M < 0$ for $r_n > w$. The zero-energy state Ψ_0 is obtained from eigenvalue equation

$$H_0\Psi_0 = 0. \tag{2.25}$$

Multiplying the equation by τ_z from the left yields

$$(M + A\partial_n\sigma_n\tau_y)\Psi_0 = 0. \tag{2.26}$$

To get exponentially decaying solutions, Ψ_0 has to an eigenstate of $\sigma_n\tau_y$ with eigenvalue -1. We decompose the solution into the combined spin-position part and the orbital degree of freedom part as

$$|\Psi_{0,\pm}\rangle = |\psi_\pm\rangle \otimes |\tau_y = \mp\rangle\,. \tag{2.27}$$

Here the spin-position part $\psi_\pm(r_n)$ is found as

$$\psi_\pm(r_n) = \langle r_n|\psi_\pm\rangle = Ne^{\int_w^{r_n} M(r_n')/A dr_n}\,|\sigma_n = \pm\rangle \tag{2.28}$$

and the ± 1 eigenstates of σ_n and τ_y are denoted by the repsective kets in the equations above.

In contrast to the Chern insulator we now have a two-dimensional zero-energy subspace because we have the additional spin degree of freedom. Projecting the full Hamiltonian $H_0 + Ak_\parallel\sigma_\parallel\tau_x$ into the two-dimensional zero-energy subspace yields

$$H_{\text{surface}} = A(\boldsymbol{\sigma} \times \boldsymbol{k}_\parallel) \cdot \hat{\boldsymbol{n}}, \tag{2.29}$$

where the surface structure enters through $\hat{\boldsymbol{n}}$ into the model. In the projected surface subspace, there is a one-to-one correspondence between the spin orientation and the orbital composition due to the state's structure given in (2.27). Thus, the orbital degree of freedom becomes redundant information, allowing us to label the basis states solely by their spin.

The resulting surface Hamiltonian in (2.29) is a massless Dirac Hamiltonian in two dimensions, namely the in-plane surface dimensions, with the Dirac velocity determined by the parameter A. For example, a flat surface with $\hat{\boldsymbol{n}} = \boldsymbol{e}_z$ yields the spectrum

$$E_{\boldsymbol{k},\pm} = \pm A|\boldsymbol{k}_\parallel|, \tag{2.30}$$

which is a Dirac cone.

The surface states exhibit a property referred to as spin-momentum locking. For a fixed energy ε, the momentum magnitude is constrained to $|\boldsymbol{k}_{\parallel}| = \varepsilon/A$, leaving its polar angle ϕ as the only degree of freedom. In this representation, the surface Hamiltonian becomes

$$H_{\text{surface}} = \varepsilon\sigma_{\phi} \tag{2.31}$$

where $\sigma_{\phi} = -\sin\phi\sigma_x + \cos\phi\sigma_y$. Since the physical state is an eigenvector of σ_{ϕ} with eigenvalue $+1$, the spin orientation is uniquely determined by the momentum direction ϕ. If the direction of the momentum is inverted this leads to $\sigma_{\phi} \to -\sigma_{\phi}$ which means the $+1$ eigenstate has the opposite spin of the original direction. Therefore, the spin direction is locked to momentum direction and the surface states are also referred to as helical surface states.

Finally, we discuss the time-reversal invariance of the BHZ model which is the critical ingredient responsible for the emergence of the Dirac cone spectrum. The BHZ Hamiltonian is invariant under the time-reversal operator $\mathcal{T} = i\sigma_y K$, with the complex conjugation operator K. The time-reversal operator satisfies $\mathcal{T}^2 = -1$ for fermions. Due to Kramer's theorem, there must be a time-reversed partner with opposite spin and momentum for the surface state.

Furthermore, at the time reversal invariant momentum $\boldsymbol{k}_{\parallel} = 0$ the $\mathcal{T}$-symmetry gives rise to a degeneracy which enforces a crossing point in the surface spectrum. Therefore, the gapless surface modes are protected by the $\mathcal{T}$-symmetry and remain robust against any perturbation respecting the $\mathcal{T}-$symmety. This symmetry can be broken, for instance by an external magnetic field.

2.4 Magnetic fields and spectral flow

In this section we treat the framework of magnetic fields in quantum mechanics, introducing core concepts and using simple examples which we can leverage in the course of the subsequent chapters.

In quantum mechanics, magnetic fields have a different effect than in classical mechanics. Similar considerations can be made for electric fields, but for the purpose of this work we are solely interested in magnetic fields. The magnetic field $\boldsymbol{B}$ does not enter directly in the Hamiltonian. Instead it enters via its vector potential $\boldsymbol{A}$ which fulfills $\boldsymbol{B} = \nabla \times \boldsymbol{A}$. For a particle of charge q we use minimal coupling substitution $\boldsymbol{p} \to \boldsymbol{p} - q\boldsymbol{A}$ into the Hamiltonian without any magnetic field.

At first it might seem unphysical to use the vector potential because the magnetic field remains invariant under gauge transformations, whereas the vector potential transforms as $\boldsymbol{A} + \nabla\chi$, thus changing the Hamiltonian. However, let us consider an arbitrary time independent Hamiltonian with some time independent vector potential $\boldsymbol{A}$. The Hamiltonian depends on the components of the momentum operator p_i and any other degrees of freedom as position or spin $\{x_i, S_i\}$. We denote the Hamiltonian as $H(\{p_i - qA_i\}, \{x_i, S_i\})$. The eigenstates fulfill the time-independent Schrödinger equation

$$H(\{p_i - qA_i\}, \{x_i, S_i\}) \left|\psi\right\rangle = E \left|\psi\right\rangle . \tag{2.32}$$

If we now perform a gauge transformation $\boldsymbol{A} \to \boldsymbol{A'} = \boldsymbol{A} + \nabla\chi$ we have

$$H'(\{p_i - qA'_i\}, \{x_i, S_i\}) \left|\psi'\right\rangle = E \left|\psi'\right\rangle , \tag{2.33}$$

where the Hamiltonian and the states transform under the gauge, but the energies have to remain the same as we still describe the same magnetic field $\boldsymbol{B}$.

Simply using that the gauge transformation function $\chi(\boldsymbol{x})$ only depends on the position, implies its commutation with all the degrees of freedom in the Hamiltonian, except for the momentum. From the operator relation

$$[p_i, f(\boldsymbol{x})] = -i\hbar\nabla_i f(\boldsymbol{x}) \tag{2.34}$$

it follows that

$$(p_i - qA_i)e^{i\frac{q}{\hbar}\chi} = e^{i\frac{q}{\hbar}\chi}\left(p_i - qA_i + q\nabla_i\chi\right). \tag{2.35}$$

Thus, we can show that the state $\left|\psi'\right\rangle$, that solves the gauge transformed system (2.33), is related to $\left|\psi\right\rangle$ by

$$\left|\psi'\right\rangle = e^{i\frac{q}{\hbar}\chi} \left|\psi\right\rangle . \tag{2.36}$$

This shows that the gauge transformation only leads to a local phase factor for the wavefunction. Moreover, physically relevant expectation values,

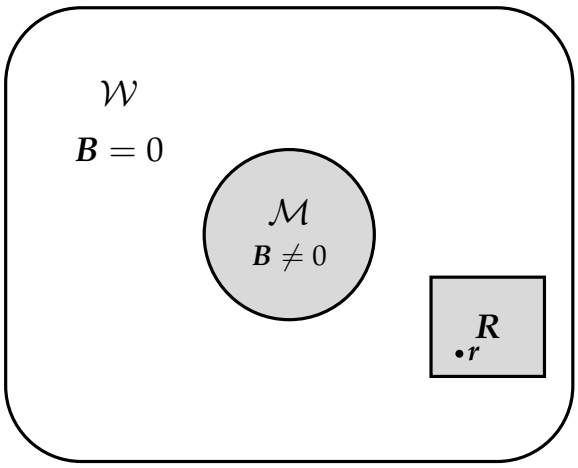

FIGURE 2.1: Spatial and magnetic field configuration for the derivation of the Aharonov-Bohm effect. The field-free region is denoted by $\mathcal{W}$ and the solenoid region by $\mathcal{M}$. The particle at position $\boldsymbol{r}$ is restricted to a box with center position $\boldsymbol{R} \in \mathcal{W}$ by a confining potential $V(\boldsymbol{r} - \boldsymbol{R})$.

such as $\langle\psi|\, \boldsymbol{p} - q\boldsymbol{A}\, |\psi\rangle$ and $\langle\psi|\, \boldsymbol{x}\, |\psi\rangle$ remain invariant under gauge transformations. Here, we introduce the kinetic momentum $\boldsymbol{\pi} = \boldsymbol{p} - q\boldsymbol{A}$ which is known from the classical description of a particle in a magnetic field and is related to the velocity of the particle by $\boldsymbol{v} = \boldsymbol{\pi}/m$, unlike the canonical momentum $\boldsymbol{p}$. Additionally, the kinetic angular momentum is defined via $\boldsymbol{L}^{\text{kin}} = \boldsymbol{r} \times \boldsymbol{\pi}$.

With the knowledge on gauge transformations at hand we treat the Aharonov-Bohm effect effect, an effect which only occurs in quantum mechanics. For simplicity, we restrict the description to a particle of charge q in a two-dimensional plane. For the setup, we consider a solenoid in some region $\mathcal{M}$, in which the magnetic field in z-direction $\boldsymbol{B}$ is non-zero. Outside the solenoid, in the region $\mathcal{W}$, we have $\boldsymbol{B} = 0$. The region $\mathcal{W}$ is where the particle is allowed to move in. However, we restrict the particle to a box in the vicinity of $\boldsymbol{R} \in \mathcal{W}$ which is described by a confining potential $V(\boldsymbol{r} - \boldsymbol{R})$, with the particle's position $\boldsymbol{r}$. This setup is depicted in Fig. 2.1.

The Hamiltonian without a magnetic field reads

$$H(\boldsymbol{R}) = \frac{\boldsymbol{p}^2}{2m} + V(\boldsymbol{r} - \boldsymbol{R}). \tag{2.37}$$

The groundstate of $H(\boldsymbol{R})$ is denoted by

$$\langle \boldsymbol{r}|\psi(\boldsymbol{R})\rangle = \psi(\boldsymbol{r} - \boldsymbol{R}) \tag{2.38}$$

with eigenenergy E.

If we place the box at some $\boldsymbol{R}$, and therein the particle, the energies are described by the free Hamiltonian $H(\boldsymbol{R})$, without any magnetic field. This is not only the case due to the particle moving in the field free region, but

due to the confining potential it cannot move in a closed loop around the solenoid. Therefore, the particle does not "feel" the magnetic flux caused by the solenoid because it does not enclose it. The latter can be compared to the example of a particle on a ring, enclosing a magnetic flux which we treat in the next section.

Although the Hamiltonian $H(\boldsymbol{R})$ yields the correct energies, it does not capture the magnetic field via minimal coupling which the actual Hamiltonian for the setup

$$H'(\boldsymbol{R}) = \frac{(\boldsymbol{p} - q\boldsymbol{A})^2}{2m} + V(\boldsymbol{r} - \boldsymbol{R}) \tag{2.39}$$

does. Therefore, we have not found the eigenstates yet.

To obtain the solution to $H'(\boldsymbol{R})$, we use the fact that the field vanishes for the region outside of the solenoid, so that $\boldsymbol{A} = \boldsymbol{\nabla}\Lambda$ with some scalar potential $\Lambda(\boldsymbol{r})$. The particle is restricted to the box which is a simply connected region, allowing the use of a scalar potential. Thus, we can use the gauge transformation $\chi(\boldsymbol{r}) = \Lambda(\boldsymbol{r})$ in equation (2.36) to obtain the groundstate of $H'(\boldsymbol{R})$ from the groundstate of $H(\boldsymbol{R})$. Putting this together, the groundstate of $H'(\boldsymbol{R})$ in the position basis reads

$$\psi'(\boldsymbol{r} - \boldsymbol{R}) = e^{i\frac{q}{\hbar}\Lambda(\boldsymbol{r})}\psi(\boldsymbol{r} - \boldsymbol{R}). \tag{2.40}$$

We emphasize that the gauge transformation cannot change the energy spectrum. Therefore, it is crucial to start from the field free case which correctly describes the energies as argued above, and incorporating the magnetic field only via a phase.

The scalar potential is given by

$$\Lambda(\boldsymbol{r}) = \int_{\boldsymbol{R}}^{\boldsymbol{r}} d\boldsymbol{r}' \cdot \boldsymbol{A}(\boldsymbol{r}'). \tag{2.41}$$

Choosing the reference point $\boldsymbol{R}$ makes sure the phase of $\psi'(\boldsymbol{r} - \boldsymbol{R})$ does not change if we move the box around the solenoid, so the state returns to itself without picking up a phase. If we choose a fixed reference point the state picks up a phase but the overall result which we obtain below, is the same.

Suppose the box is moved adiabatically in a circle $\mathcal{C}$ around the solenoid. Following the framework of section 2.1, we can calculate the Berry phase accumulated by the wavefunction for this path. In this case, the parameter of the Hamiltonian is the position of the box $\boldsymbol{R}(t)$. Using equation (2.6) for the Berry phase of the groundstate $|\psi'(\boldsymbol{R})\rangle$ of $H'(\boldsymbol{R})$, we have to calculate

$$\langle\psi'(\boldsymbol{R})|\,\boldsymbol{\nabla}_{\boldsymbol{R}}\,|\psi'(\boldsymbol{R})\rangle = -\frac{i}{\hbar}\langle\psi(\boldsymbol{R})|\,\boldsymbol{p}\,|\psi(\boldsymbol{R})\rangle - \frac{iq}{\hbar}\boldsymbol{A}(\boldsymbol{R}). \tag{2.42}$$

The expectation value of the momentum in the steady state $|\psi(\boldsymbol{R})\rangle$ vanishes and therefore we obtain for the Berry phase

$$\gamma = i\oint_{\mathcal{C}} d\boldsymbol{R} \cdot \langle\psi'(\boldsymbol{R})|\,\boldsymbol{\nabla}_{\boldsymbol{R}}\,|\psi'(\boldsymbol{R})\rangle = \frac{q}{\hbar}\int_{\mathcal{M}} d\boldsymbol{S} \cdot \boldsymbol{B} = \frac{q\Phi}{\hbar}. \tag{2.43}$$

In this setup the Berry phase is called the Aharonov-Bohm phase which the wavefunction picks up as it follows the path $\mathcal{C}$.

We can also choose any open path we want and the particle picks up a phase corresponding to the Berry phase.

Finally, we want to introduce the notion of spectral flow. For this we consider a simple example of a particle of charge q on ring of radius R with an infinitesimally thin solenoid at the origin. This magnetic field configuration is called Aharonov-Bohm field and is given by

$$\boldsymbol{B} = -\Phi\delta^{(2)}(\boldsymbol{r})\boldsymbol{e}_z \tag{2.44}$$

with the magnetic flux Φ and the d-dimensional delta function $\delta^{(d)}(\boldsymbol{r})$. The corresponding vector potential reads

$$\boldsymbol{A} = -\frac{\Phi}{2\pi r}\boldsymbol{e}_\phi \tag{2.45}$$

using cylindrical coordinates r, ϕ, z.

The Hamiltonian with minimal coupling reads

$$H = \frac{\left(p_\phi - qA_\phi\right)^2}{2m}, \tag{2.46}$$

where the only degree of freedom is the polar angle ϕ with corresponding canonical momentum $p_\phi = -i\hbar/R\partial_\phi$.

It is simple to show that the Hamiltonian is symmetric under rotations around the z-axis, namely $[H, L_z] = 0$. Here $L_z = Rp_\phi$ is the canonical angular momentum which only has a single component because the system is two-dimensional. Therefore, the eigenstates of the Hamiltonian are given by the eigenstates of L_z which are $e^{il\phi}$ with magnetic quantum number $l \in \mathbb{Z}$, making the eigenstates single-valued. From this, we obtain the corresponding eigenenergies

$$E_l(g) = \frac{\hbar^2}{2mR^2}\left(l + g\right)^2 = \frac{\hbar^2}{2mR^2}\varepsilon_n(g) \tag{2.47}$$

with $g = \Phi/\Phi_0$, where the flux is in units of the magnetic flux quantum $\Phi_0 = h/q$.

The particle is always in a region with $\boldsymbol{B} = 0$, so it is not directly influenced by the local magnetic field but rather it is influenced by the magnetic flux Φ it encloses. Therefore, it is important that the region the particle moves in encloses the magnetic flux for its energy levels to be influenced by the magnetic field. This stands in contrast to the aforementioned Aharonov-Bohm configuration, in which the energy spectrum remains invariant under the magnetic field because the particle is restricted to a domain that does not enclose the magnetic flux.

With the spectrum calculated, we can study how the energy levels and states evolve under variation of the magnetic flux Φ. This is depicted in

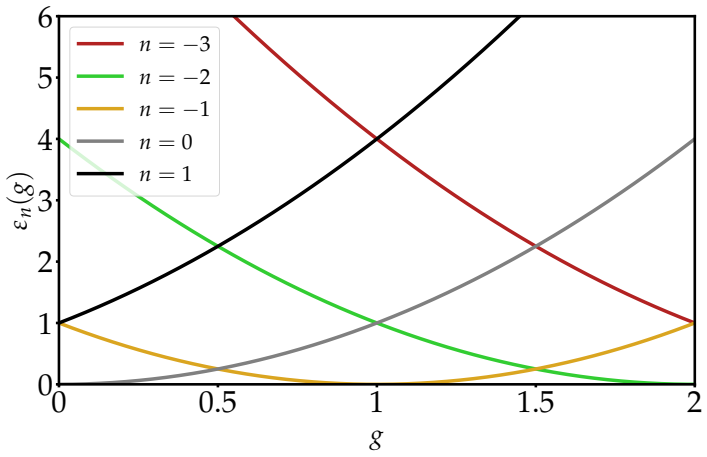

FIGURE 2.2: Dimensionless energies $\varepsilon_n(g)$ for the angular momenta $n = -3, -2, -1, 0, 1$ as a function of the dimensionless magnetic flux $g \in [0, 2]$. It can be observed that the spectrum is periodic in $g \in \mathbb{Z}$ so the respective states are mapped onto each other.

Fig. 2.2. First, it can be seen that the overall spectrum does not change if a flux quantum is inserted, so $g \to g + 1$. In contrast to the overall spectrum remaining the same, the underlying states undergo a systematic rearrangement during this process, e.g. smoothly mapping each state to its adjacent energy level starting from $g = 0$. The state itself remains unchanged but is now associated to a different energy, namely it flows in the spectrum. This can be described by $E_l(g + 1) = E_{l+1}(g)$ and marks the spectral flow.

Chapter 3

Dirac disc in an Aharonov-Bohm field

In this chapter, we determine the 3D TI surface states and spectral flow for a planar disc pierced by a continuously variable Aharonov-Bohm flux. As shown in Ch. 4, this is the local flat-space limit of the Dirac sphere problem which is studied numerically in Ch. 4.3 of Ref. [5]. The goal is to identify the central problem that occurs for fractional flux values for a singular flux string and resolve it by finding a regularization procedure. By studying this simplified planar model, we establish the regularization to analytically solve the surface states and spectral flow for the Dirac sphere in Ch. 4.

3.1 Model setup

To describe the surface states of the 3D BHZ model we use the Dirac Hamiltonian given in Eq. (2.29) which we derived for arbitrary surfaces in Ch. 2. The Dirac Hamiltonian of a massless particle with electrical charge $q > 0$ on a planar surface with normal $\hat{\boldsymbol{n}} = \boldsymbol{e}_z$ is given by

$$H_{\mathrm{D}} = v\left[\boldsymbol{\sigma} \times (\boldsymbol{p} - q\boldsymbol{A})\right] \cdot \boldsymbol{n}, \tag{3.1}$$

where v is the velocity, $\boldsymbol{p}$ the canonical momentum and $\boldsymbol{\sigma} = (\sigma_x, \sigma_y, \sigma_z)^T$ is the vector of Pauli matrices because the particle has spin-$\frac{1}{2}$. The magnetic field is included via minimal coupling using the vector potential $\boldsymbol{A}$.

The magnetic field of the Aharonov-Bohm flux is given by

$$\boldsymbol{B} = -\Phi\delta^{(2)}(\boldsymbol{r})\boldsymbol{e}_z, \tag{3.2}$$

where Φ is the magnetic flux. The corresponding vector potential reads

$$\boldsymbol{A} = -\frac{\Phi}{2\pi r}\boldsymbol{e}_\phi \tag{3.3}$$

using cylindrical coordinates r, ϕ, z.

We have already encountered this vector potential in Ch. 2, studying a particle on a ring. The difference for the Dirac disc is that it includes the origin and therefore the Dirac delta function's divergence. In the next section, we see how this becomes problematic when solving the eigenvalue problem

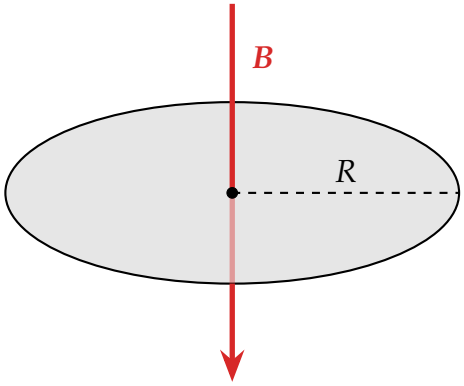

FIGURE 3.1: Depiction of the Dirac disc model. A two-dimensional circular plane of radius R which the particle is restricted to via the hard-wall boundary condition given by Eq. (3.10). The disc is pierced by an Aharonov-Bohm flux of strength $-\Phi$ indicated by the red arrow. The magnetic field points towards the negative z-direction for $-\Phi < 0$.

for H_D due to the emergence of an additional solution in a specific angular momentum subspace.

Rewriting the Hamiltonian H_D in position space, using $\boldsymbol{p} = -i\hbar\boldsymbol{\nabla}$ and polar coordinates, we obtain

$$H_\mathrm{D} = \hbar v \begin{pmatrix} 0 & e^{-i\phi}\left(\partial_r - i/r\partial_\phi + g/r\right) \\ e^{i\phi}\left(-\partial_r - i/r\partial_\phi + g/r\right) & 0 \end{pmatrix} \tag{3.4}$$

with the dimensionless flux $g = \Phi/\Phi_0 \in \mathbb{R}$ in units of the magnetic flux quantum, which is defined as $\Phi_0 \equiv h/q$.

As we are describing a spin-$\frac{1}{2}$ particle, the total angular momentum operator is given by $J = L_z + S_z$. Here $L_z = yp_x - xp_y$ is the z-component of the canonical angular momentum and $S_z = \frac{\hbar}{2}\sigma_z$ the z-component of the spin. Thus, the total angular momentum quantum number is quantized with $j = \pm\frac{1}{2}, \pm\frac{3}{2}, \ldots$.

The Hamiltonian H_D is symmetric under rotations generated by the total angular momentum so we have $[H_\mathrm{D}, J] = 0$. Thus, we can write the eigenstates of H_D as simultaneous eigenstates of J. The eigenstates of J with eigenvalues $\hbar j$ are given by

$$\zeta(\phi) = \frac{1}{\sqrt{4\pi}} e^{i(j-1/2)\phi} \begin{pmatrix} 1 \\ e^{i\phi} \end{pmatrix}. \tag{3.5}$$

In the following, we use the quantum number $n = j - 1/2 \in \mathbb{Z}$ to label the different total angular momentum sectors. This is the quantum number of the canonical angular momentum of the spin-up component. This implies the general form

$$\psi_n(r,\phi) = e^{in\phi} \begin{pmatrix} \chi_{1,n}(r) \\ \chi_{2,n}(r)\, e^{i\phi} \end{pmatrix} \tag{3.6}$$

for eigenstates of H_D, absorbing the normalization into the radial spinor components.

The particle is confined to a disc of radius R which maintains the rotational symmetry we have identified. To include the finiteness of the disc, we employ a hard-wall boundary condition. This is known from, e.g., a particle in an infinite potential well in one dimension and leads to the wavefunction vanishing at the left and right boundary. However, in the case of the Hamiltonian H_D the hard-wall leads to a non-trivial condition for the radial spinors.

The hard-wall boundary condition is achieved by adding a potential term to the Hamiltonian (3.1) which reads

$$H_\mathrm{D} \mapsto H_\mathrm{D} + \Delta(r)\sigma_z. \tag{3.7}$$

The potential is $\Delta(r) = \Delta\Theta(r-R)$, where $\Theta(x)$ is the Heaviside stepfunction and $\Delta \to \infty$. The additional term gaps out the modes for $r > R$ and preserves the symmetry with respect to the total angular momentum J. To see how the additional term influences the states, we write down the eigenvalue problem for $r > R$:

$$(H_\mathrm{D} + \Delta\sigma_z)\psi^\mathrm{out}(r,\phi) = E\psi^\mathrm{out}(r,\phi). \tag{3.8}$$

Using Eq. (3.4) and $\Delta \to \infty$, we obtain the radial equations

$$\partial_r \chi_2^\mathrm{out}(r) = -\Delta\chi_1^\mathrm{out}(r), \tag{3.9a}$$

$$-\partial_r \chi_1^\mathrm{out}(r) = \Delta\chi_2^\mathrm{out}(r), \tag{3.9b}$$

which yield the radial spinor

$$\boldsymbol{\chi}^\mathrm{out}(r) = e^{-\frac{\Delta}{\hbar v}r}\begin{pmatrix}1\\1\end{pmatrix}. \tag{3.10}$$

The limit $\Delta \to \infty$ has not been performed yet. Keeping Δ finite, it can be seen that the upper and lower spinor component must be equal. The exponential factor cancels when taking the ratio of the two components, so this condition remains valid for $\Delta \to \infty$.

By matching the radial eigenspinors of H_D for $r < R$ with $\boldsymbol{\chi}^\mathrm{out}(r)$ at $r = R$, the hard-wall boundary condition is obtained as

$$\chi_{1,n}(R) = \chi_{2,n}(R). \tag{3.11}$$

3.2 Spectrum and eigenstates

In this section, we want to solve the eigenvalue problem for H_D inside the disc. To obtain the spectrum of the Hamiltonian, we calculate the eigenstates of H_D of arbitrary energy E which is then quantized by applying the boundary condition (3.11). The eigenvalue equation reads

$$H_\mathrm{D}\boldsymbol{\psi}_n = E_n\boldsymbol{\psi}_n, \tag{3.12}$$

for arbitrary $n \in \mathbb{Z}$. Here, we have used the ansatz (3.6) due to the symmetry with respect to J, allowing us to solve the eigenvalue problem in each total angular momentum subspace n separately.

From Eq. (3.4), we obtain the coupled equations for the radial part given by

$$\left(\partial_r + \frac{n+1+g}{r}\right)\chi_{2,n}(r) = k\chi_{1,n}(r) \tag{3.13}$$

$$\left(-\partial_r + \frac{n+g}{r}\right)\chi_{1,n}(r) = k\chi_{2,n}(r) \tag{3.14}$$

with the wavenumber $k \equiv \frac{E}{\hbar v}$, dropping the index n. For the following derivation the index n for the energy and wavevector is omitted. Decoupling the two equations yields Bessel's differential equation

$$r^2\partial_r^2\chi_{1,n}(r) + r\partial_r\chi_{1,n}(r) + (k^2r^2 - (n+g)^2)\chi_{1,n}(r) = 0. \tag{3.15}$$

A brief review of the Bessel functions and the corresponding differential equation is given in App. A.

In the case of $g \notin \mathbb{Z}$, we obtain the solution

$$\chi_{1,n}(r) = A_n J_{n+g}(|k|r) + B_n J_{-(n+g)}(|k|r). \tag{3.16}$$

Here, $J_\nu(x)$ is the Bessel function of the first kind of order $\nu \in \mathbb{R}$, defined in App. A. The solution for $\chi_2(r)$ can then be obtained using Eq. (3.14) which then yields

$$\chi_{2,n}(r) = A_n J_{n+g+1}(|k|r) - B_n J_{-(n+g+1)}(|k|r). \tag{3.17}$$

From now on, we focus on positive energy spectrum $E > 0$. The solutions for $E < 0$ exhibit qualitatively similar behavior and offer no additional insights. Restricting our focus to $E > 0$ thus allows for a more concise presentation.

To obtain physically acceptable solutions, the radial spinor must be normalizable. In particular, we require that the radial spinor's components vanish sufficiently fast at the origin. Using the limiting behavior of the Bessel function for small arguments yields

$$\lim_{r\to 0} r\left[J_\nu(r)\right]^2 \propto r^{1+2\nu}, \tag{3.18}$$

where the factor r stems from the polar integral measure. The latter is only integrable at $r = 0$ if $\nu > -1$ which is the constraint we apply to the general solutions (3.16) and (3.17).

To complete the discussion, we turn to the case of $g \in \mathbb{Z}$. In this case, the radial spinor solution contains $Y_\nu(kr)$ which is the Bessel function of the second kind of order $\nu \in \mathbb{Z}$, see App. A. These are non-normalizable so they have to be discarded. If we set $g \in \mathbb{Z}$ in our solution obtained for $g \notin \mathbb{Z}$, we can use the property $J_{-n}(x) = (-1)^n J_n(x)$ for $n \in \mathbb{Z}$. Thus, we see that the solution for $g \notin \mathbb{Z}$ is also valid for the case $g \in \mathbb{Z}$.

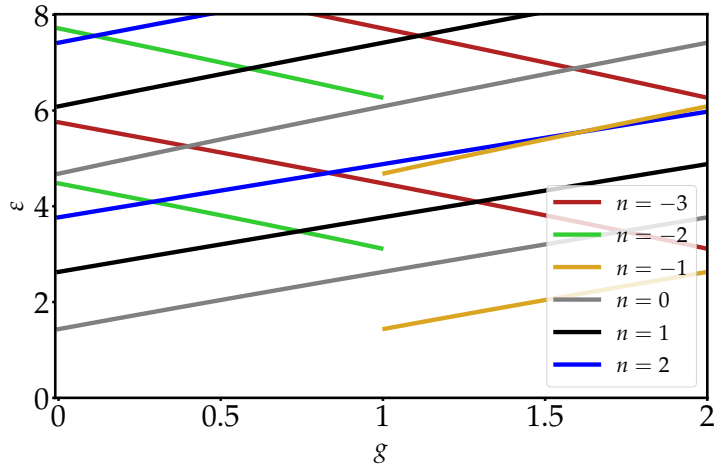

FIGURE 3.2: Dimensionless energies of angular momenta $n = -3, -2, -1, 0, 1, 2$ as function of the magnetic flux ratio $g \in [0, 2]$. The higher the energy for a fixed n, the higher is the corresponding radial quantum number z. Here, we observe that the energies increase and decrease approximately linearly with the magnetic flux g, whereas the spectrum is periodic in $g \in \mathbb{Z}$. The states with $n > n^*$ increase with g, whereas the states with $n < n^*$ decrease with g.

Turning back to $g \notin \mathbb{Z}$, we decompose the dimensionless flux $g = l + \gamma$ into its integer part $l \in \mathbb{Z}$ and its fractional part $\gamma \in (0, 1)$. Consequently, we obtain the solutions

$$\boldsymbol{\psi}_n(r, \phi) = N_n e^{in\phi} \begin{pmatrix} J_{-n-l-\gamma}(kr) \\ -J_{-n-1-l-\gamma}(kr)\, e^{i\phi} \end{pmatrix} \text{, for } n < -l - 1 \tag{3.19}$$

and

$$\boldsymbol{\psi}_n(r, \phi) = N_n e^{in\phi} \begin{pmatrix} J_{n+l+\gamma}(kr) \\ J_{n+1+l+\gamma}(kr)\, e^{i\phi} \end{pmatrix} \text{, for } n > -l - 1. \tag{3.20}$$

However, in the angular momentum subspace $n^* \equiv -l - 1$ two solutions are admitted by the normalization constraint and the spinor reads

$$\boldsymbol{\psi}_{n^*}(r, \phi) = N_{n^*} e^{-i(l+1)\phi} \begin{pmatrix} A\, J_{-1+\gamma}(kr) + B\, J_{1-\gamma}(kr) \\ [A J_\gamma(kr) - B\, J_{-\gamma}(kr)]\, e^{i\phi} \end{pmatrix}. \tag{3.21}$$

This state differs from the other angular momenta $n \neq n^*$ because it is square-integrable at the origin, but divergent in both components which means the particle is localized around the Aharonov-Bohm flux. Therefore, we call n^* the critical angular momentum subspace.

For $n \neq n^*$ we can calculate the spectrum of the Hamiltonian for $g \notin \mathbb{Z}$ by using the boundary condition (3.10). This yields

$$J_{-n-l-\gamma}(kR) = -J_{-n-1-l-\gamma}(kR), \text{for } n < -l - 1, \tag{3.22a}$$

$$J_{n+l+\gamma}(kR) = J_{n+1+l+\gamma}(kR), \text{for } n > -l - 1. \tag{3.22b}$$

We define the dimensionless energy $\varepsilon \equiv kR$. For given n and g the roots of the respective equation in (3.22) yield the dimensionless energies $\varepsilon_{n,z}(g)$. Therein, $z \in \mathbb{N}$ labels the distinct roots which we define as the radial quantum number. The energy is then given by $E_{n,z}(g) = \frac{\hbar v}{R}\varepsilon_{n,z}(g)$ which reveals the scaling $E \propto 1/R$.

In Fig. 3.2, the dimensionless energies are shown for a few angular momenta $n \neq n^*$ and their first radial quantum numbers $z = 1, 2$. High-energy states are omitted for clarity, as the number of energy levels increases with energy, making the plot visually crowded.

Here, we observe that the energies increase and decrease approximately linearly with the magnetic flux g. For a fixed integer part of the flux l we see that all states $n < n^*$ decrease in energy, whereas all the states with $n > n^*$ increase in energy.

Aside from the direction of the energy shift, this behavior reflects how the flux effectively shifts the total kinetic angular momentum

$$J^{\text{kin}} = (\boldsymbol{r} \times [\boldsymbol{p} - q\boldsymbol{A}]) \cdot \boldsymbol{e}_z + S_z = J + \hbar g. \tag{3.23}$$

For example, as g increases from 0 to 1, the total kinetic angular momentum quantum number $j + g$ smoothly shifts from the integer j towards $j + 1$. This results in a continuous evolution of the energy levels that resembles moving into the next higher total angular momentum channel. This concept can be extended to arbitrary evolutions $g = l$ to $g = l + 1$. Therefore, the spectrum returns to itself and is periodic in $g \in \mathbb{Z}$. We expect this periodicity, similar to the particle on a ring with an AB-flux treated in Sec. 2.4.

We know that the critical state n^* also has to obey this periodicity. As the flux is increased adiabatically from $g = l$ to $g = l + 1$, the respective critical state in that regime turns from $n < n^*$ at the beginning to $n > n^*$ at the end, while inbetween $n = n^*$. Consequently, the corresponding energy has to transition from decreasing to increasing with g in the process. Thus, we have made a prediction about the critical subspace's energy evolution with g without any calculation so far.

Next, we consider the critical subspace n^*. In this case the hard-wall boundary condition does not yield the energy because we still have two integration constants left in the spinor given in Eq. (3.21).

To solve the problem of not being able to determine the energy, it is necessary to impose an appropriate boundary condition at $r = 0$ for the radial spinor in the critical subspace where $n = n^*$. This boundary condition uniquely determines the ratio A/B. The determination of such boundary conditions can be treated using the theory of self-adjoint extensions (SAEs), as demonstrated in Ref. [15]. Therein, the same model is treated, but with a mass term $m\sigma_z$ included.

In this thesis, we do not explicitly deal with SAEs and rather refer the interested reader to Ref. [15]. This is because the problem with the SAE approach is that it yields an infinite set of possible boundary conditions at $r = 0$, continuously parametrized by an SAE parameter. Consequently, each SAE parameter choice and its associated boundary condition yield a distinct set of

energy eigenvalues for the critical subspace. However, in reality only a single choice must be fixed by physical constraints. Therefore, the SAE parameter encodes all relevant physical information, yet it remains undetermined.

To eliminate this ambiguity and single out the unique, physically permissible boundary condition, we turn to numerical methods. Because the energy spectrum of the critical subspace has not yet been determined analytically, we compute the system's energies using a discrete lattice model implemented in `Kwant` [16]. Unlike the continuum model, the lattice model naturally yields an unambiguous energy spectrum. By extracting the energies from this numerical lattice model, we aim to derive a corresponding regularized model for the continuum theory. This physically grounded regularization will allow us to uniquely determine the boundary condition at the origin.

3.3 Lattice model

To be able to simulate the system using `Kwant`, a lattice version of the Dirac Hamiltonian (3.1) is required. We use a regular square lattice in two dimensions with constant lattice spacing a. We start by deriving the lattice version of the Hamiltonian given by (3.1) with magnetic vector potential $\boldsymbol{A} = 0$.

For this purpose, we replace $p_j = -i\hbar\partial_j$ with $j = x, y$ and discretize the derivative. Only considering nearest neighbor couplings we obtain

$$\partial_j \psi(\boldsymbol{x}) \approx \frac{1}{2a} \left(\langle \boldsymbol{x_n} + a\boldsymbol{e}_j | \psi \rangle - \langle \boldsymbol{x_n} - a\boldsymbol{e}_j | \psi \rangle \right), \tag{3.24}$$

yielding

$$\partial_j \to \frac{1}{2a} \sum_{\boldsymbol{n}} \left(|\boldsymbol{x_n}\rangle\langle \boldsymbol{x_n} + a\boldsymbol{e}_j| - |\boldsymbol{x_n}\rangle\langle \boldsymbol{x_n} - a\boldsymbol{e}_j| \right). \tag{3.25}$$

Thus, the Hamiltonian on the lattice reads

$$H_{\mathrm{D}}^{\mathrm{lat}} = \sum_{\boldsymbol{n}} i\frac{A}{2} \left(\sigma_x |\boldsymbol{x_n} + a\boldsymbol{e}_y\rangle\langle \boldsymbol{x_n}| - \sigma_y |\boldsymbol{x_n} + a\boldsymbol{e}_x\rangle\langle \boldsymbol{x_n}| \right) + \mathrm{h.c.}, \tag{3.26}$$

where $A = \hbar v / a$.

Due to the periodicity of the lattice we can employ Bloch's theorem to diagonalize (3.26). The lattice Hamiltonian is invariant under the transformation

$$\boldsymbol{x_n} \to \boldsymbol{x_n} + a\boldsymbol{e}_j, \quad j = x, y. \tag{3.27}$$

Therefore, for the Bloch state in discrete space the ansatz

$$|\psi_{\boldsymbol{k}}\rangle = \sum_{\boldsymbol{n}} e^{i\boldsymbol{k}\cdot\boldsymbol{x_n}} \boldsymbol{u_k} |\boldsymbol{x_n}\rangle \tag{3.28}$$

with $\boldsymbol{u_k} \in \mathbb{C}^2$ is chosen. Here, the crystal-momentum is restricted to the first Brillouin zone $k_j \in \left(-\frac{\pi}{a}, \frac{\pi}{a}\right]$. Thus, the lattice Bloch Hamiltonian is obtained

as

$$H_{\mathrm{D}}^{\mathrm{Bloch}} = A\left[\sigma_x \sin(k_y a) - \sigma_y \sin(k_x a)\right] \tag{3.29}$$

with the corresponding spectrum

$$E_{\pm}(\boldsymbol{k}) = \pm A\sqrt{\sin^2(k_x a) + \sin^2(k_y a)}. \tag{3.30}$$

When using the lattice Hamiltonian to approximate the continuum Dirac model, we encounter the problem of fermion doubling. Besides the Dirac point at $\boldsymbol{k} = 0$, there are three additional Dirac points at $\boldsymbol{k} = (\pi/a, 0), (0, \pi/a)$, $(\pi/a, \pi/a)$. At all points, the spectrum is linear and resembles a Dirac fermion, resulting in a total of four Dirac cones. The additional Dirac cones which are not at $\boldsymbol{k} = \boldsymbol{0}$ are called fermion doublers.

This doubling phenomenon is a well-known artifact of discretizing the Dirac equation. To circumvent this, we add another term to our Bloch Hamiltonian on the lattice. The modified Bloch Hamiltonian reads

$$H_{\mathrm{D}}^{\mathrm{Bloch}} = A\left[\sigma_x \sin(k_y a) - \sigma_y \sin(k_x a)\right] + B\sigma_z\left[2 - \cos(k_x a) - \cos(k_y a)\right] \tag{3.31}$$

with the corresponign spectrum

$$E_{\pm}(\boldsymbol{k}) = \pm\sqrt{A^2\left[\sin^2(k_x a) + \sin^2(k_y a)\right] + B^2\left[2 - \cos(k_x a) - \cos(k_y a)\right]^2}. \tag{3.32}$$

Expanding the Hamiltonian around $\boldsymbol{k} = \boldsymbol{0}$

$$H_{\mathrm{D}}^{\mathrm{Bloch}} = Aa(\sigma_x k_y - \sigma_y k_x) + \frac{B}{2}a^2\sigma_z(k_x^2 + k_y^2). \tag{3.33}$$

The additional term vanishes in the continuum limit for $B \propto 1/a$. Therefore, the Dirac cone at $\boldsymbol{k} = 0$ is retained in the continuum limit.

However, it is also necessary to expand the Hamiltonian around the other Dirac points to examine their behavior in the continuum limit. The expansion of the Hamiltonian yields

$$H_{\mathrm{D}}^{\mathrm{Bloch}} = Aa[\sigma_x(k_y - k_{\mathrm{D},y}) - \sigma_y(k_x - k_{\mathrm{D},x})] + B\sigma_z\left(\text{const.} - \frac{\boldsymbol{k}^2 a^2}{2}\right), \tag{3.34}$$

where $\boldsymbol{k}_{\mathrm{D}} \in \{(\pi/a, 0), (0, \pi/a), (\pi/a, \pi/a)\}$. Thus, the constant term $B \propto 1/a$ diverges in the continuum limit which means the fermion doublers acquire an infinite mass and are gapped out. Therefore, we are only left with the Dirac cone at $\boldsymbol{k} = 0$ in the continuum limit. This is known as the Wilson fermion approach for putting Dirac fermions on a lattice. Note that this works both for massive and massless fermions.

Because our numerical results inherently rely on finite lattices rather than the strict continuum limit, the Wilson term is always present. We hypothesize that this term acts as a physical regularization for the Dirac Hamiltonian, naturally yielding the unique boundary condition at the origin for the critical subspace.

Therefore, in contrast to the standard Wilson fermion approach, we consider a continuum limit where the quadratic term retains physical significance by setting $\frac{Ba^2}{2} \to \frac{\hbar^2}{m}$, where the mass m is some arbitrary parameter. This allows to explicitly introduce a $\boldsymbol{k}^2\sigma_z$ dependence in the analytical continuum description of the surface model and regularize it. Moreover, it still ensures fermion doublers are gapped out in the corresponding lattice picture.

However, we require the linear Dirac term to remain dominant at the relevant energy scale $\hbar v/R$. For characteristic momenta $|\boldsymbol{p}| \sim \hbar/R$ imposed by the boundary condition, the quadratic contribution remains a small perturbation provided that

$$\frac{\hbar}{mvR} \ll 1. \tag{3.35}$$

To quantify this regime, we introduce the characteristic length scale for the quadratic term, $r^* \equiv \hbar/mv$ which simplifies our validity condition to $r^* \ll R$.

Next, we proceed with the lattice description to obtain numerical results. For this, we have to find the real space lattice contribution of the cosine term from the Wilson regularization (3.31). This is done by using the continuum limit which yields $\frac{B}{2}a^2\boldsymbol{k}^2\sigma_z$. Replacing the $k_j^2 \to -\partial_j^2$ allows for using the discretized version of the derivative. Proceeding similar to the single derivative given in (3.24) we obtain

$$\partial_j^2 \to \frac{1}{a^2}\sum_{\boldsymbol{n}} \left(|\boldsymbol{x_n}\rangle\langle\boldsymbol{x_n}+a\boldsymbol{e}_j| + |\boldsymbol{x_n}\rangle\langle\boldsymbol{x_n}-a\boldsymbol{e}_j| - 2|\boldsymbol{x_n}\rangle\langle\boldsymbol{x_n}|\right). \tag{3.36}$$

Finally, we obtain the lattice version of the Hamiltonian (3.1) which reads

$$\begin{aligned} H_{\mathrm{D}}^{\mathrm{lat}} = \sum_{\boldsymbol{n}} \Bigg[&\left(\frac{iA}{2}\sigma_x - \frac{B}{2}\sigma_z\right)|\boldsymbol{x_n}+a\boldsymbol{e}_x\rangle\langle\boldsymbol{x_n}| \\ &+ \left(-\frac{iA}{2}\sigma_y - \frac{B}{2}\sigma_z\right)|\boldsymbol{x_n}+a\boldsymbol{e}_y\rangle\langle\boldsymbol{x_n}| + \mathrm{h.c.}\Bigg] \\ &+ \sum_{\boldsymbol{n}} 2B\sigma_z|\boldsymbol{x_n}\rangle\langle\boldsymbol{x_n}|. \end{aligned} \tag{3.37}$$

Moreover, the magnetic vector potential has to be accounted for in the lattice model which is achieved by using the Peierls substitution

$$|\boldsymbol{x_n}+a\boldsymbol{e}_j\rangle\langle\boldsymbol{x_n}| \to \exp\left(i\frac{q}{\hbar}\int_{\boldsymbol{x_n}}^{\boldsymbol{x_n}+a\boldsymbol{e}_j}\boldsymbol{A}\cdot d\boldsymbol{\ell}\right)|\boldsymbol{x_n}+a\boldsymbol{e}_j\rangle\langle\boldsymbol{x_n}|, \tag{3.38}$$

where the prefactor is called Peierls phase. We approximate the integral by

$$\int_{\boldsymbol{x_n}}^{\boldsymbol{x_n}+a\boldsymbol{e}_j}\boldsymbol{A}\cdot d\boldsymbol{\ell} \approx \boldsymbol{A}\left(\boldsymbol{x_n}+\frac{a}{2}\boldsymbol{e}_j\right)\cdot a\boldsymbol{e}_j. \tag{3.39}$$

The Peierls phase that a particle picks up by going around a single plaquette on the lattice is equal to the magnetic flux that penetrates the plaquette. A

convenient gauge to implement the vector potential given in (3.3) is

$$\boldsymbol{A}_{\text{lat}} = -\Phi\delta\left(y - \frac{a}{2}\right)\Theta(x), \tag{3.40}$$

because it allows for a constant phase applied to a single line of links.

The disc shape defined by the boundary condition (3.7) is implemented using a smoothed profile. Instead of a sharp step function, we use

$$\Delta(r) = \frac{\Delta}{2}\left[1 + \tanh\left(\frac{r - R}{w}\right)\right], \tag{3.41}$$

where Δ is the boundary potential, R the radius of the system, and w controls the width of the smoothed boundary region. The step function is recovered in the limit $w \to 0$. The boundary term only contributes to the on-site potential in the lattice Hamiltonian (3.37), as it is diagonal in the position basis. The smoothing over a width w around the boundary helps to preserve rotational symmetry which would otherwise be broken due to the underlying square lattice used in the simulations. The specific choice of the smoothened step function is arbitrary.

Although the simulations are performed on a square lattice, we explicitly shape the lattice into a disc geometry by including only the lattice sites within the radial distance $R + s$ from the center. The extension of the lattice disc by an additional radial length s, in units of lattice spacing a, is added to ensure that the wavefunctions can decay properly into the region $r > R$. This extension avoids artificial cutoffs of the wavefunctions at the boundary, allowing for exponential decay as expected in the continuum model if Δ is kept finite. Moreover, it is important that the center of the disc is a plaquette and not a site, such that the origin can be penetrated by the magnetic flux.

To compare our lattice results with the continuum model, we must approach the continuum limit $a/R = 1/N \to 0$. In all simulations we fix the lattice spacing to $a = 1$ and use the lattice radius $R_{\text{lat}} \equiv N$ as the parameter controlling the continuum limit. In this unit system we approach the continuum model using $A = 1$ and $B = R_{\text{lat}}/f$ with some constant f which parametrizes the mass parameter m. Then we have $\hbar v = 1$ and $\hbar^2/m = R_{\text{lat}}/2f$. Due to the boundary condition the energies are scaling as $1/R_{\text{lat}}$, so we need to multiply the numerical energies by its inverse to get the scale invariant energies.

In the continuum limit, the lattice regularization length $r^*_{\text{lat}} = Ba^2/2Aa$ diverges. However, the physical validity of the model depends on the dimensionless ratio r^*/R. By maintaining the ratio $r^*_{\text{lat}}/R_{\text{lat}} = 1/2f$ as a constant, we ensure the regularization remains well-behaved. The condition $r^*/R \ll 1$ is satisfied by choosing $f \gg 1$.

Moreover, $2w = \Delta = 1$ and $s = 4$ are used, which is a natural choice for units of $a = 1$. This means the mass profile is smeared over only two sites, and the states decay outside the system with an inverse decay length Δ of one site. With fixed lattice spacing we must satisfy $\Delta \gg 1/R_{\text{lat}}$ in order

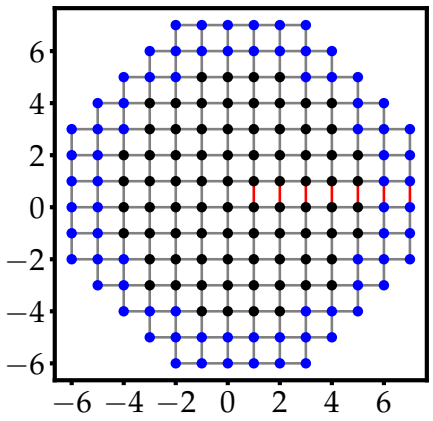

FIGURE 3.3: Lattice for $a = 1, N = 5, s = 2$. Black sites are within $r \leq R$, blue sites are within $R < r \leq R + s$ where the hard-wall boundary condition is employed. The links colored red have a Peierls phase of $e^{-i2\pi g}$, the black ones have zero Peierls phase. A plaquette is defined by the smallest rectangle possible, constructed with four sites and links.

to apply the continuum boundary condition. This condition is satisfied by taking N sufficiently large which is in any case required to obtain a good approximation of the continuum limit. In the following, we only vary the parameters N and f, whereas all other parameters are as stated above if not explicitly annotated differently.

An example of the resulting lattice model is shown in Fig. 3.3, using a small number of sites to illustrate the main features.

The resulting spectrum is shown in Fig. 3.4. Unlike in the analytical results in Fig. 3.2, we do not distinguish the angular momentum sectors by color. We focus only on the low-energy part of the spectrum, as the accuracy of the numerical results decreases at higher energies, because more lattice sites are required. This is due to discretization errors, where shorter wavelengths become poorly resolved on a fixed lattice spacing.

Despite these limitations, we find perfect agreement between the numerical and analytical results in the low-energy regime for the angular momenta $n \neq n^*$. In addition, the numerical results reveal a distinct non-linear dependence on g of the energy, corresponding to the critical state with $n = n^* = -1$ for $g \in (0,1)$ which is not found in the analytical results yet. This curve matches the prediction made in section 3.2, qualitatively showing the expected behavior of a decreasing energy for $\gamma < \frac{1}{2}$, followed by an increase as $1/2 < \gamma < 1$.

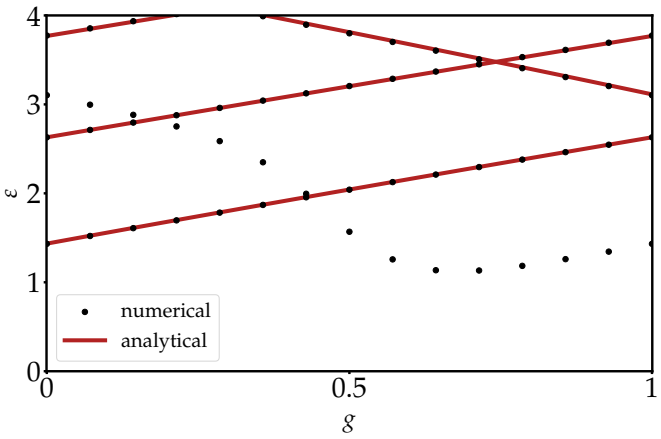

FIGURE 3.4: Analytical and numerical dimensionless energies as function of the magnetic flux ratio $g \in [0,1]$. Numerical parameters: $N = 100$ and $f = 100$.

3.4 Analytical treatment of the critical subspace

In this section, we consider the regularized continuum model for the surface states analytically. As stated in the prior section, we add the squared momentum term (3.33) to the linear model of the surface Hamiltonian given by (3.1). Moreover, we keep in mind that we work in the regime $r^*/R \ll 1$.

Furthermore, we expect that the quadratic momentum term has a negligible effect on the non-critical angular momentum sectors, where the linear model already yields the correct energies as can be seen in the numerical results in Fig. 3.4. It is expected that the additional term regularizes the critical angular momentum sector, introducing the necessary boundary condition at $r = 0$. Thus, throughout this section we fix $n = n^*$ and $\gamma \in (0,1)$ unless stated otherwise.

Adding the quadratic momentum term to our original linear Hamiltonian yields the modified Hamiltonian

$$H_{\mathrm{D}}^{\mathrm{reg}} = v\left[\boldsymbol{\sigma} \times (\boldsymbol{p} - q\boldsymbol{A})\right] \cdot \boldsymbol{e}_z + \frac{1}{m}(\boldsymbol{p} - q\boldsymbol{A})^2 \sigma_z \tag{3.42}$$

for the surface states. The superscript indicates that this model is a regularized version of the original linear model, see Eq. (3.1). This is exactly the massless version of the Hamiltonian encountered in Chpt. III of Ref. [9], where massless means that there is no constant term $M\sigma_z$. Although, the ansatz to solve for the eigenstates is technically similar, the absence of mass alters solution, necessitating a separate derivation.

The regularized Hamiltonian maintains the symmetry with respect to the total angular momentum, namely $[H_{\mathrm{D}}^{\mathrm{reg}}, J] = 0$ and we can make the ansatz (3.6) for the eigenstates. From this we can derive the radial spinor equations

for the eigenenergy E which are

$$\left(\frac{\hbar^2}{m}\left[-\partial_r^2-\frac{1}{r}\partial_r+\frac{(\gamma-1)^2}{r^2}\right]\right)\chi_{1,n}(r)+\hbar v\left(\partial_r+\frac{\gamma}{r}\right)\chi_{2,n}(r)=E\,\chi_{1,n}(r) \tag{3.43a}$$

$$\left(-\frac{\hbar^2}{m}\left[-\partial_r^2-\frac{1}{r}\partial_r+\frac{\gamma^2}{r^2}\right]\right)\chi_{2,n}(r)+\hbar v\left(-\partial_r+\frac{\gamma-1}{r}\right)\chi_{1,n}(r)=E\,\chi_{2,n}(r). \tag{3.43b}$$

We denote the operator that acts on the LHS of the equations as the radial Hamiltonian $h_{\mathrm{D}}^{\mathrm{reg}}(r)$.

For the radial spinor we make the ansatz

$$\boldsymbol{\chi}(r)=\begin{pmatrix} aK_{1-\gamma}(\kappa r)\\ bK_{\gamma}(\kappa r)\end{pmatrix} \tag{3.44}$$

and

$$\boldsymbol{\xi}(r)=\begin{pmatrix} cI_{1-\gamma}(\eta r)\\ dI_{\gamma}(\eta r)\end{pmatrix}, \tag{3.45}$$

which are suggested by the modified Bessel differential equation appearing in (3.43a), (3.43b). Here $I_\nu(x)$ and $K_\nu(x)$ are the modified Bessel function of order ν of the first and second kind, respectively, see App. A. This is the same ansatz as presented in Ref. [9]. Here a, b, c, d, κ, η are to be determined by the radial equations. Plugging in the Ansatz (3.44) and (3.45) into the radial equations (3.43a), (3.43b) reduces the problem to an algebraic eigenvalue problem.

For $\boldsymbol{\chi}(r)$, we get

$$\begin{pmatrix} -r^*\kappa^2 & -\kappa\\ \kappa & r^*\kappa^2\end{pmatrix}\begin{pmatrix} a\\ b\end{pmatrix}=k\begin{pmatrix} a\\ b\end{pmatrix} \tag{3.46}$$

and analogously for $\boldsymbol{\xi}(r)$

$$\begin{pmatrix} -r^*\eta^2 & \eta\\ -\eta & r^*\eta^2\end{pmatrix}\begin{pmatrix} c\\ d\end{pmatrix}=k\begin{pmatrix} c\\ d\end{pmatrix}, \tag{3.47}$$

which are both obtained using recurrence relations and the differential equation of the modified Bessel functions given in appendix A.

The energy appearing in $k=E/\hbar v$, is the only constant left undetermined so we can solve the eigenvalue equations for κ, a, b and η, c, d, respectively, as a function of k. For this, we solve the determinant equation

$$\det\left(M_\kappa-k\right)=0, \tag{3.48}$$

where M_κ is the matrix on the LHS of 3.46. This yields

$$\kappa_\pm=\frac{1}{r^*}\sqrt{\frac{1\pm\sqrt{1+(2kr^*)^2}}{2}}, \tag{3.49}$$

where only the positive roots are kept. The same solution applies to the determinant of Eq. (3.47) which gives $\eta_\pm = \kappa_\pm$. This shows how the regularized Hamiltonian introduces the length scale $r^* = \hbar/mv$, we have already seen in the numerical solution in Sec. 3.3.

Now we can determine the ratios b/a and d/c, leaving each solution only with an overall normalization constant. With Eq. (3.46), we obtain

$$\left(\frac{b}{a}\right)_\pm = \frac{\kappa_\pm}{k - r^*\kappa_\pm^2} \tag{3.50}$$

and Eq. (3.47) yields

$$\left(\frac{d}{c}\right)_\pm = \frac{r^*\kappa_\pm^2 + k}{\kappa_\pm}. \tag{3.51}$$

Now we have four solutions, as expected from our coupled second order differential equation, and the full solution is denoted as

$$\chi^{\text{reg}}(r) = \sum_{i=\pm} \left[\chi_i(r) + \xi_i(r)\right]. \tag{3.52}$$

As of now, no approximations have been applied and the solution is still exact. Moreover, the result is similar to that of Ref. [9] with the mass set to zero, but we have kept the $I_\nu(x)$ solutions.

In our model, we introduce the hard-wall boundary condition Eq. (3.11) at radius R, from which we can determine the energies and introducing the scaling $k = \varepsilon/R$. The dimensionless energy ε is of $\mathcal{O}(1)$ which can also be seen by the numerical results in Fig. 3.4. Combining this result with $r^* \ll R$ yields

$$\eta_+ = \kappa_+ \approx 1/r^* \tag{3.53}$$

and

$$\eta_- = \kappa_- \approx -ik. \tag{3.54}$$

Subsequently, the ratios are approximately given by

$$\left(\frac{b}{a}\right)_+ \approx -1, \qquad \left(\frac{b}{a}\right)_- \approx -i \tag{3.55}$$

and

$$\left(\frac{d}{c}\right)_+ \approx 1, \qquad \left(\frac{d}{c}\right)_- \approx i. \tag{3.56}$$

First, we have to discard the η_+ solution because $I_\nu(r/r^*)$ diverges in the limit of $r^* \to 0$ and is not normalizable. In contrast, the η_- solution can be kept because the imaginary argument makes the function well-behaved, see App. A. Thus, we are left with the solution

$$\chi^{\mathrm{reg}}(r) = a_+ \begin{pmatrix} K_{1-\gamma}(r/r^*) \\ -K_\gamma(r/r^*) \end{pmatrix} + a_- \begin{pmatrix} K_{1-\gamma}(-ikr) \\ -iK_\gamma(-ikr) \end{pmatrix} + c_- \begin{pmatrix} I_{-1+\gamma}(-ikr) \\ iI_\gamma(-ikr) \end{pmatrix} \tag{3.57}$$

with $a_\pm, c_-$ being constants. Note that we used $K_\nu(x) = K_{-\nu}(x)$.

After employing properties of the Bessel functions, the final solution is obtained as

$$\chi^{\mathrm{reg}}(r) = C \begin{pmatrix} K_{1-\gamma}(r/r^*) \\ -K_\gamma(r/r^*) \end{pmatrix} + \begin{pmatrix} B\, J_{1-\gamma}(kr) + A\, J_{-1+\gamma}(kr) \\ -[B\, J_{-\gamma}(kr) - A J_\gamma(kr)] \end{pmatrix} \tag{3.58}$$

with redefined constants A, B, C.

This is the exact same solution as for the linear Hamiltonian from Eq. (3.1), given in Eq. (3.21) but with an additional solution given by the modified Bessel function of the second kind $K_\nu(x)$. Thus, the linear solutions remain valid for the regularized model in the regime $r^* \ll R$. This is stressed by defining

$$\chi^q(r) \equiv C \begin{pmatrix} K_{1-\gamma}(r/r^*) \\ -K_\gamma(r/r^*) \end{pmatrix} \tag{3.59}$$

as the solution arising from the quadratic term and

$$\chi^l(r) \equiv \begin{pmatrix} B\, J_{1-\gamma}(kr) + A\, J_{-1+\gamma}(kr) \\ -[B\, J_{-\gamma}(kr) - A J_\gamma(kr)] \end{pmatrix} \tag{3.60}$$

as the two solutions of the linear model. Consequently, we can write

$$\chi^{\mathrm{reg}}(r) = \chi^q(r) + \chi^l(r). \tag{3.61}$$

To determine the energy E from the hard-wall boundary condition at $r = R$, we have to determine the constants up to a normalization factor first. In order to do this an additional boundary condition at the origin is needed. The asymptotic behavior of $K_\nu(x)$, given in App. A, yields

$$\lim_{r\to R} \chi_i^q(r) \propto \sqrt{\frac{\pi r^*}{2R}} e^{-R/r^*} \approx 0, \tag{3.62}$$

which implies that the quadratic solution only governs the behavior at the origin, but has no effects far away at $r \gg r^*$.

Finally, it is worth noting that we can extend this solution method for the regularized model to arbitrary angular momenta $n \neq n^*$. For these, we also obtain the same solution as for the linear model and an additional solution arising from the quadratic momentum term. However, due to the normalization constraint we are only left with one of the solutions of the linear model. Thus, we get the same energies both for the linear and the regularized model which matches with the expectation formulated in the beginning of this section. Therefore, it is justified to only consider the regularization in the critical angular momentum subspace.

The regularized Hamiltonian introduces the boundary condition at the origin which is needed to determine the energies. To derive the boundary condition, an arbitrary radial spinor $\mathbf{\Psi}(r)$ is considered. For the state to be physical, a finite energy expectation value

$$\int_0^\infty dr r \mathbf{\Psi}(r)^\dagger h_{\mathrm{D}}^{\mathrm{reg}}(r) \mathbf{\Psi}(r) < \infty \tag{3.63}$$

is required. It can be easily checked that this requires the behavior

$$\lim_{r\to 0} \chi_i(r) = r^\nu, \quad \nu > 0 \tag{3.64}$$

for the radial spinor components. Now, the separate solutions in $\chi^{\mathrm{reg}}(r)$ do not fulfill this condition, but if we discard all of them we have no solution at all in the critical angular momentum subspace. This cannot be the case as this would imply there is no state at all in the critical subspace and hence no corresponding energy in the spectral flow.

The solution to this problem is that we can impose the regularity in terms of a boundary condition on the full state

$$\chi^{\mathrm{reg}}(0) = 0 \tag{3.65}$$

which spans the critical subspace, such that the condition (3.64) is fulfilled. Here, regularity means that the wavefunction does not diverge. The possibility to impose this condition arises from the fact that the additional solution $\chi^q(r)$ carries the same divergence as the divergent components of the linear solution $\chi^l(r)$. Thus, the constants can be determined to cancel the divergent behavior. The quadratic solution is therefore essential for the behavior at the origin because there are no components that diverge at the origin $r = 0$ anymore.

This boundary condition is the same as found in Ref. [9] which the authors derive using an AB-field smeared out into a finite radius that is sent to zero in the end of the calculation. Moreover, it also seems to be a sensible boundary condition as it aligns with the regularity of the radial spinors in the subspaces $n \neq n^*$. Thus, we have found a regularized version of the original linear model. The boundary condition is also understood as a specific SAE of the Hamiltonian (3.42) as shown in Ref. [17]. However, we have found the boundary condition from the physical assumption, given by Eq. (3.63).

Finally, by imposing the boundary conditions at $r = 0$ and $r = R$, we determine the energies. Applying the boundary condition $\chi^{\mathrm{reg}}(0) = 0$ reduces to the equation

$$\lim_{r\to 0} \frac{\chi_1^l(r)}{\chi_2^l(r)} = \lim_{r\to 0} \frac{\chi_1^q(r)}{\chi_2^q(r)}. \tag{3.66}$$

Consequently, we need the small argument limiting behavior of the Bessel and modified Bessel functions, given in Eqs. (A.7) and(A.16), respectively. This yields

$$f(\gamma, k) \equiv \frac{A}{B} = (kr^*)^{1-2\gamma}, \tag{3.67}$$

where the ratio defines the function $f(\gamma, k)$. Moreover, applying the boundary condition yields the following result

$$C = -B\frac{2}{\Gamma(1-\gamma)\Gamma(\gamma)}(kr^*)^{-\gamma} \equiv -Bg(\gamma, k) \tag{3.68}$$

such that only an overall normalization constant is left in $\chi^{\text{reg}}(r)$. The final result for the regularized radial spinor is

$$\chi^{\text{reg}}(r) = B\left[-g(\gamma,k)\begin{pmatrix} K_{1-\gamma}(r/r^*) \\ -K_\gamma(r/r^*)\end{pmatrix} + \begin{pmatrix} J_{1-\gamma}(kr) + f(\gamma,k)J_{-1+\gamma}(kr) \\ -J_{-\gamma}(kr) + f(\gamma,k)J_\gamma(kr)\end{pmatrix}\right]. \tag{3.69}$$

Since the quadratic solution decays exponentially according to (3.62), the boundary condition at $r = R$ is governed exclusively by the linear solution $\chi^l(r)$, whereas the influence of the quadratic solution enters via the ratio A/B containing the scale ration r^*/R. Then, applying the boundary condition (3.10), we obtain the equation

$$J_{1-\gamma}(kR) + f(\gamma,k)J_{-1+\gamma}(kR) = -J_{-\gamma}(kR) + f(\gamma,k)J_\gamma(kR) \tag{3.70}$$

which determines the energy by solving for the dimensionless energy $\varepsilon = kR$. The intersections $\varepsilon_{n^*,z}$ have the angular quantum number $n = n^*$, depending on the integer part l of the magnetic flux due to $n^* = -l - 1$, and the radial quantum number $z \in \mathbb{N}$ that labels the solutions of this equation.

The regularization in the $r \lesssim R$ regime weights the solution in $\chi^l(r)$ with weaker power-law divergence at the origin stronger, compared to the other solution. For instance, for $\gamma < \frac{1}{2}$, the function $J_{-\gamma}$ diverges more weakly than $J_{-1+\gamma}$, whereas for $\gamma > \frac{1}{2}$ the situation is reversed. For the special case $\gamma = \frac{1}{2}$, we have the unique case of both linear solutions exhibiting the same degree of singularity at the origin. As a result, both solutions contribute equally. All of this is reflected in the behavior of $f(\gamma, k)$ which is the relative weighting factor between the two distinct solutions (3.69). In the regime $r^* \ll R$, the quadratic term is still present, providing the regularization on a scale r^* that is negligible compared to the system size R, but still finite.

In the limit $r^* \to 0$, the regularizing spinor χ^q coming from the quadratic term vanishes by virtue of (A.15), but the ratio $f(\gamma, k)$ remains well defined and becomes an exact selector of the two linear solutions

$$f(\gamma,k) \to \begin{cases} 0, & \gamma < \frac{1}{2} \\ 1, & \gamma = \frac{1}{2} \\ \infty, & \gamma > \frac{1}{2} \end{cases}, \tag{3.71}$$

independently of k. In this case the less singular solution is chosen uniquely and the other is discarded. For $r^* \ll R$ the same mechanism persists only as a strong weighting, i.e., $f(\gamma, k)$ is a smeared out step function and the energy equation (3.5) reflects this smoothened selection. Figure 3.5 illustrates how $f(\gamma, k)$ sharpens toward the $r^* = 0$ behavior as r^*/R decreases. Moreover, we can see the invariance of the energy at $\gamma = 1/2$ which remains the same

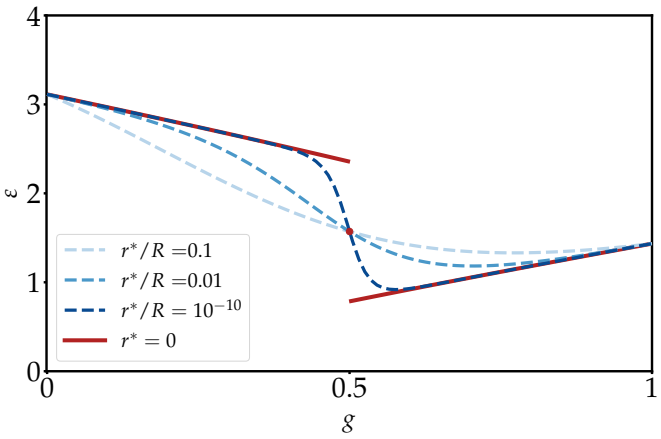

FIGURE 3.5: Analytical result for dimensionless energies of the critical subspace state determined with equation (3.70) as function of the magnetic flux ratio $g \in [0,1]$. Comparison of the limit case $r^* = 0$ and finite but small ratios r^*/R.

for all values of r^*/R because $f(\frac{1}{2}, k) = 1$.

Our result can be directly compared to the self-adjoint extension approach in Ref. [15], specifically their Eq. (11) which gives the ratio of the integration constants of the two solutions in the critical subspace. Since the mass and SAE scale therein were chosen to coincide, the mass in their expression must be replaced by our regularization scale r^* in the massless limit that we want to study. By evaluating both models at half a flux quantum, where all prefactors and the scale drop out, we find that our result (3.67) corresponds to the SAE parameter $\theta = 0$.[1] Thus, rather than treating θ as a free mathematical parameter, our physical regularization procedure determines θ while keeping r^* finite and relating it to an actual regularization term in the Hamiltonian, namely the mass m.

Lastly, we want to mention here that Ref. [9] suggests that the r^* is given by the atomic lattice spacing of the TI. In turn, this fixes $r^*/R \ll 1$ but finite for system sizes much larger than the atomic lattice spacing.

3.5 Comparison of numerics and analytics

In this section, we compare the numerical with the analytical results. Both results are shown in Fig. 3.6, where the focus is placed on the energy of the critical state $n = n^* = -1$ colored blue which is its lowest positive energy and hence radial quantum number $z = 1$. This is motivated by the fact that the lattice model already reproduces the energies of the other states, colored red, with sufficient accuracy to confirm our analytical results for the angular momentum subspaces $n \neq n^*$.

[1] Any remaining factor differences arise because in Ref. [15] $\sigma \cdot \boldsymbol{p}$ is utilized rather than $(\sigma \times \boldsymbol{p}) \cdot \boldsymbol{e}_z$ which are simply related by a unitary transformation $V = e^{-i\pi/2\sigma_z}$.

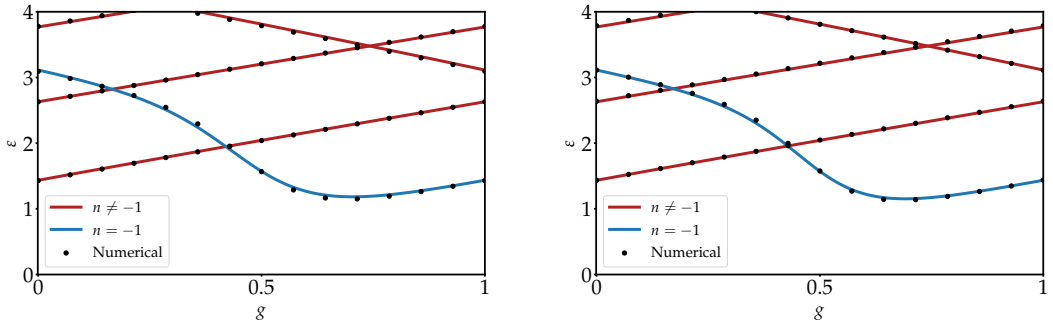

(A) $R_{\text{lat}} = 50$ and $f = 50$ (B) $R_{\text{lat}} = 200$, $f = 100$

FIGURE 3.6: Numerical and analytical results for dimensionless energies $\varepsilon_{n,z}$ as a function of the magnetic flux $g \in [0, 1]$ for the parameters specified in panel captions (A) and (B). The numerical energies are represented by black dots, while the analytical energies are shown as solid lines. The critical state has $n = n^* = -1$ and the radial quantum number $z = 1$ is considered here. Its energy is calculated using Eq. (3.70) with $r^*/R = 1/(2f)$ and $R = R_{\text{lat}}$.

It can be seen that the numerical energies for the critical state do not perfectly coincide with the respective analytical curves, but follow them with good qualitative agreement. As this is the case, it confirms that the numerical results exhibit the trend of a sharpening step function with increasing f in agreement with the analytical result. This implies that in the limit of $r^*/R \to 0$, we obtain a sharp step as expected.

The deviations can be traced back to the fact that the simulations cannot fully reach the continuum limit, since this would require $R_{\text{lat}} \to \infty$, while here R_{lat} is only moderately large. Still, we can see that for increasing R_{lat} the deviations become less pronounced as predicted, comparing Fig. 3.6a to Fig. 3.6b. This implies that the results are expected to match exactly in the continuum limit.

Moreover, it can be observed that the deviations are most pronounced around $\gamma = 1/2$, but the least strong for $\gamma \to 0, 1$. This follows from the behavior of $f(\gamma, k) = (kr^*)^{1-2\gamma}$ which rapidly approaches its limiting values $r^*/R \ll 1$ and $R/r^* \gg 1$ for $\gamma \to 0$ and $\gamma \to 1$, respectively. Additionally, at $\gamma = 1/2$ the expression is independent of r^*/R. This suggests that due to the finiteness of R_{lat} which controls the continuum limit, the identification of $r^*/R = r^*_{\text{lat}}/R_{\text{lat}}$ is not perfectly exact but only approximate. This leads to the most pronounced deviations from the analytical results for values around $\gamma = 1/2$. In the continuum limit $R_{\text{lat}} \to \infty$, this difference vanishes. Moreover, the lattice only approximately models the circular geometry which also leads to deviations between numerical and analytical results. Keeping the approximate nature of the comparison in mind, we can conclude that the numerical results confirm the analytical model.

Lastly, we verify that the squared momentum term indeed regularizes the divergence of the critical state at the origin. To this end, we use $B = R_{\text{lat}}/f$

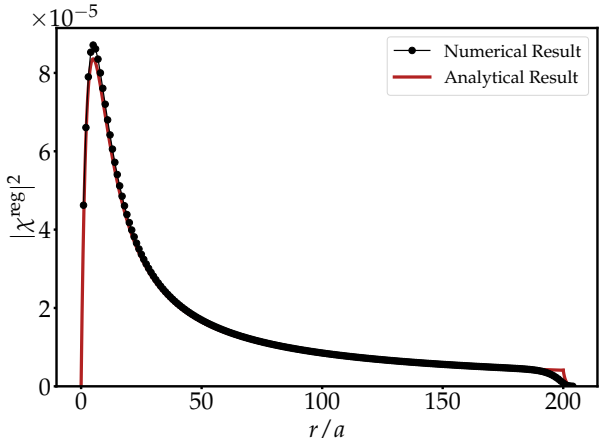

FIGURE 3.7: Comparison of analytical and lattice result for the radial spinor amplitude $|\chi^{\text{reg}}(r)|^2$ for $g = 1/2$. Numerical parameters: $R_{\text{lat}} = 200, f = 25$.

to tune the regularization scale $r^*_{\text{lat}} = B/2 = R_{\text{lat}}/2f$. Choosing parameters so that $r^*_{\text{lat}} < 1$ corresponds to a regularization scale smaller than the lattice spacing $a = 1$ which is not resolvable. Therefore, we must choose R_{lat} and f accordingly to observe the effects of regularization, while maintainig that the ratio $r^*_{\text{lat}}/R_{\text{lat}} = 1/2f$ is small.

Figure 3.7 shows the resulting radial density for $r^*_{\text{lat}} = 4$, where excellent agreement between the numerical and analytical result is observed. The remaining amplitude mismatch near the origin stems from the fact that the lattice cannot resolve the origin $r = 0$, as also visible in Fig. 3.3. Although the ratio $1/2f$ is not very small for this choice of parameters, it is still sufficient to keep the validity of the approximations and it shows the regularization of the state. Again, the actual approaching the continuum limit $R_{\text{lat}} \to \infty$ resolves this problem, because it allows for large values of f while maintaining $r^*_{\text{lat}} > 1$.

Chapter 4

Dirac Sphere with a magnetic monopole

The goal of this chapter is to analytically obtain the surface states and spectral flow of the Dirac sphere with a magnetic monopole-string configuration placed at its center. This is the model studied numerically in Ch. 4.3 of Ref. [5]. We begin by introducing the Hamiltonian on the Dirac sphere which includes curvature terms. Moreover, we mathematically introduce the concept of the magnetic monopole and the Dirac string for unquantized magnetic flux. With the Hamiltonian and vector potential at hand, we aim to solve the eigenvalue equation for the Dirac sphere to obtain the surface states and spectral flow for arbitrary magnetic flux values.

4.1 Dirac sphere Hamiltonian and magnetic monopole field

The model of the Dirac sphere is presented first in the absence of a magnetic monopole. Mathematically, this requires us to derive the Dirac operator on the Riemann sphere which is achieved using the framework of differential geometry, as demonstrated in Ref. [18]. However, the surface Hamiltonian can also be obtained through the derivation of surface states of the 3D TI's bulk Hamiltonian, similar to the derivation seen in Sec. 2.3. This derivation is shown in Ref. [19], specifically for the spherical geometry.

It is important to note that in Ref. [19] a surface Hamiltonian is obtained which has the same structure as the surface Hamiltonian in Sec. 2.3. It differs by a unitary transformation to the Hamiltonian in Refs. [5, 18]. In this thesis we are going to use the convention of the latter.

Thus, following Refs. [5, 18], the Hamiltonian for the Dirac sphere reads

$$H_{\mathrm{DS}} = -\frac{i\hbar v}{R}\left[\sigma_x \partial_\theta + \frac{\sigma_y}{\sin(\theta)}\left(\partial_\phi - i\frac{\cos(\theta)}{2}\sigma_z\right)\right] \tag{4.1}$$

with the radius R and velocity v. The Pauli matrices σ_i occur due to the particle being spin-$\frac{1}{2}$. In App. B of Ref. [5] it is explained that this Hamiltonian acts in the so called local spinor basis. In this basis the $\{\theta, \phi, r\}$-component of the Pauli vector σ are the operators $\{\sigma_x, \sigma_y, \sigma_z\}$, respectively. Here, spherical coordinates are denoted by r, ϕ, θ.

Moreover, the total angular momentum operator components in the local spinor basis are given by

$$J_z^{(l)} = -i\hbar\partial_\phi \tag{4.2a}$$

$$J_\pm^{(l)} = \pm\hbar e^{\pm i\phi}\left(\partial_\theta \pm i\cot(\theta)\partial_\phi \pm \frac{\sigma_z}{2\sin(\theta)}\right). \tag{4.2b}$$

For a detailed derivation, the reader is referred to Ref. [5].

Finally, the form of H_{DS} suggests to define the momentum operator on the sphere for a spin-$\frac{1}{2}$ particle as

$$\boldsymbol{P} \equiv -\frac{i\hbar}{R}\left[\boldsymbol{e}_\theta\frac{\partial}{\partial\theta} + \boldsymbol{e}_\phi\frac{1}{\sin(\theta)}\left(\frac{\partial}{\partial\phi} - \frac{i}{2}\sigma_z\cos(\theta)\right)\right]. \tag{4.3}$$

Next, we want to describe how to include the magnetic monopole into the Dirac sphere Hamiltonian. The field of a magnetic monopole in three dimensions is described by

$$\boldsymbol{B}_m = \frac{q_m\Phi_0}{4\pi r}\boldsymbol{e}_r, \tag{4.4}$$

similar to an electric point charge. Here, $\Phi_0 = h/e$ is the magnetic flux quantum and

$$\Phi = \int_{S^2} d\boldsymbol{S}\cdot\boldsymbol{B}_m = q_m\Phi_0 \tag{4.5}$$

is the magnetic flux through the sphere's surface.

While a magnetic monopole field can be defined mathematically, the concept initially appears to contradict classical electromagnetism, as it violates Gauss' law for magnetism $\nabla\cdot\boldsymbol{B} = 0$. However, this problem can be resolved by trying to describe the magnetic field using a vector potential $\boldsymbol{B} = \nabla\times\boldsymbol{A}$. In addition to that, the vector potential $\boldsymbol{A}$ is needed to incorporate the magnetic field via minimal coupling into the Hamiltonian.

Following Ref. [20], the vector potential is found to be

$$\boldsymbol{A} = -\frac{q_m\Phi_0}{4\pi r}\frac{1+\cos(\theta)}{\sin(\theta)}\boldsymbol{e}_\phi. \tag{4.6}$$

Applying the rotation to this vector field, the magnetic field

$$\boldsymbol{B} = \nabla\times\boldsymbol{A} = \frac{q_m\Phi_0}{4\pi r}\boldsymbol{e}_r - q_m\Phi_0\Theta(z)\delta^{(2)}(\boldsymbol{\rho})\boldsymbol{e}_z \tag{4.7}$$

is obtained which consists of the monopole field $\boldsymbol{B}_m$ and the Dirac string contribution

$$\boldsymbol{B}_s = -q_m\Phi_0\Theta(z)\delta^{(2)}(\boldsymbol{\rho})\boldsymbol{e}_z. \tag{4.8}$$

The Heaviside step-function is denoted by $\Theta(z)$ and we use the two-dimensional Dirac delta function in the x,y-plane $\delta^{(2)}(\boldsymbol{\rho}$ with $\boldsymbol{\rho} = x\boldsymbol{e}_x + y\boldsymbol{e}_y$. The overall magnetic field configuration together with the Dirac sphere is depicted in Fig. 4.1.

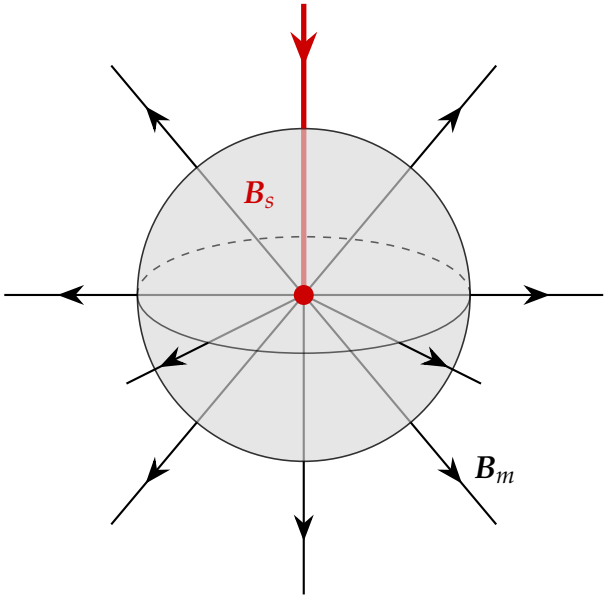

FIGURE 4.1: Field lines of the magnetic monopole $\boldsymbol{B}_m$ and the Dirac string $\boldsymbol{B}_s$ for $q_m > 0$ colored in black and red, respectively, indicating the opposite magnetic flux.

The Dirac string emerges from the singularity of the vector potential along the semi-infinite line for $\theta = 0$, piercing the North Pole of the sphere. We can see from the form of $\boldsymbol{B}_s$ that it describes an infinitesimally thin solenoid carrying a magnetic flux

$$\int_{\mathcal{C}} d\boldsymbol{S} \cdot B_s = -q_m \Phi_0 \tag{4.9}$$

through any surface $\mathcal{C}$ on the sphere that contains the North Pole. This directly implies that the magnetic flux of the total magnetic field is

$$\int_{S^2} d\boldsymbol{S} \cdot \boldsymbol{B} = 0, \tag{4.10}$$

namely Gauss' law is not violated.

This distinction is precisely where our description differs from that of a physical magnetic monopole for which the net flux through a closed surface must be non-zero. In the presence of a Dirac string, the total flux remains zero because the string carries the inverse flux of the monopole back into the closed surface. Consequently, to model a physical monopole, the Dirac string must be rendered unobservable so that it exerts no physical influence on particles. There are several derivations which show how to achieve this, and all of them lead to the Dirac quantization condition.

The simplest derivation of the Dirac quantization condition is using Aharonov-Bohm effect, introduced in Sec. 2.4. If a particle is moved slowly counterclockwise around the Dirac string in a loop the wavefunction acquires a phase due to the magnetic field which is $e^{+i2\pi q_m}$. Thus, if we demand the

Dirac string to have no effect so that it is unobservable, we immediately conclude that q_m has to take integer values.

Contrary to the Dirac quantization, we are interested in varying the magnetic flux continuously, so that q_m is arbitrary. In turn, this requires us to consider the Dirac string as a physical object. This perspective allows for an alternative interpretation of the magnetic field configuration given in Eq. (4.7). In this framework, the monopole field effectively emerges from the semi-infinite solenoid's end, providing a physical mechanism to simulate the effects of a magnetic monopole. In the remainder of the thesis the monopole-string configuration is simply referred to as a magnetic monopole.

Finally, to incorporate the magnetic field into the Hamiltonian H_{DS}, minimal coupling $\boldsymbol{P} \to \boldsymbol{P} + e\boldsymbol{A}$ is used. This yields the Hamiltonian

$$H_{\mathrm{DS}}(q_m) = -\frac{i\hbar v}{R}\left\{\sigma_x\partial_\theta + \frac{\sigma_y}{\sin(\theta)}\left[\partial_\phi - i\frac{q_m}{2} - i\frac{\cos(\theta)}{2}\left(\sigma_z + q_m\right)\right]\right\}, \quad (4.11)$$

which implies the magnetic monopole is introduced by the transformation

$$\partial_\phi \to \partial_\phi - i\frac{q_m}{2}, \quad \sigma_z \to \sigma_z + q_m. \quad (4.12)$$

This Hamiltonian possesses a chiral symmetry $\{H_{\mathrm{DS}}, \sigma_z\} = 0$, implying that the spectrum is symmetric around $E = 0$. Moreover, the Hamiltonian satisfies

$$\mathcal{U}H_{\mathrm{DS}}(q_m)\mathcal{U}^{-1} = -H_{\mathrm{DS}}(-q_m) \quad (4.13)$$

for $\mathcal{U} = \sigma_x K$ with the complex conjugation operator K. Applying $\mathcal{U}$ to the eigenvalue Eq. (4.15), we can determine the effect on the energy spectrum as

$$H_{\mathrm{DS}}(-q_m)\boldsymbol{\Psi}_{E'} = -E\boldsymbol{\Psi}_{E'}, \quad (4.14)$$

where $\boldsymbol{\Psi}_{E'} = \mathcal{U}\boldsymbol{\Psi}_E = \sigma_x\boldsymbol{\Psi}_E^*$, using the fact that the energy E is real. The result shows that transforming $q_m \to -q_m$ inverts the energy spectrum to $E \to -E$, rendering it point-symmetric.

4.2 Solution to the eigenvalue problem

We want to solve the eigenvalue problem

$$H_{\mathrm{DS}}(q_m)\boldsymbol{\Psi}_E(\theta,\phi) = E\boldsymbol{\Psi}_E(\theta,\phi) \quad (4.15)$$

for the energy $E = E(q_m)$ analytically in contrast to the numerical results for this model obtained in Ref. [5]. Reformulating the eigenvalue problem in dimensionless terms, multiplying Eq. (4.15) by $R/\hbar v$, gives

$$\tilde{H}_{\mathrm{DS}}(q_m)\boldsymbol{\Psi}_\lambda(\theta,\phi) = \lambda\boldsymbol{\Psi}_\lambda(\theta,\phi). \quad (4.16)$$

First, the solution of the eigenvalue problem for $q_m \in \mathbb{Z}$ which corresponds to the Dirac quantization condition, is given in App. B of Ref. [5] and

can be fully done by exploiting the symmetries of the system. In this case the dimensionless energy eigenvalues of the system are given by

$$\epsilon_\kappa = \pm\sqrt{\left(\kappa + \frac{1}{2}\right)^2 - \frac{q_m^2}{4}}, \tag{4.17}$$

with a degeneracy of $2\kappa + 1$.

Here, $\kappa = \frac{q_m+1}{2}, \frac{q_m+3}{2}, \ldots$ represents the quantum number associated with the square of total mechanical angular momentum which is denoted as $\boldsymbol{K}(q_m)$. The latter is given by applying the replacement (4.12) to the total angular momentum components (4.2a), (4.2b). This spectral structure arises from the full spherical symmetry of the system with respect to the total mechanical angular momentum operator

$$[H_{\mathrm{DS}}(q_m), K_z(q_m)] = [H_{\mathrm{DS}}(q_m), K_\pm(q_m)] = 0, \tag{4.18}$$

see appendix B of Ref. [5].

It is important to note that this symmetry holds strictly for integer flux q_m only. For these values the components of $\boldsymbol{K}(q_m)$ form an SU(2)-algebra. While the physical existence of the Dirac string breaks the symmetry with respect to the total angular momentum $\boldsymbol{J}^{(l)}$, the system retains invariance under the total mechanical angular momentum $\boldsymbol{K}(q_m)$ for integer flux values q_m. This can also be explained by the Aharonov-Bohm phase associated with the Dirac string becoming trivial, effectively rendering the string unobservable. This condition is not satisfied for non-integer flux. Therefore, we concentrate on the values $q_m \in \mathbb{R} \setminus \mathbb{Z}$, for which this symmetry argument cannot be exploited and no analytical solution has been provided.

For q_m being non-integer, we closely follow the solution of the eigenvalue problem for $q_m = 0$ which is done in detail by Abrikosov in Ref. [18]. Essentially, the magnetic monopole transformation given in Eq. (4.12) can be applied to the differential equations for the $q_m = 0$ problem, so a similarly modified solution ansatz can be used.

To begin with, we can simplify the eigenvalue problem by exploiting the remaining symmetries of the Hamiltonian. For the Hamiltonian $H_{\mathrm{DS}}(q_m)$, this is the rotational symmetry around the z-axis with respect to the total angular momentum, namely

$$\left[H_{\mathrm{DS}}(q_m), J_z^{(l)}\right] = 0. \tag{4.19}$$

Therefore, the eigenstates of the Hamiltonian can be chosen as simultaneous eigenstates of $J_z^{(l)}$ which implies

$$\boldsymbol{\Psi}_\lambda(\theta,\phi) = \frac{e^{im\phi}}{\sqrt{2\pi R^2}}\begin{pmatrix}\alpha_{\lambda m}(\theta)\\ \beta_{\lambda m}(\theta)\end{pmatrix} \equiv \frac{e^{im\phi}}{\sqrt{2\pi R^2}}\boldsymbol{\chi}_{\lambda m}(\theta) \tag{4.20}$$

where $\chi_{\lambda,m}(\theta)$ is the polar spinor. The eigenvalues of the z-component of the total angular momentum are $\hbar m$ with $m \in \{\pm 1/2, \pm 3/2, \dots\}$.

Inserting this ansatz into the dimensionless eigenvalue equation yields the coupled differential equations

$$-i\left(\partial_\theta + \frac{\cot\theta}{2}(1-q_m) + \frac{m-\frac{q_m}{2}}{\sin\theta}\right)\beta_{\lambda m}(\theta) = \lambda\alpha_{\lambda m}(\theta), \tag{4.21a}$$

$$-i\left(\partial_\theta + \frac{\cot\theta}{2}(1+q_m) - \frac{m-\frac{q_m}{2}}{\sin\theta}\right)\alpha_{\lambda m}(\theta) = \lambda\beta_{\lambda m}(\theta). \tag{4.21b}$$

Decoupling the equations and using the coordinate transformation $x = \cos(\theta)$ yields

$$\left[\frac{d}{dx}(1-x^2)\frac{d}{dx} - \frac{(m-\frac{q_m}{2})^2 - (\sigma_z+q_m)(m-\frac{q_m}{2})x + \frac{1}{4}}{1-x^2}\right]\begin{pmatrix}\alpha_{\lambda m}(x)\\ \beta_{\lambda m}(x)\end{pmatrix} = -\left(\lambda^2 - \frac{1}{4}\right)\begin{pmatrix}\alpha_{\lambda m}(x)\\ \beta_{\lambda m}(x)\end{pmatrix}. \tag{4.22}$$

These are the same decoupled differential equations obtained as for $q_m = 0$ case in Ref. [18], but with the replacements given in Eq. (4.12) applied. This suggests that we use a similar ansatz for the polar spinor as for $q_m = 0$, namely

$$\begin{pmatrix}\alpha_{\lambda m}(x)\\ \beta_{\lambda m}(x)\end{pmatrix} = \begin{pmatrix}(1-x)^{\frac{\alpha+1}{2}}(1+x)^{\frac{\beta+1}{2}}\xi_{\lambda m}(x)\\ (1-x)^{\frac{\alpha-1}{2}}(1+x)^{\frac{\beta-1}{2}}\eta_{\lambda m}(x)\end{pmatrix} \tag{4.23}$$

with the parameters

$$\alpha_{\sigma_z} = |\tilde{m}| - \frac{1}{2}\operatorname{sgn}(\tilde{m})[\sigma_z + q_m], \tag{4.24a}$$

$$\beta_{\sigma_z} = |\tilde{m}| + \frac{1}{2}\operatorname{sgn}(\tilde{m})[\sigma_z + q_m]. \tag{4.24b}$$

Here, $\tilde{m} = m - \frac{q_m}{2}$ is the quantum number associated with the total mechanical angular momentum z-component $K_z(q_m)$.

Then we arrive at the equations

$$\left\{(1-x^2)\frac{d^2}{dx^2} + \left[\frac{\tilde{m}}{|\tilde{m}|}(\sigma_z+q_m) - (2|\tilde{m}|+2)x\right]\frac{d}{dx} - \zeta\right\}\begin{pmatrix}\xi_{\lambda m}(x)\\ \eta_{\lambda m}(x)\end{pmatrix} = 0 \tag{4.25}$$

where $\zeta \equiv |\tilde{m}|(|\tilde{m}|+1) - \left(\lambda^2 - \frac{1}{4}\right)$. Using the coordinate transformation $z = \frac{1-x}{2}$, we can rewrite the differential equation for each component into

$$\left\{z(1-z)\frac{d^2}{dz^2} + [\alpha_{\sigma_z} + 1 - (\alpha_{\sigma_z} + \beta_{\sigma_z} + 2)z]\frac{d}{dz} + \zeta\right\}\mathrm{Y}^{\sigma_z}_{\lambda m}(z) = 0 \tag{4.26}$$

defining the reduced polar spinor

$$\mathbf{Y}_{\lambda m}(z) \equiv \begin{pmatrix} \xi_{\lambda m}(z) \\ \eta_{\lambda m}(z) \end{pmatrix}. \tag{4.27}$$

To keep the notation simple, we do not rename the functions ξ and η after the coordinate transformation, despite the formal mathematical requirement to do so. From now on, we use the $\sigma_z = \pm 1$ index notation to indicate which component of the polar spinor differential equation we consider.

The differential Eq. (4.26) is of the hypergeometric type which is discussed in the corresponding App. B, including its solutions. Generally, the hypergeometric differential equation reads

$$x(1-x)\frac{d^2w}{dx^2} + [c - (a+b+1)x]\frac{dw}{dx} - abw = 0 \tag{4.28}$$

with parameters a, b, c and the hypergeometric function is denoted by ${}_2F_1\,(a, b; c; x)$. To make use of the general results to the solution of this differential equation discussed in App. B, we have to identify the parameters a, b, c in Eq. (4.26).

The parameter c is readily obtained as

$$c_{\sigma_z} = \alpha_{\sigma_z} + 1. \tag{4.29}$$

The parameters a and b are be obtained by reading off the relations $ab = \zeta$ and $a + b = \alpha_{\sigma_z} + \beta_{\sigma_z} + 1$. These values can be substituted into the quadratic equation

$$t^2 - (a+b)t + ab = 0, \tag{4.30}$$

which is solved by $t_+ = a$ and $t_- = b$. Solving the quadratic equation yields

$$t_\pm = \frac{a+b}{2} \pm \sqrt{\left(\frac{a+b}{2}\right)^2 - ab} = |\tilde{m}| + \frac{1}{2} \pm |\lambda|, \tag{4.31}$$

which are independent of the component σ_z. It is useful to express the following combination of parameters in terms of α_{σ_z} and β_{σ_z}, namely

$$c_{\sigma_z} - a - b = -\beta_{\sigma_z}. \tag{4.32}$$

The solutions to the hypergeometric differential equation are defined by pairs of functions centered at its singular points. Since the physical interval is restricted to $z \in [0, 1]$, we omit the point at $z = \infty$ and focus on the North Pole ($z = 0$) and the South Pole ($z = 1$). As detailed in App. B, the general solution to (4.26) can be expressed using either of the following linearly independent basis sets.

Near the North Pole ($z = 0$), the basis functions are

$$w_1(z) = {}_2F_1\,(a, b; c_{\sigma_z}; z) \tag{4.33a}$$

$$w_2(z) = z^{1-c_{\sigma_z}}\,{}_2F_1\,(1 + a - c_{\sigma_z}, 1 + b - c_{\sigma_z}; 2 - c_{\sigma_z}; z)\,. \tag{4.33b}$$

Alternatively, near the South Pole ($z = 1$), the basis functions are given by

$$w_3(z) = {}_2F_1\left(a, b; a + b - c_{\sigma_z} + 1; 1 - z\right) \tag{4.34a}$$

$$w_4(z) = (1-z)^{c_{\sigma_z}-a-b}\,{}_2F_1\left(c_{\sigma_z} - a, c_{\sigma_z} - b; c_{\sigma_z} - a - b + 1; 1 - z\right). \tag{4.34b}$$

The general solution $Y^{\sigma_z}_{\lambda m}(z)$ is then a linear combination of either $\{w_1, w_2\}$ or $\{w_3, w_4\}$, with the choice determined by the criterion of normalizability of the wavefunction. Namely, we are searching for a solution that fulfills

$$\int_0^\pi d\theta \sin(\theta) \boldsymbol{\chi}_{\lambda m}(\theta)^\dagger \boldsymbol{\chi}_{\lambda m}(\theta) = \sum_{\sigma_z = \pm} \int_0^\pi d\theta \sin(\theta) \left|\chi^{\sigma_z}_{\lambda m}(\theta)\right|^2 < \infty. \tag{4.35}$$

We focus on the the power-law behaviour for $\theta \to 0$ which corresponds to $z \to 0$, of the possible polar spinor solutions (4.23). This determines if the function is square integrable at the North Pole. We keep in mind that the hypergeometric series is not necessarily convergent for arbitrary parameters, so after determining the normalizable solution we fix either the first or second argument of the hypergeometric functions to be a negative integer so that the series terminates. This yields the Jacobi polynomial functions as solutions, see App. B, similar to the $q_m = 0$ solution examined in Ref. [18].

The powers of the different solutions are determined by the parameters (4.24a) and (4.24b) which depend on q_m.

We can limit the monopole charge to positive values due to the point symmetry stated in Eq. (4.14). The dimensionless flux is parameterized as $q_m = l + \gamma$, with the integer part $l \in \mathbb{N}_0$ and the fractional part $\gamma \in (0, 1)$ which is similar to Ch. 3. Note that we only focus on non-integer fluxes. Using an arbitrary but fixed integer part l, four cases of possible solutions can be determined which are selected via the criterion of normalizability given by Eq. (4.35). These are shown in the Tab. 4.1.

Sector	Angular Momentum	α_{σ_z}	β_{σ_z}	Solution $Y^{\sigma_z}_{\lambda m}(z)$
I	$m > l + 1/2$ or $m < 0$	> 0	≥ 0	$w_1(z)$
II	$0 < m < l + 1/2$ and $2m > l$	< 0	≥ 0	$w_2(z)$
III	$0 < m < l + 1/2$ and $2m \leq l$	> 0	≤ 0	$w_4(z)$
IV	$m = l + \frac{1}{2}$	$\in (-1, 1)$	≥ 0	$w_1(z)\&w_2(z)$

TABLE 4.1: Parameter sectors and corresponding normalizable solutions of Eq. (4.26) for arbitrary but fixed integer part $l \in \mathbb{N}_0$ of the monopole charge q_m.

From Tab. 4.1, it can be seen that for all values $m \neq l + 1/2$ we are left with a single solution and hence the parameter fixing to obtain Jacobi polynomials can be used. However, for $m = l + 1/2$ the normalizability criterion leaves us with two solutions so it is treated seperately in the next section and the focus is on $m \neq l + 1/2$ here.

Using the solutions from Tab. 4.1, there are three free constants left undetermined. Two of them are the integration constants for each σ_z component of the solution $Y_{\lambda m}(z)$ and the third is the dimensionless energy λ.

To relate the two integration constants we use either of the coupling equations (4.21a) or (4.21b). This calculation is provided in App. C, so the final polar spinor is stated in the following.

The energy on the other hand is independent of the coupling and determined by requiring that the hypergeometric series terminates, as discussed above. This ensures the regularity of our solutions. We go through each sector defined in table 4.1 separately to determine the dimensionless energy.

Starting with sector I, we require $a = -n$ with $n \in \mathbb{N}_0$ to terminate the hypergeometric series. Thus determining the dimensionless energy

$$\lambda = \pm \left| n + |\tilde{m}| + \frac{1}{2} \right| . \tag{4.36}$$

Note that in this case the requirement $a = -n$ applies to both components $Y^{\sigma_z}_{\lambda m}(z)$ similarly. The corresponding polar spinor for $\mathrm{sgn}(m) = +1$ reads

$$\begin{pmatrix} \alpha_{\lambda m}(x) \\ \beta_{\lambda m}(x) \end{pmatrix} = N_{I,1} \begin{pmatrix} (1-x)^{\frac{\alpha_{+1}}{2}} (1+x)^{\frac{\beta_{+1}}{2}} P_n^{(\alpha_{+1},\beta_{+1})}(x) \\ \frac{i}{\lambda}(\beta_{+1}+n)(1-x)^{\frac{\alpha_{-1}}{2}} (1+x)^{\frac{\beta_{-1}}{2}} P_n^{(\alpha_{-1},\beta_{-1})}(x) \end{pmatrix} \tag{4.37}$$

and for $\mathrm{sgn}(m) = -1$ it reads

$$\begin{pmatrix} \alpha_{\lambda m}(x) \\ \beta_{\lambda m}(x) \end{pmatrix} = N_{I,2} \begin{pmatrix} (1-x)^{\frac{\alpha_{+1}}{2}} (1+x)^{\frac{\beta_{+1}}{2}} P_n^{(\alpha_{+1},\beta_{+1})}(x) \\ -\frac{i}{\lambda}(\alpha_{+1}+n)(1-x)^{\frac{\alpha_{-1}}{2}} (1+x)^{\frac{\beta_{-1}}{2}} P_n^{(\alpha_{-1},\beta_{-1})}(x) \end{pmatrix} \tag{4.38}$$

with normalization constant $N_{I,1}, N_{I,2}$. Here $P_n^{(\alpha,\beta)}(x)$ denotes the Jacobi polynomials as defined in App. B.

For sector II we require $1 + b - c_{\sigma_z} = -n_{\sigma_z}$ being a negative integer. Here the requirement is different for each component. However, it can be shown that

$$-n_{+1} - (-n_{-1}) = \alpha_{-1} - \alpha_{-1} = \mathrm{sgn}(\tilde{m}) = +1 \tag{4.39}$$

which implies choosing $n_{+1} \in \mathbb{N}_0$ so that $n_{-1} \in \mathbb{N}$ is properly fixed as well. Thus, both components have a finite series by imposing a single condition. Defining $n_{+1} \equiv n$ we calculate the dimensionless energy for this sector

$$\lambda = \pm \left| n + 1 + \frac{q_m}{2} \right| . \tag{4.40}$$

The corresponding polar spinor is determined as

$$\begin{pmatrix} \alpha_{\lambda m}(x) \\ \beta_{\lambda m}(x) \end{pmatrix} = N_{II} \begin{pmatrix} (1-x)^{-\frac{\alpha_{+1}}{2}} (1+x)^{\frac{\beta_{+1}}{2}} P_n^{(-\alpha_{+1},\beta_{+1})}(x) \\ -\frac{2i}{\lambda}(n+1)(1-x)^{-\frac{\alpha_{-1}}{2}} (1+x)^{\frac{\beta_{-1}}{2}} P_n^{(-\alpha_{-1},\beta_{-1})}(x) \end{pmatrix} \tag{4.41}$$

with normalization constant N_{II}.

For sector III we can proceed similar to sector II. We require $c_{\sigma_z} - b = -n_{\sigma_z}$ while fixing $n \equiv n_{+1} \in \mathbb{N}_0$. In turn, this also fixes n_{-1} so both components yield a finite series. The dimensionless energy turns out to be the same as for sector II, in Eq. (4.40). In addition to that, the polar spinor is also similar and determined as

$$\begin{pmatrix} \alpha_{\lambda m}(x) \\ \beta_{\lambda m}(x) \end{pmatrix} = N_{III} \begin{pmatrix} (1-x)^{\frac{1}{2}\alpha_{+1}}(1+x)^{-\frac{1}{2}\beta_{+1}} P_n^{(\alpha_{+1},-\beta_{+1})(x)} \\ -\frac{2i}{\lambda}(n+1)(1-x)^{\frac{1}{2}\alpha_{-1}}(1+x)^{-\frac{1}{2}\beta_{-1}} P_n^{(\alpha_{-1},-\beta_{-1})(x)} \end{pmatrix} \tag{4.42}$$

with normalization constant N_{III}. This spinor is the same one as for sector II because the signs of α_{σ_z} and β_{σ_z} change which can be read off of Tab. 4.1.

For sector IV it is not possible to fulfill the condition because out of the pair of solutions $w_1(z)$ and $w_2(z)$ both are allowed. By fixing $a = -n$ with $n \in \mathbb{N}_0$ the solution $w_1(z)$ is a finite series, but on the other hand this implies

$$1 + a - c_{\sigma_z} = n - |\tilde{m}| + \frac{1}{2}\,\mathrm{sgn}(\tilde{m})[\sigma_z + q_m] \tag{4.43}$$

cannot be a negative integer due to q_m being non-integer. Therefore, the hypergeometric series $w_2(z)$ does not terminate. Sector IV is the critical subspace, namely $m = m^* \equiv l + \frac{1}{2}$. This problem is similar to the problem in Ch. 3 which is why it was treated it in the first place. The solution for the critical subspace is derived in the next section.

4.3 Regularization of the critical subspace

In the prior section the energies $E(q_m)$ for sectors I to III have been derived. However, the energies are linear in the number of magnetic flux quanta q_m. Thus, they do not yield the energies which continuously evolve into a zero mode for the subsequent integer of flux quanta, as they are found in the numerical study in Ch. 4.3 of Ref. [5]. This is what we expect to find for the energies of sector IV, where $m = m^*$. If not explicitly mentioned otherwise, we have $m = m^*$ in this section.

First, we note that the problem is both physically and hence mathematically similar to the the Dirac disc in Ch. 3. Imagine zooming in on the North Pole of the sphere essentially yields a flat surface which is pierced by the Dirac string. Therein, we can ignore the radial monopole field as the contribution of the string is much larger in the proximity of the North Pole. Similar to the Dirac disc we are left with two solutions in the critical subspace instead of a single one which requires an additional boundary condition at the origin. Intuitively the boundary condition has to be set for the North Pole because this is where the Dirac string pierces the surface of the sphere leading to singular behavior in the Hamiltonian.

In App. C the relationship of the two integration constants in each component of the polar spinor is solved. The result for the polar spinor reads

$$\begin{pmatrix}\alpha_{\lambda m}(z)\\ \beta_{\lambda m}(z)\end{pmatrix} = A\begin{pmatrix} z^{\frac{\alpha_{+1}}{2}}(1-z)^{\frac{\beta_{+1}}{2}}{}_2F_1\left(a,b;c_{+1};z\right)\\ -\frac{2i}{\lambda}z^{\frac{\alpha_{-1}}{2}}(1-z)^{\frac{\beta_{-1}}{2}}(1-\frac{a}{c_{+1}})(1-\frac{b}{c_{+1}}){}_2F_1\left(a,b;c_{-1};z\right)\end{pmatrix}$$
$$+B\begin{pmatrix} z^{-\frac{\alpha_{+1}}{2}}(1-z)^{\frac{\beta_{+1}}{2}}{}_2F_1\left(1+a-c_{+1},1+b-c_{+1};2-c_{+1};z\right)\\ -\frac{2i}{\lambda}z^{-\frac{\alpha_{-1}}{2}}(1-z)^{\frac{\beta_{-1}}{2}}(1-c_{+1}){}_2F_1\left(1+a-c_{-1},1+b-c_{-1};2-c_{-1};z\right)\end{pmatrix} \tag{4.44}$$

with the constants A, B.

Next, the Dirac sphere Hamiltonian $H_{\mathrm{DS}}(q_m)$ given in Eq. (4.11) is considered in the limit of $\theta \ll 1$ which corresponds to zooming in on the North Pole. In this limit the Hamiltonian is given by

$$H_{\mathrm{DS}}(q_m) \approx -\frac{i\hbar v}{R}\left[\sigma_x\left(\partial_\theta + \frac{1}{2\theta}\right) + \sigma_y\frac{1}{\theta}\left(\partial_\phi - iq_m\right)\right]. \tag{4.45}$$

We define the new radial coordinate $r' \equiv \theta R$. In the limit $\theta \ll 1$ the radial coordinate is in a regime $r' \lesssim R_{\mathrm{flat}} \ll R$. The coordinate r' serves as a polar radial coordinate for the flat regime around the North Pole. Thus, the Hamiltonian close to the North Pole reads

$$H_{\mathrm{NP}} \equiv -i\hbar v\left[\sigma_x\left(\partial_{r'} + \frac{1}{2r'}\right) + \sigma_y\frac{1}{r'}\left(\partial_\phi - iq_m\right)\right]. \tag{4.46}$$

We want to bring this Hamiltonian into the form of the Dirac disc H_D, as defined in (3.1) which makes the equivalence of the problem to the Dirac disc in Ch. 3 immediate. This can be done by applying the unitary transformation $U = e^{-i\frac{1}{2}\sigma_z(\phi+\frac{\pi}{2})}$ to the Hamiltonian H_{NP} which yields

$$H_{\mathrm{D}} = UH_{\mathrm{NP}}U^\dagger = -i\hbar v\left[\sigma_{r'}\partial_{r'} + \sigma_\phi\frac{1}{r'}(\partial_\phi - iq_m)\right]. \tag{4.47}$$

The transformation maps the local to the Cartesian spinor basis. This can be seen from $UJ_z^{(l)}U^\dagger = J_z^{(c)}$. Specifically, the transformation acts on the Pauli matrices as

$$\sigma_{r'} \equiv U\sigma_xU^\dagger = \sigma_x\cos\phi + \sigma_y\sin\phi \tag{4.48a}$$
$$\sigma_\phi \equiv U\sigma_yU^\dagger = \sigma_x\sin\phi - \sigma_y\cos\phi \tag{4.48b}$$

resulting in the Dirac disc Hamiltonian H_{D} as defined in (3.1). Therefore, the the Dirac sphere model close to the North Pole is unitary equivalent to the Dirac disc problem, treated in Ch. 3. This implies that the regularization introduces a term with σ_z which breaks the chiral symmetry with respect to σ_z for the critical subspace where $m = m^*$.

Consequently, the regularization of the Dirac sphere model near the North Pole mirrors that of the Dirac disc, linked via the unitary operator U. It is

important to note, however, that even though the models are locally connected their underlying differential equations remain fundamentally distinct on a global scale. The local connection (4.47) only implies that the limiting behaviour of the solutions for $\theta \to 0$ is the same, namely the power-law behaviour of the radial spinor for the Dirac disc and the polar spinor for the Dirac sphere.

Nevertheless, the regularization of the Dirac sphere model near the North Pole can be obtained from the Dirac disc through the unitary transformation U. By applying the relation (4.47) to the regularized Dirac disc model

$$H_{\mathrm{NP}}^{\mathrm{reg}} \equiv U^{\dagger} H_{\mathrm{D}}^{\mathrm{reg}} U, \tag{4.49}$$

we can infer that the regularized solution for the sphere is expressed as a linear combination of the original unregularized solution of $H_{\mathrm{DS}}(q_m)$ and an additional quadratic component. Namely, the regualrized solution takes the form of Eq. (3.61).

The quadratic spinor in the regularized solution is exactly of the same form as for the Dirac disc, up to the transformation U, assuming the scale separation $r^* \ll R_{\mathrm{flat}}$. If the quadratic solution only exists on the scale $r^* \ll R_{\mathrm{flat}}$, the curvature of the sphere is negligible, justifying the use of local, flat-space momentum for the regularization term. This allows us to circumvent the fundamental differences between the Laplace operator on the Riemann sphere, provided in Ref. [18], and the Euclidean form as the regularization remains purely local.

Thus, the regularized solution for the polar spinor reads

$$\boldsymbol{\chi}_{\lambda m}^{\mathrm{reg}}(\theta) = \boldsymbol{\chi}_{\lambda m}(\theta) + \boldsymbol{\chi}^{q}(\theta) \tag{4.50}$$

with the quadratic solution

$$\begin{aligned} \boldsymbol{\Psi}^{q}(\theta,\phi) &= U^{\dagger} \begin{pmatrix} Ce^{il\phi} K_{\gamma}(r'/r^*) \\ -Ce^{i(l+1)\phi} K_{1-\gamma}(r'/r^*) \end{pmatrix} \\ &= Ne^{im\phi} \begin{pmatrix} K_{\gamma}(\theta R/r^*) \\ iK_{1-\gamma}(\theta R/r^*) \end{pmatrix} \\ &= e^{im\phi} \boldsymbol{\chi}^{q}(\theta) \end{aligned} \tag{4.51}$$

with constants C and N. Here, $r^* = \hbar/mv$ with the mass m from the squared momentum term in the regularized Hamiltonian given by Eq. (4.49).

The first equality relies on the quadratic solution of the Dirac disc (3.59), evaluated at the radial coordinate r' for a negative charge $q = -e < 0$. Introducing this negative charge has two immediate effects. It interchanges the modified Bessel functions between the spinor components, and it shifts the critical subspace from $n^* = -l - 1$ for $q > 0$ to $n^* = l$ for $q < 0$ which is reflected in the angular momentum. Furthermore, the unitary transformation $U^{\dagger}$ changes the angular momentum representation. Consequently, while the critical subspace in the Cartesian basis is labeled by $n^* = l$ (the $L_z^{(c)}$ eigenvalue of the upper spinor component), it is identified in the local spinor basis

by $m^* = l + 1/2$ (the $J_z^{(l)}$ eigenvalue).

In Ch. 3 we deduced the boundary condition

$$\chi^{\text{reg}}(0) = 0 \tag{4.52}$$

for the regularized model which also applies here following the discussion of equivalence. Rewriting the boundary condition as

$$\lim_{\theta\to 0} \frac{\chi_{\lambda m,1}(\theta)}{\chi_{\lambda m,2}(\theta)} = \lim_{\theta\to 0} \frac{\chi_1^q(\theta)}{\chi_2^q(\theta)} \tag{4.53}$$

we find the ratio of the constants

$$f(\gamma,\lambda) \equiv \frac{A}{B} = -\frac{2\Gamma(\gamma)}{\lambda\Gamma(1-\gamma)}(1-c_{+1})\left(\frac{r^*}{R}\right)^{-1+2\gamma}. \tag{4.54}$$

As in the case of the Dirac disc in Ch. 3, the ratio r^*/R with the power-law governed by the fractional part of the flux γ shows up in the expression.

Now it is left to determine the energy of the state. This can be achieved by imposing regularity of the solution, namely that it has no divergences. This is essentially what is achieved for the sectors I to III by requiring the hypergeometric series to terminate, leading to Jacobi polynomials. However, in the case of a linear combination of two hypergeometric functions given in (4.44) we have to consider the other singularity point of the hypergeometric functions, namely the South Pole $\theta = \pi$ or $z = 1$.

Thus, the asymptotic behavior of the polar spinor (4.44) has to be considered. As $z \to 1$, see App. B, the hypergeometric function behaves as

$$\lim_{z\to 1} {}_2F_1(a,b;c;z) = \frac{\Gamma(c)\Gamma(c-a-b)}{\Gamma(c-a)\Gamma(c-b)} + \frac{\Gamma(c)\Gamma(a+b-c)}{\Gamma(a)\Gamma(b)}(1-z)^{c-a-b}, \tag{4.55}$$

where a, b, c are arbitrary parameters. In turn, in the South Pole limit each of the four hypergeometric solutions contributes a term

$$(1-z)^{c_{\sigma_z}-a-b} = (1-z)^{2-c_{\sigma_z}-(1+a-c_{\sigma_z})-(1+b-c_{\sigma_z})} = (1-z)^{-\beta_{\sigma_z}}, \tag{4.56}$$

which arises from the second term in (4.55). In the polar spinor (4.44) this implies an overall limiting behaviour $(1-z)^{-\beta_{\sigma_z}/2}$ for each component. That leads to a divergence at the South Pole because $\beta_{\sigma_z} > 0$. Therefore, the prefactor of this contribution has to vanish which then determines λ. Proceeding in this manner, we obtain the condition

$$f(\gamma,\lambda)\frac{\Gamma(c_{+1})}{\Gamma(a)\Gamma(b)} + \frac{\Gamma(2-c_{+1})}{\Gamma(1+a-c_{+1})\Gamma(1+b-c_{+1})} = 0, \tag{4.57}$$

leaving us with an implicit equation for the energy λ. It can be shown that the condition is independent of which component is considered and is the same for both.

In Eq. (4.57) it can be seen that the energy depends on the magnetic monopole

charge q_m and also on the regularization scale r^*/R which is contributed by $f(\gamma,\lambda)$. This result is similar to the Dirac disc regularization in Ch. 3, where we also found an implicit equation for the energy in terms of the magnetic flux strength and the regularization scale, see Eq. (3.70).

Not only does this relationship determine the energy, but it also provides us with a way to rewrite the solution (4.44) into a simpler form, where the regularity at $z=1$ becomes more apparent. For this, the linear transformation

$$\begin{aligned}{}_2F_1(a,b;a+b-c+1;1-z) &= \frac{\Gamma(a+b-c+1)\Gamma(1-c)}{\Gamma(1+a-c)\Gamma(1+b-c)}{}_2F_1(a,b;c;z)\\ &+\frac{\Gamma(2-c)\Gamma(a+b-c+1)}{\Gamma(a)\Gamma(b)}z^{1-c}{}_2F_1(1+a-c,1+b-c;2-c;z),\end{aligned} \tag{4.58}$$

which maps from the $z=1$ basis into the $z=0$ basis is needed, see App. B. Applying this relation to the polar spinor (4.44) together with the condition (4.57) and the reflection identity $\Gamma(z+1)=z\Gamma(z)$ we obtain

$$\begin{pmatrix}\alpha_{\lambda m}(z)\\ \beta_{\lambda m}(z)\end{pmatrix} = A\begin{pmatrix} z^{\frac{\alpha_{+1}}{2}}(1-z)^{\frac{\beta_{+1}}{2}}{}_2F_1\left(a,b;a+b-c_{+1}+1;1-z\right)\\ -\frac{2i}{\lambda}z^{\frac{\alpha_{-1}}{2}}(1-z)^{\frac{\beta_{-1}}{2}}(c_{+1}-a-b){}_2F_1\left(a,b;a+b-c_{-1}+1;1-z\right)\end{pmatrix}. \tag{4.59}$$

In this form it can be seen that the condition (4.57) which determines the energy, provides the regularity of the solution at the South Pole.

4.4 Results

The full spectrum of $H_{\mathrm{DS}}(q_m)$ is shown in Fig. 4.2, following the solution of the prior section.

First, the energies for integer q_m, given by Eq. (4.17), are derived in Ref. [5] with a degeneracy of $2\kappa+1$. It can be seen that the analytical results for fractional magnetic flux reproduce this behavior in the limit of $\gamma\to 0$, namely integer fluxes q_m. For example, the lowest positive energy state splits into two states for $q_m>0$, owing to its double degeneracy for $q_m=0$. Moreover, at integer fluxes the spectrum is symmetric $E=0$ which corresponds to the chiral symmetry. This chiral symmetry is restored only in the non-critical subspaces for non-integer flux values q_m, whereas it is broken for the critical subspace m^* due to the regularization term.

Turning to fractional flux values q_m, the most striking feature is that the lowest positive energy in the critical subspace $m^*=l+\frac{1}{2}$ continuously forms a zero mode for $\gamma\to 1$, whereas all other energies in this subspace merge with the non-critical linear spectrum. Both of these transitions in the critical subspace take place around $\gamma\approx 1/2$, independent of the integer part of the flux. The energies in the critical subspace are determined by the condition (4.57). Therein, the function $f(\gamma,\lambda)$ contains the regularization scale

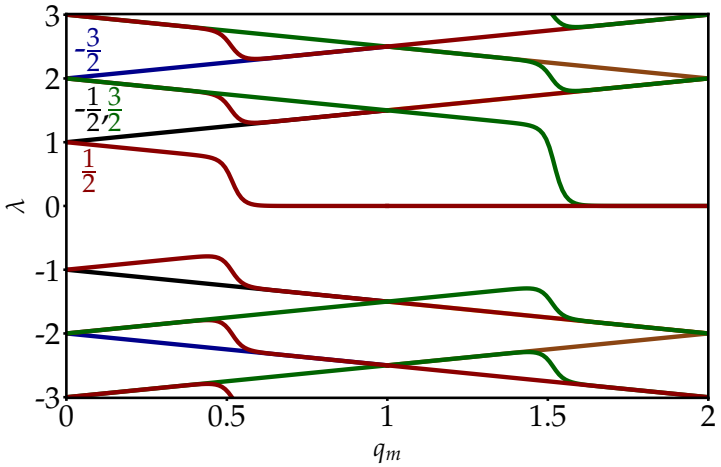

FIGURE 4.2: Dimensionless energy spectrum of $H_{\mathrm{DS}}(q_m)$ plotted against the monopole charge q_m for $r^*/R = 10^{-10}$. The curves correspond to different total angular momentum quantum numbers m which are color-coded and explicitly annotated. The different energies labeled by n belong to the same m so they share a uniform color scheme for either positive or negative values. Notably, the lowest positive energy level in the critical subspace descends to a zero mode, while the higher positive energies and all negative energies within this subspace merge with the non-critical spectrum.

ratio r^*/R that governs the sharpness of these transitions. For $r^*/R \to 0$ the transition becomes a sharp step function. However, similar to the Dirac disc result from Ch. 3 the energy at $\gamma = 1/2$ is independent of the scale ratio.

This continuous formation of a single zero mode towards the next integer flux q_m for each interval is exactly what is numerically predicted in Ref. [5]. Finally, we can connect the spinors in the critical subspace forming a zero mode to the zero modes analytically calculated in Ref. [5] for integer monopole charges $q_m \in \mathbb{Z}$. For dimensionless flux $q_m \in \mathbb{N}$, the zero modes are given by spinors of the form $\mathbf{\Psi} = (0, \psi_2)^T$ where the component ψ_2 is obtained as

$$\psi_2(\theta,\phi) = e^{i(m_\kappa + q_m/2)\phi} \left(\cos\frac{\theta}{2}\right)^{m_\kappa} \left(\sin\frac{\theta}{2}\right)^{-m_\kappa} (\sin\theta)^{\frac{q_m}{2}-\frac{1}{2}}. \tag{4.60}$$

Here, m_κ represents the quantum number of the kinetic total angular momentum z-component $K_z(q_m)$ and takes on values $m_\kappa = -\frac{q_m-1}{2}, \ldots, \frac{q_m-1}{2}$ which corresponds to a number of q_m zero modes. For q_m between two integers, the number of zero modes remains at $\lfloor q_m \rfloor$ with the exact same m_κ as for $\lfloor q_m \rfloor$ but with fractional values $\lfloor q_m \rfloor \mapsto q_m$ inserted.

Consider, for example, the transition $q_m = 1 \to 2$. The state with $m_\kappa = 0$ which forms the single zero mode at $q_m = 1$, remains at zero energy, evolving into the $m_\kappa = -1/2$ mode due to $m_\kappa = 1/2 - q_m/2$. Simultaneously, the state with $m = 3/2$ which belongs to the critical subspace m^* in this regime

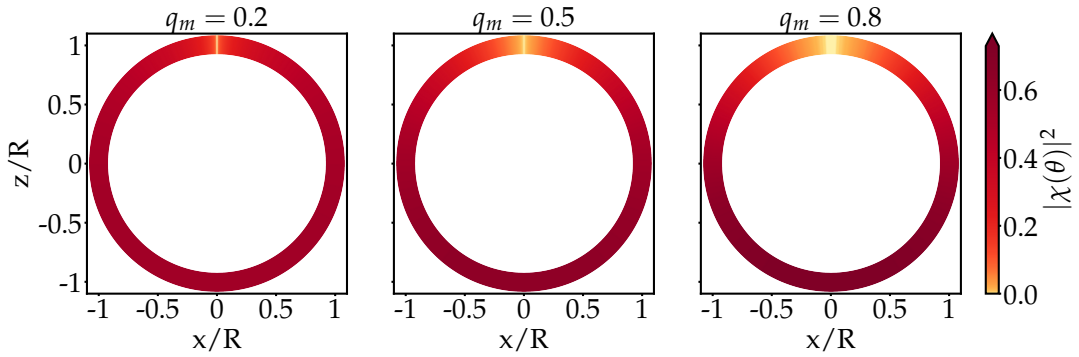

(A) State with lowest positive energy for $m = -\frac{1}{2}$.

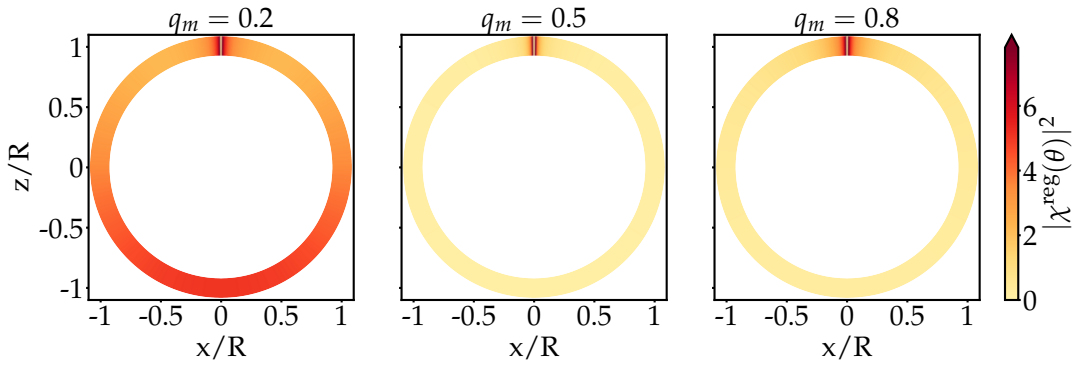

(B) Regularized state (4.50) in the critical subspace with lowest positive energy for $m = m^* = \frac{1}{2}$.

FIGURE 4.3: Polar probability density $|\chi|^2$ for different flux values q_m with $l = 0$ and different subspaces m, specified in the panel captions (A) and (B). The scale ratio is chosen as $r^*/R = 10^{-10}$, chosen according to $r^* \ll R_{\text{flat}} \ll R$. Note that while the density is plotted on a ring of finite thickness for visualization purposes, the particle is physically confined to the sphere's two-dimensional surface at radius R.

descends in energy to become a zero mode, ultimately forming the $m_\kappa = +1/2$ zero mode at $q_m = 2$. This results in two zero modes at $q_m = 2$, namely $m_\kappa = \pm\frac{1}{2}$.

As the flux is further increased from $q_m = 2 \to 3$, these two modes remain at zero energy, while a third zero mode emerges from the critical subspace. This process continues for each interval, repeatedly adding one zero mode each time which then remains at zero. The added zero mode always corresponds to the highest possible m_κ, while the other zero modes' m_κ decrease in the process. The zero modes are also plotted in Fig. 4.2.

The physical stability of these zero modes can be understood by examining the behavior of the wavefunction at the North Pole $\theta = 0$. At $q_m = 1$, the wavefunction with maximal m_κ approaches a constant non-zero value as $\theta \to 0$. As q_m increases, this wavefunction develops a node, so the wavefunction vanishes as $\theta \to 0$. This pattern repeats for each interval. For any integer q_m, the zero mode with the highest m_κ transitions to having a node at

the North Pole as q_m increases further.

Since the lower m_κ modes already possess such nodes, the wavefunctions effectively vanish at the location of the Dirac string piercing at the North Pole, rendering them physically insensitive to the string's presence and ensuring they remain at zero energy.

Turning to the non-critical subspaces $m \neq m^*$, it can be seen that the energies decrease or increase exactly linearly with the magnetic flux q_m. The energies in the subspaces $m > l + \frac{1}{2}$ only decrease linearly because the flux q_m has yet to reach the strength so that the states enter the critical subspace which forces its lowest positive energy into a zero mode.

Lastly, all the positive energies for all subspaces $m < l + \frac{1}{2}$ increase linearly because they already contributed a zero mode which stays at zero which implies the non-zero energies cannot enter a critical subspace again for growing q_m. The chiral symmetry dictates the opposite behavior for the corresponding negative energies.

The zero modes in the Dirac Hamiltonian's spectrum have a special physical meaning. To understand this we need Dirac's hole theory of the Dirac equation. For example, we can consider the spectrum for $q_m = 0$. We have infinitely many negative and positive energies which are symmetric around $E = 0$ due to the chiral symmetry. To define a vacuum, we need to fill the infinite negative energy states which is called the Dirac sea with the charge Q_{vac} and energy E_{vac}.

Technically, both the vacuum charge and energy are infinite but if only differences with respect to the vacuum are considered the infinities cancel out. Then, occupied positive energy states correspond to electronic states carrying a charge $-e$ and energy $+E$. On the other hand, when removing a state from the Dirac sea this produces a hole which is also an excited state with respect to the vacuum. The hole carries the opposite charge $Q_{\text{vac}} - (-e) - Q_{\text{vac}} = +e$ and positive energy $E_{\text{vac}} - (-E) - E_{\text{vac}} = +E$.

However, if the energy of a state is at $E = 0$, as it is the case for $q_m = 1$, the state belongs both to the electronic states and the Dirac sea [21]. Suppose the state has some undetermined charge q_0. If the state is occupied, it has to contribute a charge $-e$ in total because it is an electronic state. If it is unoccupied, the hole carries the opposite charge $-q_0$ because the state also belongs to the Dirac sea. Therefore, we have $Q_{\text{vac}} + q_0 - (Q_{\text{vac}} - q_0) = -e$ which means the zero mode carries a charge $q_0 = -e/2$. However, this means that in the continuous formation of such a zero mode the charge $-e$ the state originally carries has to fractionalize.

The numerical results for the critical subspace state's probability density in Ref. [5] hint at an explanation to resolve where the other half of the charge goes in the process. In the simulation the critical subspace's surface states are not only localized at the Dirac string but also coupled into the bulk along the Dirac string because the simulation is done on a spherical shell of finite thickness. It is supposed that once the full sphere is taken into account the critical subspace surface states couple to the bulk and carry $-e/2$ to the magnetic monopole along the Dirac string during the process of $\gamma = 0 \to 1$.

If the critical subspace's state is occupied in the beginning of the process it carries a charge $-e$, but as it has formed a zero mode at the end of the process it only carries $-e/2$. The charge transport to the magnetic monopole would explain the half charge that is missing from the surface. A similar continuous fracitonalization process is also numerically simulated in Ref. [9] for a spherical TI and in Ref. [10] for a monopole in a cubic TI. Moreover, this observation is consistent with the Witten effect, which predicts that a magnetic monopole carrying an integer flux quantum in a 3D TI binds half an electronic charge [7].

To compare these results we also look at the probability density associated to the eigenstates. In Fig. 4.3 it is shown how the probability density associated to the lowest positive energy for $m = \pm 1/2$ changes for q_m away from zero. Note that both states start with the same probability density for $q_m = 0$, namely a constant distribution.

For $m = 1/2$, shown in Fig. 4.3a, the probability density develops a zero-node at the North Pole which means the particle avoids the Dirac string for non-zero q_m. The size of the node increases with q_m.

Conversely, for the critical subspace $m = -1/2$ shown in Fig. 4.3b, the probability density exhibits a peak close to the North Pole where it approaches zero because of the regularization and the corresponding boundary condition. This peak emerges from the regularized solution and the behavior is similar to the regularized state on the disc, shown in Fig. 3.7.

The peak intensifies as the fractional flux part $\gamma \to 1/2$, where it reaches a maximum before subsequently decreasing. Note that this effect is independent of the integer part of the flux. This indicates that the particle is localized along the Dirac string, with the strongest confinement occurring at $\gamma = 1/2$, similar to the the result in Ref. [5].

It is natural that our analytical result does not reflect the coupling to the bulk because we only consider the surface in our model. However, the localization at the Dirac string, which is strongest at fractional flux value $\gamma = 1/2$, does hint at this fractional charge transport that is suggested to take place around the rapid transition for $\gamma \approx 1/2$ [5].

While fully confirming this requires incorporating surface-bulk coupling, the current analytical framework already demonstrates strong agreement with the numerical results from Ref. [5]. Especially, the spectral flow of the surface states in Fig. 4.2 agrees with the numerical prediction and thus shows we have found an analytical framework that extends to arbitrary flux values q_m.

Chapter 5

Fractional charge pumping in the Dirac sphere

The preceding chapter established the analytical framework for the topological surface states of a Dirac sphere hosting a central magnetic monopole. Within this framework, we demonstrated that the formation of a zero mode necessitates charge fractionalization, resulting in the relocation of $-e/2$ away from the surface. However, this purely two-dimensional surface model fundamentally does not yield a direct description of the charge transport into the sphere's interior as suggested by numerical results [5, 9, 10].

To fully capture the charge transport into the sphere's interior, we must now extend our theoretical description into the three-dimensional bulk of the topological insulator. This chapter develops a corresponding bulk Hamiltonian model to investigate the coupling between the surface and the interior along the Dirac string. By analyzing the bulk states localized at the Dirac string, we aim to explicitly describe the continuous transport mechanism that carries half an electron charge from the surface to the magnetic monopole in the process of increasing the dimensionless magnetic flux by an integer.

5.1 Dirac string bound states

In this section we consider the bulk Hamiltonian of the 3D BHZ-model

$$H_{\mathrm{BHZ}} = \left[Mv^2 + \frac{1}{\mu}\boldsymbol{p}^2 \right] \tau_z + v[\boldsymbol{\sigma} \cdot \boldsymbol{p}]\tau_x, \tag{5.1}$$

established in Sec. 2.3. Here, M and μ have dimensions of mass and v is the surface state velocity. Moreover, the topological regime of this Hamiltonian is given by $M < 0$, while $\mu > 0$ is fixed in the remainder of this section. Conversely, the trivial regime is then given by $M > 0$.

A remark regarding the surface model derived from Eq. (5.1) is in order, as it remains essential for the remainder of this chapter. In Sec. 2.3 the surface model is derived from Eq. (5.1), but with the quadratic momentum term set to zero. However, accounting for the quadratic momentum term introduces the characteristic length scales $r_\mu = \hbar/\mu v$ and $r_M = \hbar/Mv$ for the localized surface states [22]. In the topological regime, $-0.25 < r_\mu/r_M < 0$ is required for exponential localization of the surface states. In addition to this, for a sphere of radius R it can be shown that $r_\mu, |r_M| \ll R$ has to hold so surface

states are localized strong enough to avoid overlap between opposite sites of the sphere.

Numerical results strongly suggest the existence of bulk states bound to the Dirac string [5, 9, 10]. We therefore focus our analysis on the local region immediately surrounding this singularity. In this vicinity, the radial magnetic field contribution from the monopole itself becomes negligible. The dominant field is entirely dictated by the singular flux string. This local isolation is completely analogous to the flat-space limit analyzed for the surface model of the Dirac sphere in Ch. 4.

This localized gauge field is described using the pure Aharonov-Bohm flux

$$\boldsymbol{A} = -\frac{\Phi}{2\pi r}\boldsymbol{e}_\phi, \tag{5.2}$$

which we have already established for the Dirac disc model in Ch. 3. As we want to connect the results of the bulk model to the surface states from Ch. 4, the same notation for the dimensionless magnetic flux $q_m = \Phi/\Phi_0 = l + \gamma$ is employed.

Including the vector potential via minimal coupling into H_{BHZ} yields the Hamiltonian

$$H_{\text{string}} = \left[Mv^2 + \frac{1}{\mu}\boldsymbol{\Pi}^2\right]\tau_z + v[\boldsymbol{\sigma}\cdot\boldsymbol{\Pi}]\tau_x, \tag{5.3}$$

with the kinetic momentum $\boldsymbol{\Pi} = \boldsymbol{p} + e\boldsymbol{A}$. From now on, p_z is set to zero in H_{string} because we aim to find bound states in the x, y-plane. Then, the Hamiltonian H_{string}, with $p_z \neq 0$, can be projected into the subspace of the bound states to find an effective Hamiltonian for the z-direction.

To solve for the bound states, we make use of the symmetry

$$[H_{\text{string}}, J_z] = 0, \quad J_z = L_z + S_z \tag{5.4}$$

with z-component of the total angular momentum denoted by J_z. In contrast to the prior section, we solely work in the Cartesian spinor basis, similar to Ch. 3, so we drop the superscript on the operators.

The symmetry allows to separate the eigenstates into an angular and radial part

$$\boldsymbol{\Psi}_n(\mathbf{r}) = e^{in\phi}\begin{pmatrix} u_{\sigma_z=+1,\tau_z=+1}(r) \\ v_{\sigma_z=+1,\tau_z=-1}(r) \\ e^{i\phi}u_{\sigma_z=-1,\tau_z=+1}(r) \\ e^{i\phi}v_{\sigma_z=-1,\tau_z=-1}(r) \end{pmatrix}, \tag{5.5}$$

where $r = \sqrt{x^2+y^2}$. Similar to Ch. 3, n is the quantum number of the canonical angular momentum of the spin-up component. In general, the radial function depends on the component with respect to τ_z and σ_z which is denoted by the subscripts. In the following, only the critical subspace with $n = n^* = l$ is considered because the surface states in the corresponding critical subspace $m = m^*$ show localization along the string and descend to zero energy, thus leading to charge fractionalization.

The basis can be reordered so the Hamiltonian has a block structure. This is achieved by using the basis

$$\{|\uparrow_\tau\uparrow_\sigma\rangle, |\downarrow_\tau\downarrow_\sigma\rangle, |\downarrow_\tau\uparrow_\sigma\rangle, |\uparrow_\tau\downarrow_\sigma\rangle\}, \tag{5.6}$$

with the product states of the ± 1 eigenstates of τ_z and σ_z. In this basis, the Hamiltonian reads

$$H_{\text{string}} = \begin{pmatrix} M(\mathbf{\Pi}) & v\Pi_- & 0 & 0 \\ v\Pi_+ & -M(\mathbf{\Pi}) & 0 & 0 \\ 0 & 0 & -M(\mathbf{\Pi}) & v\Pi_- \\ 0 & 0 & v\Pi_+ & M(\mathbf{\Pi}) \end{pmatrix}, \tag{5.7}$$

where $\Pi_\pm = \Pi_x \pm i\Pi_y$ and $M(\mathbf{\Pi}) = Mv^2 + \frac{1}{\mu}\mathbf{\Pi}^2$. The upper block and lower block basis are defined by the first two and last two entries of the set given in Eq. (5.6), respectively.

The Hamiltonian possesses a chiral symmetry $\{H_{\text{string}}, \tau_y\} = 0$. The operator τ_y maps between the upper and lower block basis. Thus, we only have to solve for the bound state in the upper block and immediately get the solution of the lower block via

$$H_{\text{string}}\tau_y |\psi\rangle = -E\tau_y |\psi\rangle, \tag{5.8}$$

where $|\psi\rangle$ is the eigenstate of the upper block with energy E.

The upper block Hamiltonian can be written as

$$H_{\text{b}} = \left(Mv^2 + \frac{1}{\mu}\mathbf{\Pi}^2\right)\alpha_z + v\boldsymbol{\alpha}\cdot\mathbf{\Pi}, \tag{5.9}$$

with $\boldsymbol{\alpha} = (\alpha_x, \alpha_y, \alpha_z)^T$ being the vector of Pauli matrices which act in the upper block basis. The Hamiltonian H_{b} has the same form as the regularized Dirac disc Hamiltonian (3.42), up to a unitary transformation and an additional constant mass term M. This particular model is studied in Sec. III of Ref. [9] which is referred to for a detailed solution. The solution is mathematically similar to the method used for the regularized model in Ch. 3 as well.

Following the results obtained in Ref. [9], the eigenstate for H_{b} reads

$$\boldsymbol{\psi}^{\text{b}}(r,\phi) = \frac{e^{il\phi}}{N}\begin{pmatrix} \left(\frac{1}{r_M} + k - r_\mu\kappa_-^2\right)\left(\frac{\kappa_+}{\kappa_-}\right)^\gamma K_\gamma(\kappa_- r) - \left(\frac{1}{r_M} + k - r_\mu\kappa_+^2\right)K_\gamma(\kappa_+ r) \\ ie^{i\phi}\left[-\left(\frac{\kappa_+}{\kappa_-}\right)^\gamma \kappa_- K_{1-\gamma}(\kappa_- r) + \kappa_+ K_{1-\gamma}(\kappa_+ r)\right] \end{pmatrix}, \tag{5.10}$$

with normalization constant N. The vector is expressed with respect to the upper block basis.

This state fulfills the regularized boundary condition $\boldsymbol{\psi}^{\text{block}}(r \to 0, \phi) = 0$ derived in Ch. 4. The constants are found as

$$\kappa_{\pm} = \frac{1}{r_\mu}\sqrt{\frac{(1+2r_\mu/r_M) \pm \sqrt{(1+2r_\mu/r_M)^2 - 4(1/r_M^2 - k^2)r_\mu^2}}{2}}. \tag{5.11}$$

Therein, the length scales r_μ, r_M appear and the energy $E = \hbar v\varepsilon/|r_M| \equiv \hbar v k$ is introduced. The state is strongly localized on the scale of r_μ around the string but avoids the location $r = 0$ of the string itself.

Moreover, the eigenenergy is determined by the implicit equation

$$\frac{(r_\mu\kappa_+)^{1+\delta} - (r_\mu\kappa)^{1+\delta}}{(r_\mu\kappa_-)^{1+\delta} - (r_\mu\kappa_-)^{1+\delta}} = \frac{r_\mu}{r_M}(1+\varepsilon), \tag{5.12}$$

where the fractional part of q_m is parametrized by $\gamma = \frac{1+\delta}{2}$. Here, the ratio $-0.25 < r_\mu/r_M = M/\mu < 0$ enters. This ratio is negative due to the TI being in the topological regime but its absolute value depends on specific material parameters so it is kept arbitrary.

Note that in contrast to the Dirac disc case, we only obtain two solutions with $\kappa_\pm$ for the model treated here. Therefore, the boundary condition at the origin is enough to determine the energy and there is no additional boundary condition needed.

Finally, the state given in Eq. (5.10) expressed in the basis (5.6) reads

$$|\Psi\rangle = \psi_1^{\text{b}}(r,\phi)|\uparrow_\tau\uparrow_\sigma\rangle + \psi_2^{\text{b}}(r,\phi)|\downarrow_\tau\downarrow_\sigma\rangle. \tag{5.13}$$

From the state $|\Psi\rangle$ we also obtain the eigenstate of the lower block using the chiral symmetry. It is given by

$$|\Lambda\rangle = i\psi_1^{\text{b}}(r,\phi)|\downarrow_\tau\uparrow_\sigma\rangle - i\psi_2^{\text{b}}|\uparrow_\tau\downarrow_\sigma\rangle, \tag{5.14}$$

with the the energy determined by equation (5.12) but with $\varepsilon \mapsto -\varepsilon$.

The bound state energies for the the upper and lower block eigenstates are plotted in Fig. 5.1. The energies lie within the range $\pm|M|v^2$. That is, they lie in the gap of the BHZ Hamiltonian's spectrum given by

$$E_\pm = \sqrt{v^2\boldsymbol{p}^2 + \left(Mv^2 + \frac{1}{\mu}\boldsymbol{p}^2\right)^2} \xrightarrow[|\boldsymbol{p}|\to 0]{} \pm|M|v^2. \tag{5.15}$$

The spectrum is directly obtained from diagonalizing the Hamiltonian (5.1). This property renders the states $|\Psi\rangle, |\Lambda\rangle$ as bound states. Hence, these are the bulk states bound to the Dirac string we have searched for.

The sharpness of the transition which takes place around $\delta = 0$, or $\gamma = 1/2$, is governed by the ratio $|M/\mu|$ and becomes a step function in the limit $|M/\mu| \to 0$. However, as the masses M, μ are material parameters for a real 3D TI and thus can vary, we use an arbitrary but fixed finite ratio in the following.

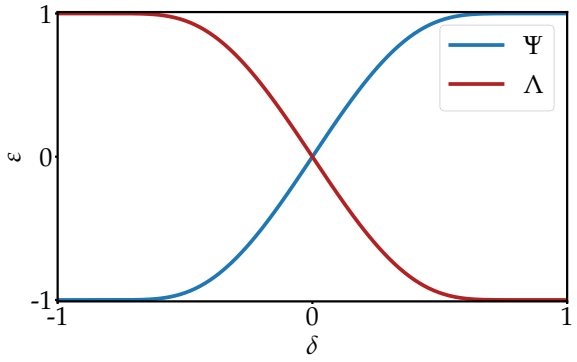

FIGURE 5.1: Dimensionless bound state energy ε of the upper and lower block eigenstate. The energy is determined by equation (5.12) and shown against δ for the arbitrary ratio $r_\mu/r_M = -0.01$, see main text. For half a flux quantum $\gamma = 1/2$, the string supports a zero-energy bound state whereas it converges to ± 1, or with dimensions attached $\pm|M|v^2$, for $\delta \to \pm 1$.

Furthermore, the bound state energy is degenerate at $\gamma = 1/2$ with $\varepsilon(1/2) = 0$.

The states $|\Psi\rangle, |\Lambda\rangle$ span the orthonormal subspace of bound states we want to project the Hamiltonian H_{string}, given in Eq. (5.3), into. With this projection we obtain an effective model for the z-direction which only takes the states bound to the Dirac string into account, as suggested by the results of Refs. [5, 9, 10]. Note that p_z is not set to zero from here on.

The projected Hamiltonian is given by

$$H_z = \sum_{i,j=\Psi,\Lambda} \langle i| H_{\text{string}} |j\rangle |i\rangle \langle j| . \tag{5.16}$$

Calculating the matrix elements yields

$$H_z = \left[E(\gamma) + \frac{W(\gamma)}{\mu} p_z^2 \right] \lambda_z - v p_z \lambda_y \tag{5.17}$$

with

$$W(\gamma) = \int d^2\boldsymbol{r} \left[\left| \psi_1^{\text{b}}(r,\phi) \right|^2 - \left| \psi_2^{\text{b}}(r,\phi) \right|^2 \right] \tag{5.18}$$

and the upper block bound state energy $E(\gamma) = \hbar v/|r_M| \varepsilon(\gamma)$ where $\varepsilon(\gamma)$ is given by Eq. (5.12). Here, the dependence on the fractional part of the dimensionless magnetic flux γ is explicitly denoted.

A new degree of freedom within the bound state subspace is introduced. Therein, the Pauli matrices acting in this two-dimensional subspace are denoted by $\lambda_x, \lambda_y, \lambda_z$. In this subspace $|\Psi\rangle = (1,0)^T$ and $|\Lambda\rangle = (0,1)^T$ are identified.

As discussed in the next section, we focus on the low-energy regime $p_z \ll$

$\hbar/r_\mu, \hbar/|r_M|$ so the quadratic momentum term can be ignored. This yields the linear model

$$H_z \approx E(\gamma)\lambda_z - v p_z \lambda_y, \tag{5.19}$$

describing the z-direction model. For an infinitely long string, the spectrum reads

$$E_z = \pm\sqrt{E(\gamma)^2 + v^2 p_z^2}. \tag{5.20}$$

The energy gap of the spectrum is given by $\pm|E(\gamma)|$ and varies with the magnetic flux of the string. Hence, the gap vanishes exactly for half a flux quantum in the system, namely $\gamma = 1/2$. Thus, our model predicts a gapless mode along the Dirac string similar to Ref. [10]. In Ref. [10] this gapless mode is responsible for the "wormhole effect" and transports the charge that accumulates at the surface of the TI to the magnetic monopole which is confirmed by numerical simulations. It is also worth noting that the gapless mode is still exact when considering the quadratic term with $W(\gamma)$ which can be shown to be zero at $\gamma = 1/2$, so that the spectrum remains gapless at that point.

5.2 Effective scattering model

Having derived the Hamiltonian H_z for states propagating along the Dirac string, we now aim to explicitly quantify the charge transported along it. To this end, we employ an effective 1D scattering model which is directly motivated by Brouwer's scattering approach to adiabatic charge pumping [23]. While the formal details of this framework are deferred to Sec. 5.3, its scattering-based setup provides a method for calculating the pumped charge for our system. In the following, we derive the scattering model for the system which consists of the outer surface, the Dirac string and the magnetic monopole.

Given the z-rotational symmetry of the surface states discussed in Ch. 4, the azimuthal part of its wavefunction is separable, allowing us to focus exclusively on the polar part of the spinor given by Eq. (4.59). By applying the mapping $\theta = r'/R$ for a sphere of radius R near the North Pole, the polar part can be decomposed into radially incoming and outgoing 1D modes. The incoming and outgoing modes propagate towards and away from the North Pole, respectively which is depicted by corresponding arrows in Fig. 5.3a in two separate directions to indicate the rotational symmetry. This representation is analogous to expressing a standing wave as a superposition of counter-propagating traveling waves, i.e. the bound states in the infinite potential well.

However, finding an explicit analytical decomposition of the surface states into these individual 1D modes is not strictly necessary for our calculation. Instead, we make the simplifying assumption that the incoming and outgoing modes of the surface states map directly onto the asymptotic scattering states of the Dirac string described by $H_s \equiv -v p_z \lambda_y$. The Hamiltonian H_s is equivalent to the Hamiltonian H_z but with a vanishing gapping term because the surface states are not bound to the Dirac string. Then, the transmission

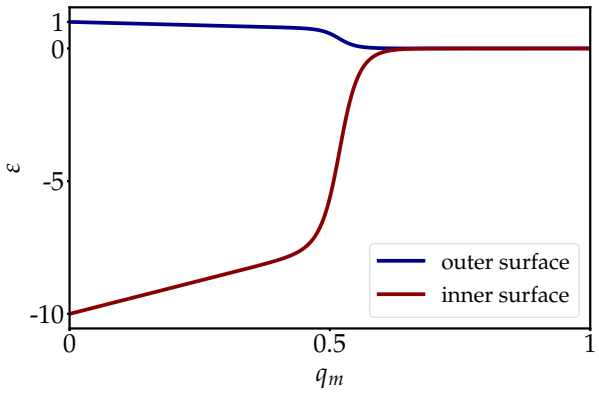

FIGURE 5.2: The dimensionless energy $\varepsilon = \frac{ER}{\hbar v}$ of the inner and outer surface state in the critical subspace $m = m^* = 1/2$ which descend to zero energy, shown for $q_m \in [0, 1]$ and $r^*/R = 10^{-10}$. The inner surface radius is set to $R = 10R_i$ so the energy of the inner surface is rescaled compared to the outer surface. The inner surface state energy has opposite sign to the outer surface state energy as discussed in the main text.

and reflection properties of the Dirac string are rigorously described by the scattering matrix S that can be calculated via the Hamiltonian H_z.

Moreover, an inner cavity with radius R_i that closely surrounds the magnetic monopole is added, which the Dirac string connects the outer spherical surface to. This inner boundary models the magnetic monopole, allowing for bound states that bind the pumped charge. Furthermore, as shown in Ref. [9], the magnetic monopole naturally creates this additional domain wall for the inner boundary. We consider a small inner spherical cavity $R_i \ll R$ such that the length of the Dirac string $L = R - R_i$ can be approximated as $L \approx R$.

This inner surface supports surface states governed by the Hamiltonian

$$H_{\mathrm{DS,i}}(q_m) = \frac{i\hbar v}{R_i}\left\{\sigma_x\partial_\theta + \frac{\sigma_y}{\sin(\theta)}\left[\partial_\phi - i\frac{q_m}{2} - i\frac{\cos(\theta)}{2}(\sigma_z + q_m)\right]\right\}. \quad (5.21)$$

This expression matches the outer surface Hamiltonian $H_{\mathrm{DS}}(q_m)$ given by Eq. (4.11) but introduces an overall negative sign and replaces the radius R with the inner surface radius R_i.

The sign inversion originates from the opposite surface normal vector $\hat{\boldsymbol{n}} \mapsto -\hat{\boldsymbol{n}}$ which enters for the surface Hamiltonian derived Sec. 2.3. Consequently, the energy spectrum matches that of the outer surface but is inverted. Furthermore, the condition $R/R_i \gg 1$ implies that these inner surface energies are significantly larger than those of the outer surface.

The only exception is the lowest energy mode of the critical subspace $m = m^*$. This specific mode descends toward zero energy and is the sole state that approaches the Fermi energy $E_F = 0$ of the outer and inner surface. We focus on the Fermi energy because it is the energy at which the the scattering model for the charge pumping in Sec. 5.3 has to be considered. The comparison

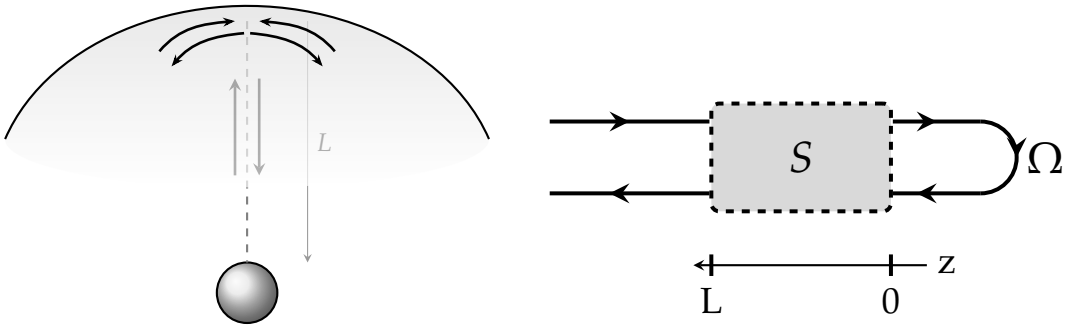

(A) (B)

FIGURE 5.3: The effective model for the charge transport along the Dirac string before and after unraveling the surface states in Panel (A) and (B), respectively. Panel (A) depicts the radially ingoing and outgoing states on the outer spherical surface as well as the states that travel along the string in z-direction in two directions. The Dirac string is visualized by a dashed line which is connected to the inner spherical surface that surrounds the monopole. Panel (B) shows the unraveled 1D model of the outer surface states coupled via the Dirac string, with scattering matrix S, to the inner surface with a constant reflection phase $\Omega \in [0, 2\pi)$ visualized by the closed arc.

between the critical subspace energy, descending to zero energy, for the inner and outer surface is shown in Fig. 5.2.

The inner surface is incorporated into the model through a bound state $E_B = E_B(\gamma) < 0$ it hosts, which the scattering states of the outer surface and the Dirac string interact with. The bound state is spatially located at $z = 0$, where the inner cavity connects to the Dirac string. As discussed, the bound state energy E_B is identified with the specific inner surface mode that approaches zero as γ transitions from 0 to 1. This state naturally lies in the critical subspace which has to be considered.

The influence of the bound state on the scattering process is described through a reflection matrix of the Breit-Wigner form

$$S_{\mathrm{BW}}(E, \gamma) = e^{i\phi_{\mathrm{bg}}} \frac{E - E_B - i\frac{\Gamma}{2}}{E - E_B + i\frac{\Gamma}{2}} \tag{5.22}$$

with an additional constant background phase shift ϕ_{bg}, which is not fixed yet. Here, Γ denotes the resonance width. The scattering matrix depends on the magnetic flux through the bound state energy E_B. However, the Dirac string is strongly gapped away from $\gamma = 1/2$ in the low energy regime considered for H_z. Thus, the outer surface state can only scatter towards the inner cavity in the vicinity of $\gamma = 1/2$. Consequently, the effect of S_{BW} for the charge pumping most important at $\gamma = 1/2$. Thus, for the remainder of this section $E_B = E_B(\gamma = 1/2)$ is considered, if not stated otherwise.

The absolute squared value of the coupling matrix element between the Dirac string and the inner surface determines the resonance width $\Gamma > 0$.

In the following section, it is shown that the specific nature of this coupling does not influence the total pumped charge. Furthermore, one can argue that $\Gamma \ll |E_B|$ because the coupling depends on the overlap of the wavefunctions on the surface and within the Dirac string.

This coupling is approximately determined by the overlap of the inner surface wavefunction and the Dirac string state at their intersection on the North Pole of the inner surface. The wavefunction of the Dirac string state is localized along its length L, yet only its two dimensional intersection of area $\propto r_\mu^2$ contributes. Due to $r_\mu \ll R \approx L$, as argued in Sec. 5.1, the overlap is strongly suppressed. More precisely, the ratio is approximately $\Gamma/E_B \sim r_\mu/L \ll 1$. Additionally, the wavefunction of the inner surface state is localized at the North Pole, but not exponentially. It remains spread out across the surface, which further minimizes the overlap. This can be seen from the surface state in the critical subspace given in Eq. (4.59).

We fix the background phase shift by considering the scattering matrix at $E = E_F = 0$. Because of the narrow resonance limit, where $\Gamma \ll |E_B|$, the Breit-Wigner approximation simplifies to $S_{\mathrm{BW}}(0) \approx e^{i\phi_{\mathrm{bg}}}$. Since the bound state energy E_B is negative and has a narrow resonance Γ the scattering at zero energy remains far from resonance and cannot effectively scatter into the inner surface. Consequently, the inner surface is modeled as a hard wall at this energy. A calculation similar to the hard wall boundary condition detailed in Sec. 3.1 yields a background phase of $\phi_{\mathrm{bg}} = -\pi/2$.

The scattering phase shift is defined by the expression

$$\Omega(E,\gamma) = \arg(S_{\mathrm{BW}}(E)) = -\frac{\pi}{2} - 2\arctan\left(\frac{\Gamma/2}{E - E_B}\right). \tag{5.23}$$

Here, $E_B = E_B(\gamma)$ can have arbitrary values γ again. Note that we abbreviate the notation with $\Omega = \Omega(E,\gamma)$.

Thus, we established an effective model constructed from the outer surface, the Dirac string and the inner surface. The setup of the effective model is shown in Fig. 5.3a and Fig. 5.3b before and after mapping it to one dimension, respectively, which we also call unraveling.

To derive the scattering matrix for the Dirac string at Fermi energy $E_F = 0$, we calculate the transfer matrix T which relates the in- and outgoing states at $z = 0$ and $z = L$. The stationary Schrödinger equation for H_z in position space reads

$$[i\hbar v \partial_z \lambda_y + E(\gamma)\lambda_z]\boldsymbol{\psi}(z) = 0. \tag{5.24}$$

From this we gain access to the spatial evolution operator which is determined by the differential equation

$$\partial_z \boldsymbol{\psi}(z) = -\frac{1}{\hbar v} E(\gamma)\lambda_x \boldsymbol{\psi}(z). \tag{5.25}$$

This is solved by

$$\boldsymbol{\psi}(0) = T\boldsymbol{\psi}(L) \text{ with } T = e^{KL}, \tag{5.26}$$

where $K = \frac{E(\gamma)}{\hbar v}\lambda_x$. The matrix exponential evaluates to

$$T = \cosh(\eta L)\mathbb{I} + \sinh(\eta L)\lambda_x \tag{5.27}$$

using $\eta = \eta(\gamma) = \frac{E(\gamma)}{\hbar v} = \frac{\varepsilon(\gamma)}{|r_M|}$.

To gain access to the scattering matrix, the action of the transfer matrix on the in- and outgoing states of the surface has to be determined. As discussed, the scattering states are defined by the free Hamiltonian $H_s = -vp\lambda_y$. In the coordinate system depicted in Fig. 5.3b the in- and outgoing states correspond to the right- and left-moving states, respectively. Thus, at Fermi energy $E_F = 0$ the states have the form $\chi_{R,L}$ which are the λ_y eigenstates with eigenvalue ± 1, respectively.

Using $\lambda_x\chi_R = i\chi_L$ and $\lambda_x\chi_L = -i\chi_R$, we obtain

$$T\chi_R = \cosh(\eta L)\chi_R + i\sinh(\eta L)\chi_L, \tag{5.28}$$
$$T\chi_L = \cosh(\eta L)\chi_L - i\sinh(\eta L)\chi_R. \tag{5.29}$$

This yields the matrix elements in the $(\chi_R, \chi_L)^T$ basis

$$T_{RR} = \cosh(\eta L), \tag{5.30}$$
$$T_{LL} = \cosh(\eta L), \tag{5.31}$$
$$T_{LR} = i\sinh(\eta L), \tag{5.32}$$
$$T_{RL} = -i\sinh(\eta L). \tag{5.33}$$

To derive the effective reflection amplitude R_{eff} for a system closed by a wall at $z = 0$ with a reflection phase Ω, the scattering states outside the string have to be determined. For a wave incident from the left $z > L$, the spinor at the interface $z = L$ is a combination of the incoming right-mover and the total reflected left-mover, expressed as $\psi(L) = \chi_R + R_{\text{eff}}\chi_L$. At the interface $z = 0$, the state is composed of right- and left-moving components $\boldsymbol{\psi}(0) = A\chi_R + B\chi_L$.

The inner surface at $z \leq 0$ imposes a boundary condition. That is, given the reflection phase Ω from Eq. (5.23), the reflected wave B is related to the incident wave A by $B = A\exp(i\Omega)$. This is depicted in Fig. 5.3b by the closed arc.

Using the transfer matrix relation $\boldsymbol{\psi}(0) = T\boldsymbol{\psi}(L)$ in the $(\chi_R, \chi_L)^T$ basis yields

$$\begin{pmatrix} A \\ Ae^{i\Omega} \end{pmatrix} = \begin{pmatrix} T_{RR} & T_{RL} \\ T_{LR} & T_{LL} \end{pmatrix} \begin{pmatrix} 1 \\ R_{\text{eff}} \end{pmatrix}. \tag{5.34}$$

Solving this system of equations for R_{eff} gives

$$R_{\text{eff}} = \frac{e^{i\Omega}T_{RR} - T_{LR}}{T_{LL} - e^{i\Omega}T_{RL}}. \tag{5.35}$$

Finally, by substituting the explicit matrix elements for T, we arrive at the full explicit form for the effective reflection amplitude

$$R_{\text{eff}} = \frac{e^{i\Omega}\cosh(\eta L) - i\sinh(\eta L)}{\cosh(\eta L) + ie^{i\Omega}\sinh(\eta L)}, \tag{5.36}$$

which depends on the dimensionless flux γ through $\eta = \eta(\gamma)$.

As constructed by closing the system, we have a purely reflective scattering with $|R_{\text{eff}}| = 1$ restricted to the unit circle in the complex plane. The phase of the reflection is given by

$$\phi_{\text{eff}}(E,\gamma) \equiv \arg\left(R_{\text{eff}}\right) = \Omega - 2\arctan\left(\frac{\cos(\Omega)\tanh(\eta L)}{1-\sin(\Omega)\tanh(\eta L)}\right). \tag{5.37}$$

5.3 Dirac string as charge pump

With the effective scattering model established, it is possible to calculate the pumped charge using Brouwer's scattering theory of parametric pumping [23], which was already announced in the prior section. In this framework, adiabatic charge pumping is driven by the cyclic variation of an external control parameter X, such as a gate voltage or magnetic field which slowly alters the scattering properties of the system connected to leads. Therein, the scattering matrix is evaluated at the Fermi energy and is the reason we focused on this energy in the prior section. The change of the scattering properties can then be converted to a formula to determine the charge pumped out of a lead through the scattering region. For a detailed description, the reader is referred to Ref. [23].

However, our setup is purely reflective and thus solely described by a reflection matrix $r(X)$. Then, the general Brouwer formula for the charge pumped by the system simplifies directly to

$$Q = -\frac{e}{2\pi i}\int_{X_i}^{X_f} dX \frac{d}{dX}\log\det(r(X)), \tag{5.38}$$

as given in Ref. [24, 25]. Here, X_i and X_f are the initial and final parameter, respectively.

In our case the driving parameter is the dimensionless magnetic flux $X \equiv \gamma$ which is varied over a single cycle from 0 to 1. Moreover, the reflection matrix only has a single entry rendering it a scalar and the formula simplifies to

$$Q = -\frac{e}{2\pi}\int_0^1 d\gamma \frac{d}{d\gamma}\phi_{\text{eff}}(E_F,\gamma). \tag{5.39}$$

To evaluate the charge transported in the process of $\gamma = 0 \to 1$, using Eq. (5.39), we need calculate how the phase ϕ_{eff} evolves in this process. For this we analyze $\eta(\gamma)L = (L/|r_M|)\varepsilon(\gamma)$. The length $|r_M| \ll L \approx R$ due to the decay length of the surface states into the bulk, as discussed below Eq. (5.1).

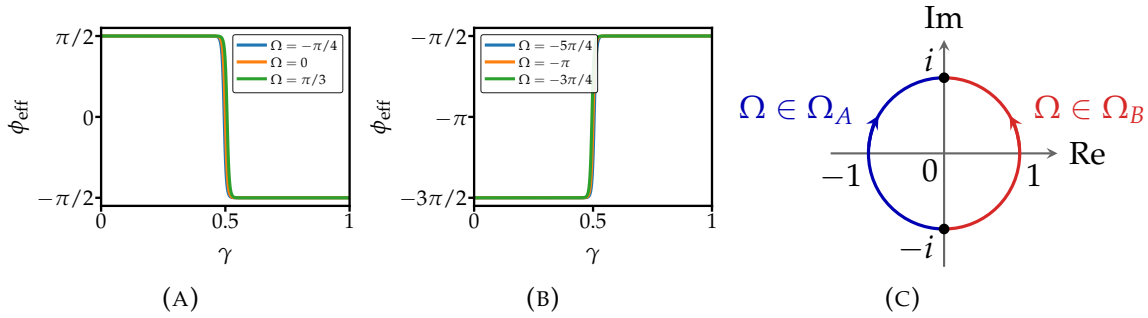

(A) (B) (C)

FIGURE 5.4: Phase evolution and corresponding R_{eff} trajectory in the complex plane for different values of Ω. The parameters are chosen as $r_\mu/r_M = -0.01$ and $L/|r_M| = 10$. Panel (A) [(B)] shows the evolution for the phase ϕ_{eff} as a function of $\gamma \in (0,1)$ for arbitrary $\Omega \in \Omega_A = (-\pi/2, \pi/2)$ [$\Omega \in \Omega_B = (-3\pi/2, -\pi/2)$], winding from what shows to be $\pi/2$ to $-\pi/2$ [$-3\pi/2$ to $-\pi/2$]. See main text for a further discussion of the limiting values. The phase shows a sharp transition around $\gamma = 1/2$ which is where the Dirac string becomes gapless. Panel (C) shows the evolution of R_{eff} for (A) and (B) in the complex plane. This demonstrates that the phase winding is exactly opposite of each other for the two phase choices Ω_A, Ω_B.

The evolution of the effective phase ϕ_{eff} during the pumping cycle is illustrated in Fig. 5.4 for two representative intervals of the bound state reflection phase $\Omega \in \Omega_A \equiv (-\pi/2, \pi/2)$ and $\Omega \in \Omega_B \equiv (-3\pi/2, -\pi/2)$. Note that in contrast to $\Omega(E, \gamma)$ given in Eq. (5.23), Ω is chosen as a constant in the process. This is because we want Fig. 5.4 to show that the total phase winding is strictly governed by which interval Ω lies in and only the transition at $\gamma = 1/2$ depends on the specific value.

The effective phase ϕ_{eff} is 2π-periodic in Ω which means the phase winding always falls in either of the two categories. Moreover, from Eq. (5.37) it can be inferred that for all $\Omega = \pi/2 + n\pi$ with $n \in \mathbb{Z}$ the phase $\phi_{\text{eff}} = \Omega$ is independent of γ. Thus, there is no phase winding and consequently the pumped charge vanishes.

The properties of the phase winding align with the description of the phase $\Omega(E, \gamma)$ via a bound state resonance effect. In Brouwer's formula, we consider the scattering at Fermi energy $E = E_F = 0$ and thus $\Omega(E = 0, \gamma)$ has to be implemented. Then, using Eq. (5.23) we obtain

$$\Omega(0, \gamma) = -\frac{\pi}{2} - 2 \arctan\left(\frac{\Gamma}{2|E_B|}\right) \in \Omega_B \tag{5.40}$$

for $E_B < 0$ which is the case for all $\gamma \in (0,1)$ during the pumping process. Thus, the phase winding and direction of pumped charge is fixed.

This result is completely independent of the specific resonance width $\Gamma > 0$ and consequently the specific coupling of the Dirac string to the inner surface. It is also independent of the specific bound state energy, as it

only depends on the overall sign. It is simply the bound state energy of the inner surface fixing the direction of the charge pumping. Moreover, the scattering never hits a resonance for fractional flux values because the inner surface energy always fulfills $E_B \neq E_F = 0$. Therefore, the pumped charge is non-zero.

In addition to this, a sharp transition around $\gamma = 1/2$ can be seen for all choices of Ω, being slightly shifted for different values in the same set. The sharpness of the transition is determined by $L/|r_M|$ and becomes a step function in the limit $L/|r_M| \to \infty$.

The Brouwer formula (5.39) implies that changes in the phase lead to charge pumping. This suggests that the charge pumping process takes place around $\gamma = 1/2$ because away from that value the phase stays approximately constant. This is due to the Dirac string supporting gapless modes for $\gamma = 1/2$ but away from that value the Dirac string is strongly gapped. The dimensionless strength of the gapping in ϕ_{eff} depends on $L/|r_M|$ which explains why the transition becomes sharper when this ratio becomes large.

This implies that the dependence of Ω on γ through the bound state energy is only important for $\gamma = 1/2$. However, away from $\gamma = 1/2$ the limiting values of the effective phase become independent of the bound state energy as long as $E_B < 0$. As this is the case, there is no dependence on the flux away from $\gamma = 1/2$.

Furthermore, this confirms that it is the Dirac string which is responsible for the charge transport. This result is in accordance with the "wormhole" effect described in Ref. [10].

While the effective phase evolutions shown in Fig. 5.4 visually suggest a precise phase difference of $\Delta\phi_{\text{eff}} = \pm\pi$, this quantization is only exact in the limit $L/|r_M| \to \infty$. For a finite system, the winding acquires an exponential correction governed by the ratio $L/|r_M|$. To see this explicitly, we consider the case $\Omega = -\pi$ where the expression for the effective phase simplifies to $\phi_{\text{eff}}(E_F, \gamma) = -\pi + 2\arctan(\tanh(\eta L))$ as $\Omega = -\pi$ is fixed. Recalling that the argument scales as $\eta(\gamma)L = (L/|r_M|)\varepsilon(\gamma)$, the phase is evaluated at the boundaries of the pumping cycle, corresponding to $\varepsilon(\gamma \to 0) = -1$ and $\varepsilon(\gamma \to 1) = 1$.

The surface states decay rapidly compared to the system size with $L/|r_M| \gg 1$, so we can expand the hyperbolic tangent for large positive arguments as $\tanh(x) \approx 1 - 2e^{-2x}$. The phase at the upper boundary then evaluates to

$$\phi_{\text{eff}}(\gamma \to 1) \approx -\pi + 2\arctan\left(1 - 2e^{-2L/|r_M|}\right) \approx -\frac{\pi}{2} - 2e^{-2L/|r_M|}. \quad (5.41)$$

Similarly, at the lower boundary, the odd symmetry of the hyperbolic tangent yields

$$\phi_{\text{eff}}(\gamma \to 0) \approx -\pi + 2\arctan\left(-1 + 2e^{-2L/|r_M|}\right) \approx -\frac{3\pi}{2} + 2e^{-2L/|r_M|}. \quad (5.42)$$

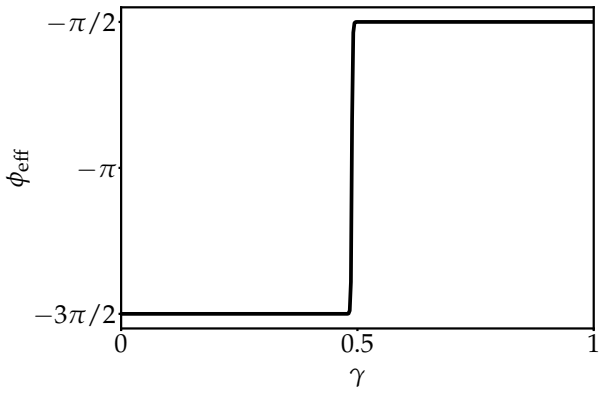

FIGURE 5.5: Evolution for the effective phase $\phi_{\text{eff}}(E_F, \gamma)$, given in Eq. (5.37), with $\Omega(0, \gamma)$, given in Eq. (5.40), in the interval $\gamma \in (0, 1)$. The bound state energy $E_B(\gamma)$ is determined for an inner surface of radius $R_i = R/10$ and $r^*/R = 10^{-10}$. The parameters are chosen as $L/|r_M| = 50$ and $r_\mu/r_M = -0.01$. The evolution shows the expected $\Delta\phi_{\text{eff}} \approx \pi$ phase jump, as discussed in the main text. A sharp transition at $\gamma = 1/2$ can be seen, corresponding to the Dirac string being gapless at this point.

Taking the difference, the total accumulated phase over the complete cycle is

$$\Delta\phi_{\text{eff}} \approx \pi - 4e^{-2L/|r_M|}. \tag{5.43}$$

This demonstrates that any deviation from a perfect π-winding is exponentially suppressed. This can be explained using results from Ref. [9]. Therein, the wavefunction for the full system of a spherical 3D TI with a magnetic monopole and associated Dirac string is analytically calculated at $\gamma = 1$. The wavefunction of the zero mode, which is expected to show charge fractionalization, is partitioned into two exponentially localized surface states at the outer and inner surface. Thus, a residual overlap between these states remains due to their exponential tails preventing a perfect separation of the wavefunction and thus charge.

Finally, applying the charge pump formula given in Eq. (5.38) in the limit $L/|r_M| \gg 1$, the phase winding for $\Omega(E_F, \gamma) \in \Omega_B$ yields a fractional pumped charge of $Q \approx -e/2$ up to the aforementioned finite-size corrections in $L/|r_M|$.

Furthermore, the phase winding of $\phi_{\text{eff}}(E_f, \gamma)$, using $\Omega(E_F, \gamma)$ from Eq. (5.40), is shown in Fig. 5.5. Therein, the γ dependence through the bound state energy is explicitly accounted for, instead of choosing a constant Ω. This confirms that while the process generally depends only on Ω remaining within the interval Ω_B, its precise value becomes critical at $\gamma = 1/2$, where the Dirac string becomes gapless. It can be seen that the effective phase starts to shift close to $\gamma = 1/2$ and reaches $\phi_{\text{eff}} \approx -\pi/2$ at $\gamma = 1/2$, thus completing the phase shift.

The process of charge pumping can now be clearly understood. For $\gamma <$

$1/2$, the wavefunction within the critical subspace accumulates at the North Pole of the outer surface where the Dirac string pierces it, as shown in Ch. 4. When γ approaches $1/2$ the effective phase from our model begins shifting. Then, at $\gamma = 1/2$, the Dirac string becomes gapless. This allows the outer surface state to couple with the magnetic monopole, or the corresponding inner surface, via the Dirac string. During this process, the effective scattering phase in our effective model completes shifting to $\phi_{\text{eff}} \approx -\pi/2$ because of off-resonance scattering at the bound state, residing on the inner surface, which acts as a hard wall.

This phase shift dictates that half an electronic charge is pumped by the Dirac string to the magnetic monopole. Subsequently, for $\gamma > 1/2$, the Dirac string becomes strongly gapped again, keeping the effective phase constant for the rest of the process.

Numerical results from Sec. VII of Ref. [9] present the evolution of the wavefunction, which belongs to the critical subspace, for $\gamma \in [0, 1]$ and integer part $l = 0$ on a lattice. Therein, the full spherical 3D TI with the magnetic monopole and associated Dirac string is simulated so we can compare our findings to the numerical results. The results demonstrate that the relevant wavefunction from the outer surface at $\gamma = 0$ penetrates the bulk as $\gamma \to 1/2$, which initiates the effective phase shifting in our model. Then at $\gamma = 1/2$, the gapless modes of the Dirac string allow the leaked surface wavefunction to localize along the full length of the Dirac string as it supports gapless modes. In turn, this completes the phase shift of the effective phase. For $\gamma > 1/2$, the transition to a gapped Dirac string divides the leaked wavefunction between the inner and outer surfaces and leaves a charge deficit of $e/2$ at the surface relative to the monopole.

Coming back to the analytical model from this chapter, the scattering initially occurs at a Fermi energy $E_F = 0$ where $|E_B| \gg \Gamma$. Consequently, the inner surface acts as a hard wall for the state still residing in the Dirac string. As $\gamma \to 1$, the bound state energy E_B approaches $E_F = 0$ and additionally $|E_B| \approx \Gamma$. Ultimately, this limit allows the wavefunction to leak into the inner surface, or its respective bound state, at the end of the process because of the resonance. This result aligns with the analytical findings of Ref. [9]. The initial wavefunction splits equally between the monopole and the outer surface, resulting in each component carrying a charge of $-e/2$ as predicted by the zero modes and the Witten effect [5, 7]. Thus, we have established an effective model that captures the charge fractionalization and formation of the monopole bound state.

Chapter 6

Conclusion and outlook

This thesis has examined the surface states of a spherical 3D TI, described by the BHZ model, and their spectral flow and charge fractionalization under the variation of a magnetic flux introduced by a monopole-string configuration.

In Ch. 2, the core foundational concepts were established. We demonstrated how surface states arise in two- and three-dimensional TIs via the Jackiw-Rebbi model and derived the respective surface Hamiltonian used to describe the spherical 3D TI. Additionally, the fundamental effects of magnetic fields in quantum mechanics were reviewed through illustrative examples to support the analytical treatments in subsequent chapters.

In Ch. 3, we explored the local flat-space limit at the North Pole of the Dirac sphere with a magnetic monopole and its associated Dirac string, resulting in the Dirac disc pierced by the Dirac string. We addressed the emergence of an ambiguous extra solution within a specific angular momentum subspace when the magnetic flux is given by a fraction of the magnetic flux quantum. To uniquely determine the energy spectrum, we established a new boundary condition at the origin by introducing a regularized continuum model with a quadratic momentum term akin to the Wilson fermion approach on the lattice. This regularization yields a highly localized solution decaying at a characteristic length r^* and forces the radial spinor to vanish at the origin. Consequently, the spectral flow in this critical subspace depends on the ratio r^*/R and acts as a smoothed step function that continuously weights the unregularized analytical solutions.

Building on this flat space framework, Ch. 4 analyzed the surface states of the Dirac sphere with a central magnetic monopole and attached Dirac string. Requiring normalizable solutions revealed the same critical subspace ambiguity found in the Dirac disc where an extra solution necessitates a boundary condition at the North Pole. Applying the quadratic momentum regularization from the Dirac disc, we identified the same highly localized solution and boundary condition at the North Pole, forcing the wavefunction to vanish. This resolved the overall spectral flow and detailed how robust zero energy modes continuously evolve at fractional fluxes. Our analysis demonstrated that these zero modes carry half an elementary charge upon occupation. Finally, we showed that the wavefunction in the critical subspace become localized around the Dirac string and reach maximum localization exactly at half a flux quantum.

In Ch. 5, we extended the Dirac sphere model into the 3D TI bulk to investigate the observed charge fractionalization of the surface states in the critical subspace from Ch. 4. By deriving an effective one-dimensional Hamiltonian for states bound to the Dirac string, we demonstrated that the string supports gapless modes exactly at half a flux quantum, while remaining strongly gapped at all other fractional values. Modeling the magnetic monopole as an inner surface that supports a bound state, we established that a charge of $-e/2$ is pumped using Brouwer's framework for adiabatic charge pumping. The transport sign depends on the inner surface orientation via its bound state energy E_B, and not on the specific coupling between the inner surface and the Dirac string, entering via the resonance width Γ of the bound state. Furthermore, we showed that the pumping occurs along the Dirac string at half a flux quantum, where the string becomes gapless. Finally, we demonstrated that the wavefunction localized at the inner surface binds to the monopole at the end of the flux variation, as the bound state energy approaches zero and the scattering closes in on the resonance, comparing this to analytical and numerical results of Ref. [9].

This thesis is a good starting point to explore and compare alternative regularization procedures beyond the momentum-squared approach used here. A central question for future study is how various regularization schemes lead to the continuous formation of zero modes for the Dirac sphere, allowing for a systematic comparison of their physical effects.

Moreover, it would be interesting to quantify the resonance width Γ from the model in Ch. 5 through the overlap of string and surface wavefunctions. An exact calculation beyond scale comparisons would pinpoint the threshold and regime where the wavefunction leaks from the Dirac string onto the inner surface.

Going further, a natural extension is to derive the exact eigenstates for the complete 3D TI model of the Dirac sphere for fractional magnetic flux. This explicitly incorporates the outer surface, the inner boundary enclosing the monopole, and the Dirac string simultaneously within a single mathematical framework. Building upon the full 3D model, a detailed theoretical analysis of the exact coupling between the 2D spherical surface states and the 1D bulk states bound to the Dirac string would be possible. This also gives access to exactly determine the precise evolution of the wavefunction during the charge pumping process, showing how it splits into two parts and subsequently binds to the monopole and the outer surface.

Appendix A

Bessel functions

This appendix provides a concise reference for the properties of Bessel and modified Bessel functions utilized in this work. The formulas are taken from [26], specifically chapter 10.

Bessel functions

The Bessel differential equation reads

$$x^2y'' + xy' + (x^2 - \nu^2)y = 0. \tag{A.1}$$

For $\nu \notin \mathbb{Z}$ the two independent solutions are $J_{\pm\nu}(x)$, whereas for $\nu \in \mathbb{Z}$ they are $J_\nu(x)$, $Y_\nu(x)$. The Bessel function of the first kind is defined as

$$J_\nu(x) = \sum_{m=0}^{\infty} \frac{(-1)^m}{m!\,\Gamma(m+\nu+1)} \left(\frac{x}{2}\right)^{2m+\nu}, \tag{A.2}$$

with the Gamma function for $\Re(z) > 0$ defined as

$$\Gamma(z) = \int_0^\infty t^{z-1}e^{-t}\,dt. \tag{A.3}$$

The Bessel fucntion of the second kind is defined as

$$Y_\nu(x) = \frac{J_\nu(x)\cos(\nu\pi) - J_{-\nu}(x)}{\sin(\nu\pi)}, \tag{A.4}$$

where the latter only holds for $\nu \notin \mathbb{Z}$ and for $n \in \mathbb{Z}$ we use the limit

$$Y_n(x) = \lim_{\nu\to n} Y_\nu(x). \tag{A.5}$$

Moreover we have $J_{-n}(x) = (-1)^n J_n(x)$ for $n \in \mathbb{Z}$, which shows why in the integer case we need both the Bessel function of the first and second kind to get two linearly independent solutions.

Another important property are the recurrence relations

$$\mathcal{C}_{\nu-1}(x) + \mathcal{C}_{\nu+1}(x) = \frac{2\nu}{x}\mathcal{C}_\nu(x) \tag{A.6a}$$

$$\mathcal{C}_{\nu-1}(x) - \mathcal{C}_{\nu+1}(x) = 2\mathcal{C}'_\nu(x) \tag{A.6b}$$

$$\mathcal{C}_{\nu-1}(x) - \frac{\nu}{x}\mathcal{C}_\nu(x) = \mathcal{C}'_\nu(x) \tag{A.6c}$$

$$-\mathcal{C}_{\nu+1}(x) + \frac{\nu}{x}\mathcal{C}_\nu(x) = \mathcal{C}'_\nu(x) \tag{A.6d}$$

which hold for arbitrary index ν and $C_\nu(x)$ denotes either $J_\nu(x)$ or $K_\nu(x)$.

When ν is fixed and $x \to 0$ we have

$$J_\nu(x) \sim \begin{cases} \dfrac{(-1)^\nu}{|\nu|!}\left(\dfrac{x}{2}\right)^{|\nu|}, & \text{for } \nu \in \mathbb{Z}_{<0} \\ \dfrac{1}{\Gamma(\nu+1)}\left(\dfrac{x}{2}\right)^{\nu}, & \text{else} \end{cases} \tag{A.7}$$

and

$$Y_\nu(x) \sim \begin{cases} \Gamma(\nu)\left(\frac{1}{2}x\right)^{-\nu}, & \text{for } \nu > 0 \\ \cos(|\nu|\pi)\Gamma(|\nu|)\left(\frac{1}{2}x\right)^{-|\nu|}, & \text{for } \nu < 0 \text{ and } \nu \neq -\frac{1}{2}, -\frac{3}{2}, \ldots \end{cases}. \tag{A.8}$$

Modified Bessel functions

The modified Bessel differential equation reads

$$x^2y'' + xy' - (x^2 + \nu^2)y = 0. \tag{A.9}$$

For arbitrary ν the two linearly independent solutions are the modified Bessel function of the first kind $I_\nu(x)$ and the second kind $K_\nu(x)$. The first one is defined as

$$I_\nu(x) = i^{-\nu}J_\nu(ix) \tag{A.10}$$

and second one is defined by

$$K_\nu(x) = \frac{\pi}{2}\frac{I_{-\nu}(x) - I_\nu(x)}{\sin(\nu\pi)} = K_{-\nu}(x), \tag{A.11}$$

where the latter only holds for $\nu \notin \mathbb{Z}$. For $n \in \mathbb{Z}$ we use the limit

$$K_n(x) = \lim_{\nu \to n} K_\nu(x). \tag{A.12}$$

The recurrence relations read

$$\mathcal{Z}_{\nu-1}(x) - \mathcal{Z}_{\nu+1}(x) = \frac{2\nu}{x}\mathcal{Z}_\nu(x), \tag{A.13a}$$

$$\mathcal{Z}_{\nu-1}(x) + \mathcal{Z}_{\nu+1}(x) = 2\mathcal{Z}'_\nu(x), \tag{A.13b}$$

$$\mathcal{Z}_{\nu-1}(x) - \frac{\nu}{x}\mathcal{Z}_\nu(x) = \mathcal{Z}'_\nu(x), \tag{A.13c}$$

$$\mathcal{Z}_{\nu+1}(x) + \frac{\nu}{x}\mathcal{Z}_\nu(x) = \mathcal{Z}'_\nu(x), \tag{A.13d}$$

which hold for arbitrary ν. Here $\mathcal{Z}_\nu(x)$ denotes either of $I_\nu(x)$ or $e^{\nu\pi i}K_\nu(x)$. For the latter the phase factor is important to get the correct phases in the recurrence relations.

Moreover we have the asymptotic behaviours for $x \to \infty$

$$I_\nu(x) \sim \frac{e^x}{\sqrt{2\pi x}} \tag{A.14}$$

$$K_\nu(x) \sim \sqrt{\frac{\pi}{2x}} e^{-x}. \tag{A.15}$$

When ν is fixed and $x \to 0$ we have

$$K_\nu(x) \sim \begin{cases} -\ln\left(\frac{x}{2}\right) - \gamma, & \text{if } \nu = 0 \\ \frac{1}{2}\Gamma(\nu)\left(\frac{1}{2}x\right)^{-\nu}, & \text{if } \nu > 0 \end{cases} \tag{A.16}$$

with the Euler-Mascheroni constant γ.

Appendix B

Gaussian hypergeometric function

This appendix provides a concise reference for the properties of the Gaussian hypergeometric function, or just hypergeometric function, utilized in this work. The formulas are taken from [26], specifically chapter 15. Regarding Jacobi polynomials, we refer to chapter 18 of [26].

The Gauss hypergeometric differential equation is a second-order linear ordinary differential equation given by

$$z(1-z)\frac{d^2w(z)}{dz^2} + [c-(a+b+1)z]\frac{dw(z)}{dz} - abw(z) = 0, \tag{B.1}$$

where a, b, and c are complex parameters. This equation possesses three regular singular points at $z = 0$, $z = 1$, and $z = \infty$.

For the singular point at the origin $z = 0$, the two linearly independent solutions, assuming c is not an integer, are

$$w_1(z) = {}_2F_1(a,b;c;z) = \sum_{n=0}^{\infty} \frac{(a)_n(b)_n}{(c)_n}\frac{z^n}{n!} \tag{B.2}$$

and

$$w_2(z) = z^{1-c}{}_2F_1(a-c+1, b-c+1; 2-c; z) \tag{B.3}$$

where $(q)_n$ is the Pochhammer symbol defined as

$$(q)_n = \begin{cases} 1 & n = 0 \\ q(q+1)\dots(q+n-1) & n > 0 \end{cases}. \tag{B.4}$$

The function ${}_2F_1\,(a,b;c;z)$ denotes the hypergeometric function or Gaussian hypergeomteric function.

By shifting the variable to $t = 1 - z$, the solutions around the singularity $z = 1$, assuming $c - a - b$ is not an integer, are

$$w_3(z) = {}_2F_1(a,b;a+b-c+1;1-z) \tag{B.5}$$

and

$$w_4(z) = (1-z)^{c-a-b}\,{}_2F_1(c-a, c-b; c-a-b+1; 1-z). \tag{B.6}$$

We do not discuss the solution set around the singularity $z = \infty$, following the variable transform $t = 1/z$, because we do not need it in the main text. The relationship between the solutions at $z = 0$ and $z = 1$ is described by the linear transformation

$$\begin{aligned} {}_2F_1(a, b; c; z) &= \frac{\Gamma(c)\Gamma(c-a-b)}{\Gamma(c-a)\Gamma(c-b)}\,{}_2F_1(a, b; a+b-c+1; 1-z) \\ &+ \frac{\Gamma(c)\Gamma(a+b-c)}{\Gamma(a)\Gamma(b)}(1-z)^{c-a-b}\,{}_2F_1(c-a, c-b; c-a-b+1; 1-z). \end{aligned} \tag{B.7}$$

Using the series representation (B.2) it can be seen that for arbitrary parameters a, b, c we have

$${}_2F_1\left(a, b; c; 0\right) = 1. \tag{B.8}$$

Combining this result with equation (B.7) we can also deduce the limiting behaviour of ${}_2F_1\left(a, b; c; z\right)$ for $z = 1$.

The hypergeometric function is also connected to the Jacobi Polynomials. The hypergeometric series, defined in (B.2), terminates if either the first or second argument is a negative integer

$${}_2F_1\left(-m, b; c; z\right) = \sum_{n=0}^{m} (-1)^n \binom{m}{n} \frac{(b)_n}{(c)_n} z^n. \tag{B.9}$$

with $m \in \mathbb{N}_0$ and the binomial $\binom{m}{n}$. Similarly this works for $b = -m$. The connection to the Jacobi polynomials $P_n^{(\alpha,\beta)}(z)$ is

$$P_n^{(\alpha,\beta)}(z) = \binom{n+\alpha}{n} {}_2F_1\left(-n, n+\alpha+\beta+1; \alpha+1; \frac{1-z}{2}\right). \tag{B.10}$$

They fulfill the orthogonality relation on the interval $x \in [-1, 1]$

$$\begin{aligned} &\int_{-1}^{1} (1-x)^\alpha (1+x)^\beta P_m^{(\alpha,\beta)}(x) P_n^{(\alpha,\beta)}(x)\, dx \\ &\qquad = \frac{2^{\alpha+\beta+1}}{2n+\alpha+\beta+1} \frac{\Gamma(n+\alpha+1)\Gamma(n+\beta+1)}{\Gamma(n+\alpha+\beta+1)n!} \delta_{nm} \end{aligned} \tag{B.11}$$

for $\alpha, \beta > -1$. The Jacobi polynomials can also be defined by the Rodrigues formula

$$P_n^{(\alpha,\beta)}(z) = \frac{(-1)^n}{2^n n!} (1-z)^{-\alpha} (1+z)^{-\beta} \frac{d^n}{dz^n} \left[(1-z)^{\alpha+n} (1+z)^{\beta+n}\right]. \tag{B.12}$$

Appendix C

Polar spinor for the Dirac sphere

In this appendix we provide the calculation that determines the polar spinor

$$\begin{pmatrix} \alpha_{\lambda m}(x) \\ \beta_{\lambda m}(x) \end{pmatrix} = \begin{pmatrix} (1-x)^{\frac{\alpha_{+1}}{2}}(1+x)^{\frac{\beta_{+1}}{2}}\xi_{\lambda m}(x) \\ (1-x)^{\frac{\alpha_{-1}}{2}}(1+x)^{\frac{\beta_{-1}}{2}}\eta_{\lambda m}(x) \end{pmatrix}, \tag{C.1}$$

which is defined in (4.23).

In the corresponding section 4.2 we determined the solutions to the components of the reduced polar spinor

$$\mathrm{Y}_{\lambda m}(z) = \begin{pmatrix} \xi_{\lambda m}(z) \\ \eta_{\lambda m}(z) \end{pmatrix}. \tag{C.2}$$

and also the dimensionless energy λ. Now we use the coupling equations (4.21a) and (4.21b) to relate the integration constants of each component of the polar spinor to one another. Then we have the final solution only leaving a normalization constant. Similar to the calculation of the energies we use the sectors defined in table 4.1.

Sector I

The components of the reduced polar spinor are

$$\mathrm{Y}^{\sigma_z}_{\lambda m}(z) = A_{\sigma_z} {}_2F_1\left(a, b; c_{\sigma_z}; z\right) \tag{C.3}$$

with $a = -n$, dimensionless energy $\lambda(q_m) = \pm\left|n + \tilde{m} + \frac{1}{2}\right|$ and integration constants A_{σ_z}, which we aim to relate.

To express the hypergeometric series in terms of a Jacobi polynomial using equation (B.10) we note that

$$\alpha_{\sigma_z} + \beta_{\sigma_z} + 1 - a = 2|\tilde{m}| + 1 + n = b. \tag{C.4}$$

Absorbing the constant factors from equation (B.10) into the integration constant we obtain

$$\xi_{\lambda m}(x) = A_{+1} P_n^{(\alpha_{+1}, \beta_{+1})}(x) \tag{C.5}$$

for the upper component and

$$\eta_{\lambda m}(x) = A_{-1} P_n^{(\alpha_{-1},\beta_{-1})}(x) \tag{C.6}$$

for the lower component. The formulation in terms of the Jacobi polynomials naturally formulates the spinor in terms of the variable $x = \cos(\theta)$.

Using the second of the coupling equations (4.21b), with $x = \cos(\theta)$, we get

$$\frac{-i}{\sqrt{1-x^2}}\left(-\left(1-x^2\right)\frac{d}{dx} + \frac{x}{2}(1+q_m) - \frac{m+\frac{q_m}{2}}{\sin\theta}\right)\alpha_{\lambda m}(x) = \lambda\beta_{\lambda m}(x). \tag{C.7}$$

For $\mathrm{sgn}(m) = +1$ the LHS can be rewritten into

$$\frac{-iA_{+1}}{\sqrt{1-x^2}}(1-x)^{\frac{\alpha_{+1}}{2}}(1+x)^{\frac{\beta_{+1}}{2}} \times \left[-\beta_{+1}(1-x) - \left(1-x^2\right)\frac{d}{dx}\right] P_n^{(\alpha_{+1},\beta_{+1})}(x) \tag{C.8}$$

and for $\mathrm{sgn}(m) = -1$ the LHS can be rewritten as

$$\frac{-iA_{+1}}{\sqrt{1-x^2}}(1-x)^{\frac{\alpha_{+1}}{2}}(1+x)^{\frac{\beta_{+1}}{2}} \times \left[-\alpha_{+1}(1+x) - \left(1-x^2\right)\frac{d}{dx}\right] P_n^{(\alpha_{+1},\beta_{+1})}(x). \tag{C.9}$$

This form allows for using the recurrence relations of the Jacobi Polynomials

$$\begin{aligned}(x-1)\frac{d}{dx}P_n^{(\alpha,\beta)}(x) &= (\alpha+n)P_n^{(\alpha-1,\beta+1)} - \alpha P_n^{(\alpha,\beta)} \\ &= \frac{1-x}{1+x}\left(\beta P_n^{(\alpha,\beta)} - (\beta+n)P_n^{(\alpha+1,\beta-1)}\right),\end{aligned}$$

which can be obtained from chapter 18.9 of [26]. Thus, the expressions (C.8), (C.9) can be rewritten as

$$-iA_{+1}(1-x)^{\frac{\alpha_{-1}}{2}}(1+x)^{\frac{\beta_{-1}}{2}}P_n^{(\alpha_{-1},\beta_{-1})}(x) \times \begin{cases} -(\beta_{+1}+n), & \mathrm{sgn}(m) = +1 \\ (\alpha_{+1}+n), & \mathrm{sgn}(m) = -1 \end{cases}. \tag{C.10}$$

Finally, comparing this to the RHS of equation (C.7) we obtain

$$A_{-1} = -A_{+1}\frac{i}{\lambda} \times \begin{cases} -(\beta_{+1}+n), & \mathrm{sgn}(m) = +1 \\ (\alpha_{+1}+n), & \text{if } \mathrm{sgn}(m) = -1 \end{cases}. \tag{C.11}$$

Sector II and III

Following the approach for sector I we rewrite the solutions into Jacobi polynomials first.

The components of the reduced polar spinor are

$$\Upsilon^{\sigma_z}_{\lambda m}(z) = A_{\sigma_z} z^{1-c_{\sigma_z}} {}_2F_1\left(1+a-c_{\sigma_z}, 1+b-c_{\sigma_z}; 2-c_{\sigma_z}; z\right) \tag{C.12}$$

with $1+b-c_{+1} = -n = -n_{+1}$, $1+b-c_{-1} = -n-1 = -n_{-1}$, dimensionless energy $\lambda(q_m) = \pm\left|n+1+\frac{q_m}{2}\right|$ and integration constants A_{σ_z}, which we aim to relate.

To express the hypergeometric series in terms of a Jacobi polynomial using (B.10) we note that

$$-\alpha_{\sigma_z} + \beta_{\sigma_z} + 1 - (1+b-c_{\sigma_z}) = 1+a-c_{\sigma_z}. \tag{C.13}$$

Absorbing the constant factors into the integration constant we obtain

$$\xi_{\lambda m}(x) = A_{+1} P^{(-\alpha_{+1},\beta_{+1})}_{n_{+1}}(x) \tag{C.14}$$

for the upper component and

$$\eta_{\lambda m}(x) = A_{-1} P^{(-\alpha_{-1},\beta_{-1})}_{n_{-1}}(x) \tag{C.15}$$

for the lower component.

Again, using the coupling equation (C.7) we get for the LHS

$$\begin{aligned}&\frac{-iA_{+1}}{\sqrt{1-x^2}}(1-x)^{-\frac{\alpha_{+1}}{2}}(1+x)^{\frac{\beta_{+1}}{2}}\\ &\times\left[-\left(1-x^2\right)\frac{d}{dx} - (\alpha_{+1}+\beta_{+1}) + x(\beta_{+1}-\alpha_{+1})\right] P^{(-\alpha_{+1},\beta_{+1})}_{n_{+1}}(x).\end{aligned} \tag{C.16}$$

This corresponds to the backward shift identity

$$\left\{\left(1-x^2\right)\frac{d}{dx} + [(\beta-\alpha)-(\alpha+\beta)x]\right\} P^{(\alpha,\beta)}_n(x) = -2(n+1)P^{(\alpha-1,\beta-1)}_{n+1}(x) \tag{C.17}$$

which can be found in chapter 18.9 of [26].

After applying the backward shift identity and applying algebraic manipulations we can rewrite (C.16) as

$$-iA_{+1}(1-x)^{-\frac{\alpha_{-1}}{2}}(1+x)^{\frac{\beta_{-1}}{2}} 2(n+1) P^{(-\alpha_{-1},\beta_{-1})}_{n+1}(x). \tag{C.18}$$

Finally, comparing this to the RHS of the coupling equation (C.7) we obtain

$$A_{-1} = -A_{+1}\frac{2i}{\lambda}(n+1). \tag{C.19}$$

The procedure for sector III is similar to that for sector II and also makes use of the backward shift identity. The result for the relation of the integration constants is also the same as given in (C.19).

Sector IV

For sector IV we proceed similar to sector I to III. The components of the reduced polar spinor are given by

$$\Upsilon^{\sigma_z}_{\lambda m}(z) = A_{\sigma_z}{}_2F_1\left(a,b;c_{\sigma_z};z\right) + B_{\sigma_z} z^{1-c_{\sigma_z}}{}_2F_1\left(1+a-c_{\sigma_z},1+b-c_{\sigma_z};2-c_{\sigma_z};z\right) \tag{C.20}$$

Applying the coupling equation (C.7) we get for the LHS terms proportional to A_{+1}

$$A_{+1}\left[-2z(a+b-c_{+1}) + 2z(1-z)\frac{d}{dz}\right]{}_2F_1\left(a,b;c_{+1};z\right), \tag{C.21}$$

and for the terms proportional to B_{+1}

$$B_{+1}\left[z(1-z)\frac{d}{dz} + 1 - c_{+1} - (1+a-c_{+1}+1+b-c_{+1}-1)z\right] \times {}_2F_1\left(1+a-c_{+1},1+b-c_{+1};2-c_{+1};z\right), \tag{C.22}$$

where we leave out all prefactors of any powers of z and $1-z$ to avoid crowded expressions and isolate the contiguous relations.

Using the contiguous relations

$$z(1-z)\frac{d}{dz}{}_2F_1(a+1,b+1;c+1;z) + \left[c-(a+b+1)z\right]{}_2F_1(a+1,b+1;c+1;z) = c\,{}_2F_1(a,b;c;z), \tag{C.23a}$$

$$c(1-z)\frac{d}{dz}{}_2F_1(a,b;c;z) - c(a+b-c){}_2F_1(a,b;c;z) = (c-a)(c-b){}_2F_1(a,b;c+1;z) \tag{C.23b}$$

we can simplify the LHS of the coupling equation to

$$\begin{aligned} &-2iA_{+1}(1-\frac{a}{c_{+1}})(1-\frac{b}{c_{+1}})z^{\frac{\alpha_{-1}}{2}}(1-z)^{\frac{\beta_{-1}}{2}}{}_2F_1\left(a,b;c_{-1};z\right) \\ &-2iB_{+1}(1-c_{+1})z^{-\frac{\alpha_{-1}}{2}}(1-z)^{\frac{\beta_{-1}}{2}}{}_2F_1\left(1+a-c_{-1},1+b-c_{-1};2-c_{-1};z\right), \end{aligned} \tag{C.24}$$

now including all prefactors and powers of z and $1-z$. Comparing the expression to the RHS of the coupling equation (C.7) we finally obtain

$$A_{-1} = -\frac{2i}{\lambda}(1-\frac{a}{c_{+1}})(1-\frac{b}{c_{+1}})A_{+1}, \tag{C.25a}$$

$$B_{-1} = -\frac{2i}{\lambda}(1-c_{+1})B_{+1}. \tag{C.25b}$$

Bibliography

[1] B. Andrei Bernevig, Taylor L. Hughes, and Shou-Cheng Zhang, "Quantum Spin Hall Effect and Topological Phase Transition in HgTe Quantum Wells", in: *Science* 314.5806 (Dec. 2006), 1757–1761, ISSN: 1095-9203, DOI: 10.1126/science.1133734, URL: http://dx.doi.org/10.1126/science.1133734.

[2] M. Z. Hasan and C. L. Kane, "Colloquium: Topological insulators", in: *Rev. Mod. Phys.* 82 (4 2010), pp. 3045–3067, DOI: 10.1103/RevModPhys.82.3045, URL: https://link.aps.org/doi/10.1103/RevModPhys.82.3045.

[3] Mengyun He, Huimin Sun, and Qing Lin He, "Topological insulator: Spintronics and quantum computations", in: *Frontiers of Physics* 14.4, 43401 (Aug. 2019), p. 43401, DOI: 10.1007/s11467-019-0893-4.

[4] Paul Adrien Maurice Dirac, "A theory of electrons and protons", in: *Proceedings of the Royal Society of London. Series A, Containing Papers of a Mathematical and Physical Character* 126.801 (Jan. 1930), pp. 360–365, ISSN: 0950-1207, DOI: 10.1098/rspa.1930.0013, eprint: https://royalsocietypublishing.org/rspa/article-pdf/126/801/360/26095/rspa.1930.0013.pdf, URL: https://doi.org/10.1098/rspa.1930.0013.

[5] Alexander Ziesen, "Two-dimensional Dirac Systems: From Clean Dirac Spheres to Vortices on the Surface of Disordered, Proximitized Topological Insulators", Advisors: Fabian Hassler, David P. DiVincenzo, Ph.D. thesis, RWTH Aachen University, 2024, DOI: 10.18154/RWTH-2024-01309, URL: https://publications.rwth-aachen.de/record/978459/files/978459.pdf.

[6] David Tong, *Lectures on the Quantum Hall Effect*, 2016, arXiv: 1606.06687 [hep-th], URL: https://arxiv.org/abs/1606.06687.

[7] G. Rosenberg and M. Franz, "Witten effect in a crystalline topological insulator", in: *Phys. Rev. B* 82 (3 2010), p. 035105, DOI: 10.1103/PhysRevB.82.035105, URL: https://link.aps.org/doi/10.1103/PhysRevB.82.035105.

[8] E. Witten, "Dyons of charge $e\theta/2\pi$", in: *Physics Letters B* 86.3 (1979), pp. 283–287, ISSN: 0370-2693, DOI: https://doi.org/10.1016/0370-2693(79)90838-4, URL: https://www.sciencedirect.com/science/article/pii/0370269379908384.

[9] Shoto Aoki et al., *Why magnetic monopole becomes dyon in topological insulators*, 2024, arXiv: 2304.13954 [cond-mat.mes-hall], URL: https://arxiv.org/abs/2304.13954.

[10] G. Rosenberg, H.-M. Guo, and M. Franz, "Wormhole effect in a strong topological insulator", in: *Phys. Rev. B* 82 (4 2010), p. 041104, DOI: 10.1103/PhysRevB.82.041104, URL: https://link.aps.org/doi/10.1103/PhysRevB.82.041104.

[11] Sebastian Huber and Titus Neupert, *Topological Condensed Matter Physics*, https://ethz.ch/content/dam/ethz/special-interest/phys/theoretical-physics/cmtm-dam/documents/tqn/tqn-2021/TopCondMat.pdf, Lecture Notes, Department of Physics, ETH Zürich and Department of Physics, University of Zürich, 2021.

[12] János K. Asbóth, László Oroszlány, and András Pályi, *A Short Course on Topological Insulators*, Springer International Publishing, 2016, ISBN: 9783319256078, DOI: 10.1007/978-3-319-25607-8, URL: http://dx.doi.org/10.1007/978-3-319-25607-8.

[13] Xiao-Liang Qi, Taylor Hughes, and Shou-Cheng Zhang, "Topological Field Theory of Time-Reversal Invariant Insulators", in: *Phys. Rev. B* 78 (2008), p. 195424, DOI: 10.1103/PhysRevB.78.195424, arXiv: 0802.3537 [cond-mat.mes-hall].

[14] R. Jackiw and C. Rebbi, "Solitons with fermion number ½", in: *Phys. Rev. D* 13 (12 1976), pp. 3398–3409, DOI: 10.1103/PhysRevD.13.3398, URL: https://link.aps.org/doi/10.1103/PhysRevD.13.3398.

[15] Ph. de Sousa Gerbert, "Fermions in an Aharonov-Bohm field and cosmic strings", in: *Phys. Rev. D* 40 (Aug. 1989), pp. 1346–1349, DOI: 10.1103/PhysRevD.40.1346.

[16] C. W. Groth et al., "Kwant: a software package for quantum transport", in: *New Journal of Physics* 16 (2014), p. 063065, DOI: 10.1088/1367-2630/16/6/063065.

[17] Andrej Mesaros et al., "Zero-energy states bound to a magnetic π-flux vortex in a two-dimensional topological insulator", in: *Nuclear Physics B* 867.3 (Feb. 2013), 977–991, ISSN: 0550-3213, DOI: 10.1016/j.nuclphysb.2012.10.022, URL: http://dx.doi.org/10.1016/j.nuclphysb.2012.10.022.

[18] A. A. Abrikosov Jr, *Dirac operator on the Riemann sphere*, 2002, arXiv: hep-th/0212134 [hep-th], URL: https://arxiv.org/abs/hep-th/0212134.

[19] Ken-Ichiro Imura et al., "Spherical topological insulator", in: *Phys. Rev. B* 86 (23 2012), p. 235119, DOI: 10.1103/PhysRevB.86.235119, URL: https://link.aps.org/doi/10.1103/PhysRevB.86.235119.

[20] Michael Dunia, P. Q. Hung, and Douglas Singleton, "A new look at the Dirac quantization condition", in: *The European Physical Journal C* 83.6 (June 2023), ISSN: 1434-6052, DOI: 10.1140/epjc/s10052-023-11684-8, URL: http://dx.doi.org/10.1140/epjc/s10052-023-11684-8.

[21] R Jackiw, "Fractional and Majorana fermions: the physics of zero-energy modes", in: *Physica Scripta* 2012.T146 (2012), p. 014005, DOI: 10.1088/0031-8949/2012/T146/014005, URL: https://doi.org/10.1088/0031-8949/2012/T146/014005.

[22] Chao-Xing Liu, Shou-Cheng Zhang, and Xiao-Liang Qi, *The quantum anomalous Hall effect*, 2015, arXiv: 1508.07106 [cond-mat.mes-hall], URL: https://arxiv.org/abs/1508.07106.

[23] P. W. Brouwer, "Scattering approach to parametric pumping", in: *Physical Review B* 58.16 (Oct. 1998), R10135–R10138, ISSN: 1095-3795, DOI: 10.1103/physrevb.58.r10135, URL: http://dx.doi.org/10.1103/PhysRevB.58.R10135.

[24] G. Bräunlich, G. M. Graf, and G. Ortelli, "Equivalence of Topological and Scattering Approaches to Quantum Pumping", in: *Communications in Mathematical Physics* 295.1 (2010), pp. 243–259, DOI: 10.1007/s00220-009-0983-1, URL: https://doi.org/10.1007/s00220-009-0983-1.

[25] I. C. Fulga, F. Hassler, and A. R. Akhmerov, "Scattering theory of topological insulators and superconductors", in: *Physical Review B* 85.16 (Apr. 2012), ISSN: 1550-235X, DOI: 10.1103/physrevb.85.165409, URL: http://dx.doi.org/10.1103/PhysRevB.85.165409.

[26] *NIST Digital Library of Mathematical Functions*, https://dlmf.nist.gov/, Release 1.2.5 of 2025-12-15, F. W. J. Olver, A. B. Olde Daalhuis, D. W. Lozier, B. I. Schneider, R. F. Boisvert, C. W. Clark, B. R. Miller, B. V. Saunders, H. S. Cohl, and M. A. McClain, eds., URL: https://dlmf.nist.gov/.

Acknowledgements

First, I would like to thank Fabian Hassler for offering this thesis to me. I would like to thank him for providing me with constant supervision and long discussions. Sometimes it has taken me far longer than expected to understand what he meant to explain to me, but sooner or later his intuitive approach always offered me a new way of doing physics and understanding problems.

I would also like to thank Markus Müller for being my second examiner.

Special thanks also go to Jonathan, Steven and Konstantinos for being my office mates and incorporating me into the group.

Then, I would like to thank my parents for always supporting me during my studies. Without them I would have never studied physics.

Finally, I would like to thank all my friends who were always there for me and never let my freetime get boring. Especially, I would like to mention Leo, Henry, Pablo, Mike, Mark and Roman.